Low-Temperature Methanol Steam Reforming

Hugo José Lopes Silva

Dissertation presented for the degree of

Doctor of Philosophy in Chemical and Biological Engineering

by the

University of Porto – Faculty of Engineering

LEPABE – Department of Chemical Engineering

University of Porto – Faculty of Engineering

Porto, 2015

Dissertation supervised by:

Adélio Miguel Magalhães Mendes

Full Professor

Department of Chemical Engineering

University of Porto – Faculty of Engineering

Cecília Mateos Pedrero

Postdoctoral Researcher

Department of Chemical Engineering

University of Porto – Faculty of Engineering

Financial support:

Acknowledgements

I would like to acknowledge the Portuguese National Founding Agency for Science, Research and Technology (FCT), for the attributed grant SFRH/BD/45890/2008. I am grateful to the European Union's Seventh Framework Programme (FP7/2007-2013) for the Fuel Cells and Hydrogen Joint Technology Initiative under grant agreement No [303476] due to the funding received for part of this work. I also acknowledge financing from FCT through the project PTDC/EQU-EQU/104217/2008. To LEPABE and DEQ that offered me the conditions to conduct the research activity.

I express a sincere feeling of gratitude to my supervisors. To Professor Adélio Mendes for giving me the opportunity of being part of an outstanding research group that combines several areas of knowledge. Thank you also, for all the passionate and enthusiastic scientific discussions that revealed to be a truly learning experience. To Dr. Cecilia Mateos Pedrero, I would like to extend my gratitude; thank you for all the support, knowledge, advises and guidance that lead to the definition of this thesis. In days of struggle, you were strength. Your friendship is a gift that I really hope to save and respect through its different timings.

I am also grateful to Dr. Sandra Sá, colleague that I had the opportunity to work at LEPABE within the methanol steam reforming (MSR) research field, and that had the valuable contribution concerning the project/assembly of an in-house set-up for evaluating the MSR catalysts performance. The opportunity to be integrated in the same project and work together was fundamental for the results presented in this dissertation. Also, I would like to acknowledge Professor Sousa for the learning experience during the assembly of the control and acquisition box of the set-up, which included LabView programming.

I cannot forget to express my gratitude to Dr. Alfredo Tanaka for sharing its vast knowledge and experience in the field of materials science, which was crucial for finding a path in this work. Thank you.

I would like to acknowledge Dr. Katarzyna Eblagon for her relevant contribution in chapter 4 of this thesis, concerning the performance of Pd/ZnO catalysts for MSR. The Instituto de Tecnología Química (ITQ), in the Polytechnic University of Valencia (UPV), partner of the BeingEnergy Project, I would like to acknowledge the research period in their facilities and to Abdessamad Grirrane and Professor Hermenegildo Garcia for the reception and guidance. Finnally, to Dr J. L. Jorda Moret and to Dr. P. H. Concepción also from ITQ-UPV for the discussion and analysis of the Pd/ZnO samples through *in-situ* XRD and CO DRIFT studies, respectively.

Paulo Ribeirinha is acknowledged for the simulated results of the kinetic models presented in Chapter 5.

The work in this thesis, presented as a compilation of scientific publications, is the outcome of the endeavor of several co-autors, and I would like to acknowledge each and every one for their valuable contributions.

To my coleagues in LEPABE I want to say thank you for all the companionship and good moments shared. If you find reasons to smile there is no space for concerns.

I would like to say to my Parents and to my sister Raquel that there is not enough time to reattribute all the love and sacrifices that were made during my period at FEUP. Thank you.

Finally, to Susana I cannot say that I do not ask myself: where were you all this time? What makes me happy at the present moment is that we have a long future in front of us. I want to live the largest chapter of my life with you by my side.

Abstract

Climate changes due to greenhouse-gas emissions and the continuous growth of energy demand are triggering the search for cleaner and sustainable energy sources for the near future, where hydrogen combined to fuel cell technology is expected to have a key role. Despite being the most attractive fuel for polymer electrolyte membrane fuel cells (PEMFCs), hydrogen storage is still a limiting factor with the currently available technologies, which entails safety risks, non-competitive overall efficiency and lower volumetric density when compared to other fuels. The current options are pressurized hydrogen (700 bar, 39 $kgH_2 \cdot m^{-3}$), liquefied hydrogen at cryogenic temperatures (21 K, 70.8 $kgH_2 \cdot m^{-3}$) and storage in solids (e.g. Mg_2FeH_6, 150 $kgH_2 \cdot m^{-3}$). Therefore, the on-site hydrogen production in an integrated and compact energy system with fuel cells has been pointed out as an alternative solution for stationary and transportation applications. In this scenario, the methanol steam reforming reaction (MSR) is one very attracting alternative that takes into account all the advantages inherent to the use of the simplest of all alcohols as a hydrogen carrier.

This thesis focuses on the development and study of highly efficient catalysts for MSR. The state of the art of these catalysts can be divided in two main groups: copper-based and the group 8-10 metal-based catalysts, largely represented by the Pd/ZnO formulation. Both groups of catalysts are addressed in this thesis and different strategies for improving their performance are presented.

As a first approach in this work, a urea-assisted hydrothermal synthesis method was deeply studied with the purpose of tailoring the physicochemical properties of a metal oxide that is ubiquitous in both groups of MSR catalysts - zinc oxide (ZnO). The inclusion of Pluronic P123 block copolymer in the preparation method revealed to be crucial for obtaining highly dispersed ZnO microflowers with enhanced surface area and higher proportion of polar crystal planes (higher polarity). Additionally, the type of metal salt precursor influenced the morphology and polarity properties of ZnO. In this way, when zinc acetate was used it occurred the formation of highly faceted microflowers, whereas zinc nitrate led to urchin-like structures with lower

polarity. This simple and easily scalable synthesis method was crucial for evaluating the influence of ZnO properties in a catalytic system for MSR.

In a following study, the developed ZnO supports were used for the preparation of Cu/ZnO catalysts. The activity and selectivity of these catalysts was confirmed to be strongly related with the surface area and polarity properties of ZnO. While increasing the surface area, higher dispersion of active copper particles was attained and consequently the activity was enhanced. A noteworthy result was the lower carbon monoxide production of the catalysts with higher proportion of polar planes. Inclusively, the selectivity at high conversion levels was significantly better than a reference commercial catalyst ($CuO/ZnO/Al_2O_3$ from Süd-Chemie) under the same kinetic conditions.

As an alternative to the copper-based catalysts, the more recent Pd/ZnO formulation shows a surprising shift of selectivity towards MSR when a PdZn alloy is formed. In another study presented within the framework of this thesis, a series of ZnO supports prepared by the hydrothermal route, were calcined under different gas atmospheres (i.e. H_2, N_2, O_2 and air). The support calcined in a H_2 atmosphere presented an enhanced performance for MSR, which was associated to the higher concentration of oxygen vacancies on ZnO surface. Again, in this group of catalysts, the support properties had an impact on the catalyst performance.

As a final study, a novel CuZrDyAl catalyst formulation was prepared by the coprecipitation method and a kinetic study within the low-temperature MSR range was performed. The developed catalyst was then compared with the $CuO/ZnO/Al_2O3$ commercial catalyst and showed better performance in terms of selectivity (namely, yielding lower CO concentration) and activity. This behavior was attributed to the improved reducibility of the copper particles in the CuZrDyAl catalyst. The parameters of a simple power-law equation and two mechanistic kinetic models were determined. The best fitting with the experimental data was obtained when using mechanistic Model 3, based on the reported work from Peppley *et al.* for the commercial $CuO/ZnO/Al_2O_3$. Noteworthy, is the small number of MSR kinetic studies within the temperature range of 170 ºC-200 ºC.

Resumo

As mudanças climáticas devido às emissões de gases estufa e o crescimento contínuo do consumo energético fomentam a procura de novas fontes de energia ambientalmente limpas e sustentáveis para um futuro próximo, onde se espera que hidrogénio combinado com a tecnologia das celúlas de combustível venha a ter um papel crucial. Apesar de ser o melhor combustível para as células de combustível de membrana de permuta iónica, o armazenamento de hidrogénio ainda é um fator limitante com as tecnologias actualmente disponíveis, envolvendo riscos para a segurança, uma eficiência global pouco competitiva e uma menor densidade volumétrica quando comparado a outros combustíveis. As opções atuais são o armazenamento de elevada pressão (700 bar, 39 kg $H_2 \cdot m^{-3}$), a liquefação do hidrogénio a temperaturas criogênicas (21 K, 70,8 kg $H_2 \cdot m^{-3}$) e o armazenamento em sólidos (por exemplo Mg_2FeH_6, 150 kg $H_2 \cdot m^{-3}$). A produção *in situ* de hidrogénio num sistema integrado de energia e compacto com células de combustível, tem sido apontada como uma solução alternativa para aplicações estacionárias e no sector dos transportes. Neste cenário, a reação de reformação com vapor de metanol é uma alternativa muito atractiva que tem em conta todas as vantagens inerentes à utilização do mais simples de todos os álcoois para o transporte de hidrogénio.

O principal foco desta tese foi o desenvolvimento e estudo de catalisadores altamente eficientes para a reformação com vapor de metanol. Com base no estado da arte destes catalisadores, estes podem ser divididos em dois grupos principais:os catalisadores à base de cobre e os catalisadores do grupo 8-10, representados principalmente pela formulação de Pd/ZnO. Ambos os grupos de catalisadores são abordados nesta tese e diferentes estratégias para a melhoria do seu desempenho são apresentadas.

Como uma primeira abordagem neste trabalho, foi desenvolvido um método de síntese hidrotérmica com a finalidade de controlar as propriedades físico-químicas de um óxido de metal que é ubíquo em ambos os grupos de catalisadores para a reformação com vapor de metanol - óxido de zinco (ZnO). A inclusão de um copolímero (Pluronic P123) no método de preparação revelou-se crucial para a obtenção de microestruturas de ZnO altamente dispersas, com uma elevada área

superficial e uma maior proporção de planos cristalinos polares (maior polaridade). Além disso, o tipo de precursor usado também influenciou a polaridade e a morfologia do ZnO. Desta forma, quando acetato de zinco foi utilizado ocorreu a formação de microestruturas altamente facetadas, enquanto que o nitrato de zinco conduziu à formação de estruturas com menor polaridade. Este método de síntese simples e que possibilita um fácil aumento de escala, foi de importância crucial para avaliar a influência das propriedades do ZnO num sistema catalítico para a reformação com vapor de metanol.

Num segundo estudo, os suportes catalíticos de ZnO foram usados para a preparação de catalisadores de Cu/ZnO. A actividade e selectividade destes catalisadores revelou-se estar relacionada com a área superficial e polaridade do ZnO. Com o aumento da área superfical, maior dispersão de partículas de cobre activas foi alcançada e, consequentemente, a actividade aumentou. Um resultado interessante foi a menor produção de monóxido de carbono dos catalisadores preparados usando suportes de maior polaridade. Inclusive, a seletividade para níveis elevados de conversão foi significativamente melhor do que a selectividade de um catalisador comercial de referência ($CuO/ZnO/Al_2O_3$ - Süd-Chemie).

Como uma alternativa aos catalisadores à base de cobre, a formulação de Pd/ZnO mostra uma surpreendente mudança de selectividade no sentido da reação de reformação com vapor de metanol, quando uma liga metálica de PdZn é formada. Em outro estudo apresentado no âmbito desta tese, uma série de suportes de ZnO preparados pelo método de síntese hidrotérmica, foram calcinados sob diferentes atmosferas de gasosas (H_2, N_2, O_2 e ar). O suporte de ZnO calcinado numa atmosfera de H_2 apresentou um melhor desempenho, o que foi associado à maior concentração de lacunas de oxigénio na superfície deste suporte. Mais uma vez, neste grupo de catalisadores, as propriedades do suporte tiveram um impacto sobre o desempenho do catalisador.

Num último estudo, uma nova formulação catalítica para a reformação com vapor de metanol é apresentada: CuZrDyAl. Este catalisador foi ulizado para realizar um estudo cinético numa gama de baixas temperaturas. O desempenho do catalisador desenvolvido foi comparado com o catalisador comercial de referência

$CuO/ZnO/Al_2O_3$ e apresentou melhores resultados em termos de seletividade (ou seja, produzindo menor concentração CO) e atividade. Este resultado encontrou-se estar relacionado com a melhoria da reducibilidade das partículas de cobre. Foram determinados os parâmetros de ajuste para um modelo empírico e para dois modelos mecanísticos. O melhor ajuste dos dados experimentais foi obtido para o modelo 3, com base no trabalho publicado por Peppley *et al.* para o catalisador comercial de $CuO/ZnO/Al_2O_3$. É de realçar o número reduzido de estudos cinéticos na gama de temperaturas entre 170 ºC-200 ºC.

Contents

Figure Captions

Table Captions

Chapter 1

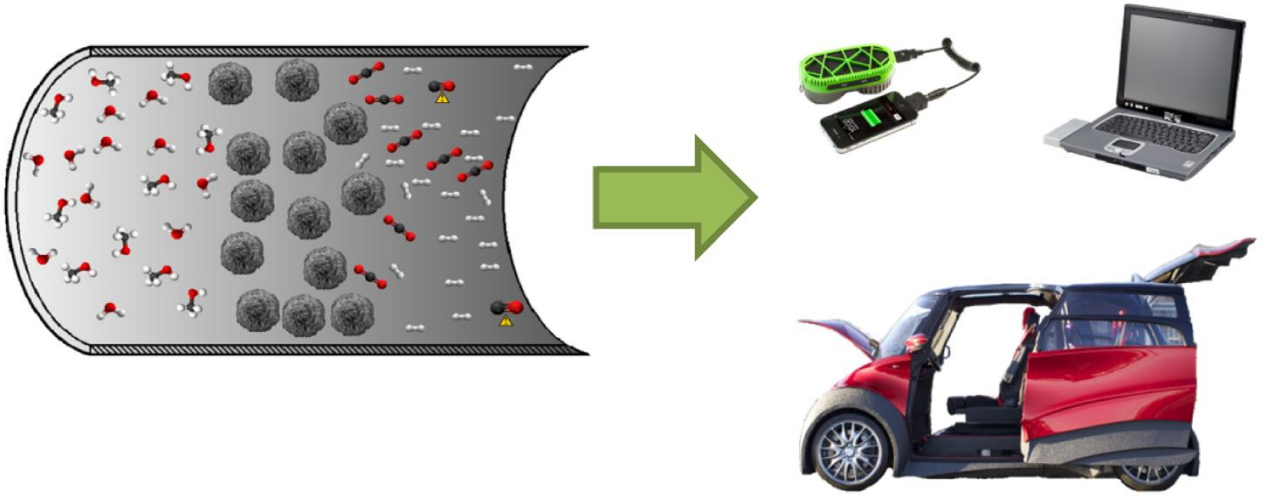

Chapter 1. Introduction

The global energy system has currently two major concerns that call an immediate intervention: the continuous growth of energy demand and climate changes. According to the international energy agency (IEA) the global primary energy demand is projected to have an increase of 1.5 % per year between 2007 and 2030 [1]. The predicted scenario indicates a 40 % increase in tonnes of oil equivalent (toe), assuming that no changes will occur in the energy sector – Figure 1.1.

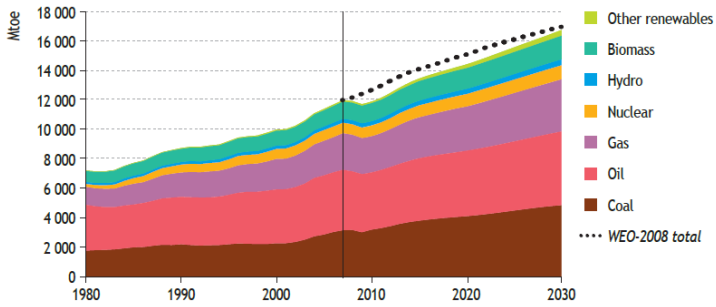

Figure 1.1 - World primary energy demand by fuel relative to the IEA projections in 2008 (image adapted from IEA 2009 [1]).

This indicates an unsustainable trend of the present energy system. The climbing of energy demand is combined with a dependence in hydrocarbons resources (oil, gas and coal) that are finite. As a reminder, the recent rising in oil demand placed the price per barrel in a new record at July 2008, exceeding the 140 US dollars per barrel [2].

The energy sector has also been held responsible for the alarming climate changes of our time, mainly due to greenhouse-gas emissions (see Figure 1.2). This awareness is causing political intervention to settle targets of CO_2 concentration levels. As a belief, the barrier of the 450 ppm in CO_2 equivalent is the upper limit for maintaining the temperature changes below the 2 ˚C, having as reference the pre-industrial period [3].

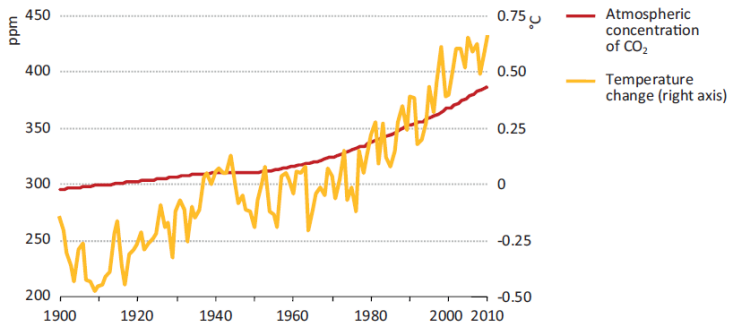

Figure 1.2 - Atmospheric concentration of CO_2 in connection with the temperature changes (image adapted from IEA 2013 [3]).

Looking at these projections is easy to understand that is imperative to develop cleaner and sustainable energy sources.

1.1. Fuel Cells

As an environmentally friendly technology, fuel cells are expected to have a key role in the near future for the clean production of electric power. By definition, a fuel cell is an energy conversion device that electrochemically converts chemical energy within two reactants, a fuel and an oxidant, into electrical energy, heat and water as by-product [4]. The fuel cells working principle is very simple and four main components are responsible for the electrochemical reactions: electrically negative electrode (anode) where the fuel is supplied, electrically positive electrode (cathode) where an oxidant is supplied, an electrolyte that separates the two electrodes and an external electrical circuit that connects the electron migration from the anode to the cathode side [5]. Generally, fuel cells are classified according to the nature of electrolyte used. Based on this criterion, the following types of fuel cells were developed: alkaline fuel cells (AFC) that use alkaline solution electrolytes; phosphoric acid fuel cells (PAFCs) using phosphoric acid electrolyte; polymer electrolyte membrane fuel cells (PEMFC) using proton exchange membranes; molten carbonate fuel cells (MCFC) using molten carbonate salt electrolytes; solid oxide fuel cells (SOFC) using ceramic ion conducting electrolyte in solid oxide form.

When compared to other fuel cells, PEMFCs are regarded as the most promising and versatile reaching the portable (5 W-20 kW), stationary (0.5 kW-400 kW) and transport (1 kW-100 kW) areas of application [5]. This technology is discussed in the following section.

1.1.1. PEMFCs

The polymer electrolyte membrane fuel cells (PEMFCs) are considered the best suitable fuel cells for commercial applications, especially as mentioned before for the transport and small scale stationary applications. Their popularity is mainly due to the simple operation process, moderate operating temperatures (60-80 ˚C), fast starting up time, high power densities (ca. 300-1000 $mW \cdot cm^{-2}$) [6] and long-term stability (ca. more than 20,000 h [7]). Typically, hydrogen is the elected fuel, leading to the higher efficiencies. However, a common subtype of PEMFCs is the direct methanol fuel cells (DMFCs) that use methanol as fuel instead of hydrogen. Nevertheless, there are several challenges faced by DMFC technology that include high catalyst usage, which results in higher costs, lower power density, lower efficiency as result of methanol crossover and shorter operable life compared with direct hydrogen systems [8-10]. Therefore, the former technology has lower competiveness than the hydrogen operated PEMFCs.

However, the PEMFCs face some drawbacks of its own to overcome. One common disadvantage presented by PEMFC is the high cost of the anode catalyst, typically made of a Pt alloy; the catalyst loading is of 0.2-0.3 $mg \cdot cm^{-2}$ for both anode and cathode [11]. Another crucial matter is the sensitivity of the electrocatalyst to fuel impurities. For instance, the presence of CO even in trace amounts (10 ppm) causes a serious loss of effectiveness of the anode electrocatalyst [5]. Presently, the Pt-Ru alloy catalysts are responsible for improving the tolerance levels for 200 ppm [5]. Nevertheless, the hydrogen supplied to the anode should be highly pure.

Recently high temperature polymer electrolyte fuel cells (HT-PEMFCs) technology shifted the tolerable limits of CO to 20,000-30,000 ppm [12]. These fuel

cells can operate up to 200 °C with electrolyte membranes made of a highly chemical and thermal stable polymer, PBI – polybenzimidazole, doped with phosphoric acid. This gives extra-flexibility regarding the demanding CO levels, and is a consequence of the high operating temperatures, which declines the adsorption thermodynamics of CO [13]. As additional advantages HT-PEMFCs have simpler system architectures and among the dispensable process units are: preferential oxidation reactors, humidifiers, air compressors and radiators [12].

The research and development efforts concerning fuel cells technology have increased over the last years, in an attempt to maturate a commercial technology for a wide range of sectors. Globally there are more than 2000 companies working on the conception and commercialization of novel products based on fuel cell technologies [14]. A very recent example of one successful commercial example in the transport sector is the fuel cell vehicle from Toyota – Figure 1.3. The Mirai fuel cell Sedan is going to be released in Europe in September 2015 [15].

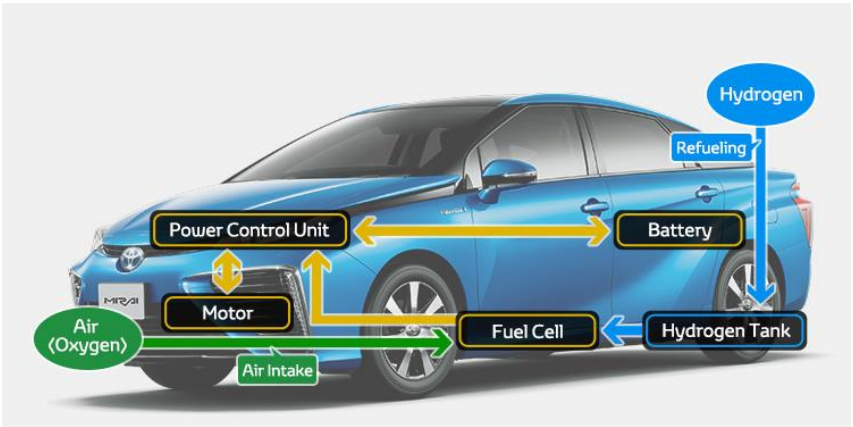

Figure 1.3 - The Mirai Sedan fuel cell vehicle from Toyota (image adapted from [15])

The former vehicle represents one strong example of the PEMFCs valuable commercial application in the transportation sector. However, as a requirement, pure hydrogen is supplied to the fuel cell and in the following sections the limitations of hydrogen storage and transport are discussed.

1.2. Hydrogen: storage and transportation

Hydrogen is considered a clean fuel with a high gravimetric energy and without any question is a vast element, representing 90 % of the atoms present in the universe [16]. This characteristics turn hydrogen into a preferential fuel that has led to the proposal of the so-called hydrogen economy. However, the hydrogen economy is not simply dependent on the capacity to produce hydrogen, but also on its storage and distribution. A passenger car similar to the Toyota in Figure 3 needs 4-5 kg of hydrogen to have a driving range of 500 km [2]. However, hydrogen has low energy content per unit of volume, requiring 3000 times more space than gasoline for an equivalent amount of energy [16]. This represents a huge drawback and research efforts are ongoing in order to develop compact hydrogen storage systems with high mechanical strength and durability, safety under normal use, acceptable risk under extreme conditions, good thermodynamics, fast kinetics, effective heat transfer and long life or many cycles of absorption/desorption (hydrides) [17].

There are three primary techniques to store hydrogen: compressed gaseous hydrogen, liquid hydrogen and hydrides. The compress gaseous hydrogen technique is based on applying high storage pressures. As a consequence of such high pressures, the wall material has a crucial role regarding safety. This material should have, as ideal properties, low density and high tensile strength, resistance to aging and fatigue (mainly due to loading), and impermeability to the small hydrogen molecule. Compressed hydrogen has other drawbacks, among them is still the low energy per volume compared to fossil fuels (39 $kgH_2 \cdot m^{-3}$ at 700 bar); the high operation pressures (350-700 bar) [43] demand the integration of strict control and safety systems. Regarding the compression costs, they are 10-15 % of the energy contained in the hydrogen fuel [16]. Also, the tank material can became brittle after a long exposure to hydrogen, reducing the wall material ductility, which conducts to wall cracking below the normal yield stress.

Liquid hydrogen is produced at very low temperatures, around -253 °C. In comparison with the previous technique low pressures of storage are applied (0.1-0.35 MPa) [46]. Even at low pressures, liquid hydrogen has twice as much energy content (70.8 kg $H_2 \cdot m^{-3}$) [17]. The main problem of liquid hydrogen storage is

hydrogen boil-off. This phenomenon happens due to heat transfer from the surroundings to the hydrogen tank. In this case, hydrogen becomes gaseous and leaks from the storage tank. With the current thermal insulation technology, hydrogen leaks can reach a rate of 2-3 % by volume per day [18]. Another reported problem is the low efficiency of liquid hydrogen storage. The work needed to liquefy hydrogen can reach ca. 30 % of the hydrogen energy content [18].

Hydrides, is the third approach for hydrogen storage. It is based on chemically absorb hydrogen on solid metals or metallic alloys. In the desorption process, to release hydrogen from the metal hydrides, heat needs to be supplied. The hydrides are divided in two groups: metal hydrides or chemical hydrides. In chemical hydrides, hydrogen forms a covalent bond with the alloy, whereas metal hydrides are ionic compounds of hydrogen and metal. The hydrides structures are typically AB, AB_2, A_2B, AB_3, and AB_5 [19, 20]. *A* element is an alkaline or rare earth metal (La, Zr, Ti or Mg), and *B* element is usually a transition metal (Ni, Mn, or Fe). In literature A_2B and AB_2, are considered the best metal hydrides due to their light weight, high storage capacities, good absorption/desorption kinetics and they can initiate hydrogen absorption without a catalyst [19]. The drawbacks of this technology are the difficulty to retrieve hydrogen after several absorption/desorption cycles, low hydrogen gravimetric density, the impurities accumulation can reduce the initial storage capacity, the necessity of high temperatures for promoting hydrogen desorption from light metal hydrides, and the infrastructures for a hydride based economy do not exist. Additionally, despite the fact that metal hydrides have higher hydrogen volumetric densities (e.g. 150 $kgH_2 \cdot m^{-3}$, Mg_2FeH_6) [21] than compressed or liquid hydrogen techniques, the volumetric densities are still below other common fuels. The comparison between the energy content of some of the former mentioned H_2 storage techniques and other common fuels is established in Figure 1.4.

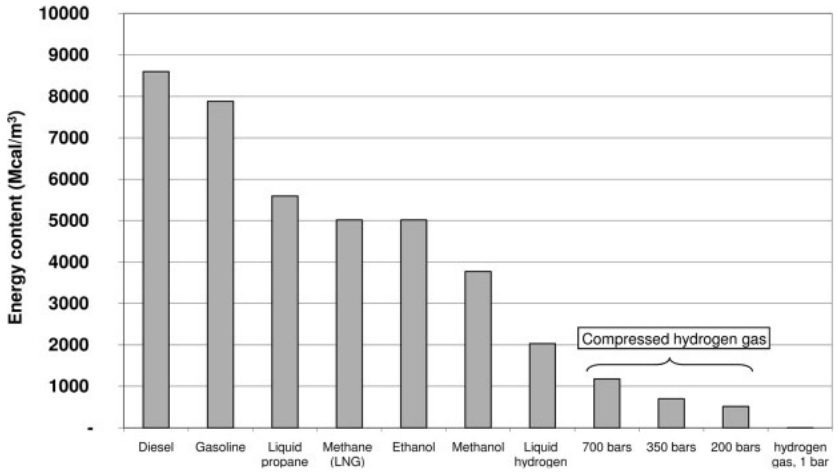

Figure 1.4 -- Energy content of common fuels in comparison with hydrogen storage techniques (image adapted from [16])

It can be concluded that there are severe technologic difficulties surrounding the economically and safety handling of hydrogen. Hydrogen storage problem can be overcome while using a liquid oxygenated fuel, such as methanol. This is one of the proposed strategies in this work.

1.3. Methanol

An alternative approach that arises from the limitations of H_2 storage and transport is the use of methanol as an energy feedstock. Presently, methanol is one of the largest volume commodity chemical produced in the world [22]. In 2013, the global methanol demand reached the 60.7 million metric tons [23]. Methanol is almost exclusively produced from natural gas through a syngas route: methane reforming produces syngas that is converted to methanol at 200-300 °C and 50-100 atm, through the following reactions:

$$CO+2H_2 \rightleftarrows CH_3OH \quad (1.1)$$

$$CO_2+3H_2 \rightleftarrows CH_3OH+H_2O \quad (1.2)$$

$$CO_2 + H_2 \rightleftarrows CO + H_2O \quad (1.3)$$

Although reserves of methane are still large they are diminishing. Therefore, unconventional sources of methane should be exploited such as methane hydrates or biomass. Methane hydrates resources discovered in oceans are 20 times larger than those of oil, gas and coal together [24]. The biomass processes include the utilization of wood and wood wastes, agricultural crops and their waste byproducts, municipal solid waste, animal waste, and aquatic plants and algae [16].

Methanol storage and transport are simple when compared to hydrogen and other oxygenated hydrocarbons. It is liquid at atmospheric pressure and normal environmental temperature. In terms of environmental impact, the high miscibility of methanol with water prevents in a spill incident the spread over large areas of open waters, which is an adverse effect of oil or gasoline spills [11]. Moreover, in a spill situation methanol is readily metabolized by living organisms. In transport applications, methanol-powered fuel cell vehicles are promising for minimizing all current air pollutants from vehicles. Analyzing from the toxicology point of view, methanol, like other motor fuels, is considered to be a hazardous compound. However, contrarily to gasoline it is not carcinogenic or mutagenic. It is promptly absorbed by ingestion, inhalation, and more slowly by skin exposure. For measuring the impact of methanol use on public health, a study was performed concerning the normal exposure of humans to methanol during a car refueling [16]. The levels were much lower than a soda containing aspartame, compound that is metabolized to methanol. Only 2-3 mg of methanol is absorbed during refueling and a daily intake of up to 500 mg is safer for a human diet [16].

1.3.1. Methanol Steam Reforming for H_2 production

The on-site hydrogen production through the reforming of alcohols and hydrocarbons, in an integrated and compact energy system with fuel cells is pointed as an alternative solution to overcome the drawbacks of hydrogen storage and transport. When compared to other fuels, methanol presents several advantages for

hydrogen production. With only one carbon atom, methanol is the simplest of all alcohols. The absence of a strong C–C bond facilitates the reforming at low-temperatures (200 – 300 ˚C). This range of temperatures is very low when compared to other common fuels such as methane, which is reformed above 500 ˚C [25] and ethanol, with a reforming temperature around 400 ˚C [26]. Moreover, it has high hydrogen to carbon ratio. In addition to the overall steam reforming reaction, Equation (1.4), two side reactions are commonly considered: methanol decomposition, Equation (1.5), and water–gas shift, Equation (1.6), [27, 28]:

$$CH_3OH + H_2O \rightleftarrows CO_2 + 3H_2 \qquad \Delta H_{298} = 49.7\,kJ\cdot mol^{-1} \qquad (1.4)$$

$$CH_3OH \rightleftarrows CO + 2H_2 \qquad \Delta H_{298} = 92\ kJ\cdot mol^{-1} \qquad (1.5)$$

$$CO + H_2O \rightleftarrows CO_2 + H_2 \qquad \Delta H_{298} = -41.2\ kJ\cdot mol^{-1} \qquad (1.6)$$

Even though the purpose of the methanol steam reforming reaction is the production of hydrogen, there are other products formed that must be taken into consideration. Besides the non-reacted water and methanol, the reaction mixture is composed by hydrogen, carbon dioxide and small amounts of carbon monoxide. Reminding that the hydrogen produced is for PEMFC applications, it is clear that the formation of carbon monoxide must be minimized. This highlights the importance of the catalyst performance in the reaction. Ideally, the catalyst should be highly active in order to achieve large amounts of hydrogen, highly selective so that the carbon monoxide produced is negligible and finally it should present long-term stability.

1.4. Methanol steam reforming catalysts[29]

Since their development in 1960s that the copper-based catalysts are the most commonly used formulation in the methanol industry, mainly due to their high activity [30-34]. However, these catalysts are known for their pyrophoric characteristics and deactivation by thermal sintering [35, 36], which motivates the search for other types of catalysts. In comparison to Cu-based, group 8–10 catalysts have been reported in the literature [37-39] as highly stable and with similar

selectivity. However, concerning the catalytic activity, the later catalysts have in most studies the disadvantage of producing less hydrogen than the copper-based ones.

1.4.1. Copper-based catalysts

The most common catalysts for MSR are the copper-based ones. In order to improve their catalytic activity, several approaches are reported in the literature. Some studies are based on the addition of promoters [40-45], while others focus on the effect of the preparation method [46-50]. The later effect has been investigated by several authors, who found that each step can affect the properties of the catalyst. In other words, similar catalysts prepared by different methods can present distinct catalytic properties.

1.4.1.1. Status of copper catalysts: metal dispersion, surface area and particle size

The performance of copper-based catalysts is affected by the status of copper. More specifically, high values of copper dispersion and metal surface area, along with small particle sizes, are the targets to attain for the production of highly active catalysts. A summary of the physicochemical properties of various catalysts found in the literature is presented in Table 1.1. In its turn, the influence of the preparation method and promoter on the performance of the steam reforming reaction catalysts in presented in Table 1.2 and 1.3. To facilitate the comparison between different catalysts, some authors use the commercially available $CuO/ZnO/Al_2O_3$ catalyst as a reference [51-53].

An extensive variety of preparation methods can be found in the literature for the copper-based catalysts, namely the conventional co-precipitation [40, 54-56] and wet impregnation [53,57-59] methods. To enhance the catalytic activity and selectivity of the synthesised catalysts, some authors propose new preparation methods or a variation of the conventional ones. It is worth noticing that, in this study, selectivity is always towards the formation of CO unless said otherwise:

$$S_{CO} = \frac{F_{CO}}{F_{CO} + F_{CO_2}} \times 100 \quad (1.7)$$

where, F_{CO} and F_{CO2} are CO and CO_2 flow rates, respectively, and S_{CO} is the selectivity towards the formation of CO.

Table 1.1 - Physicochemical properties of copper catalysts found in the literature.

Catalyst	Preparation method	S_{BET} ($m^2 \cdot g^{-1}$)	S_{Cu} ($m^2 \cdot g^{-1}$)	Cu dispersion (%)
Cu/ZrO_2 [56]	IMP	13.1	1.0	-
Cu/ZrO_2 [56]	CP	64.2	3.5	-
Cu/ZrO_2 [56]	OGCP	71.5	18.4	-
Cu/ZnO [59]	CP	47.5	20.8	-
$Cu/ZnO/Al_2O_3$ [59]	CP	90.8	23.7	-
$Cu/ZnO/ZrO_2/Al_2O_3$ [59]	CP	129.7	25.9	-
Cu/Zn/Al [60]	WT	63.9	-	-
Cu/Zn/Al [60]	HS	84.5	-	-
Cu/Zn/Al [60]	CP	93.7	-	-
Cu/ZnO [40]	CP	40.7	16.0	-
Cu/ZnO [40]	HP	76.4	41.6	-
$Cu/ZnO/Al_2O_3$ [40]	HP	97.5	47.0	-
Cu/ZnO [61]	CP	48.6	20.8	9.6
$Cu/ZnO/Al_2O_3$ [61]	CP	91.9	22.2	11.3
$Cu/ZnO/ZrO_2$ [61]	CP	81.8	15.5	13.2
$Cu/ZnO/ZrO_2/Al_2O_3$ [61]	CP	116.2	23.3	23.2
Cu/Zn/Al [62]	WT	152	-	-
Cu/Zn/Ce/Al [62]	WT	162	-	-
Cu-Mn [63]	CP	9.6	-	-
Cu-Mn [63]	CP	55.2	-	-
Cu-Mn spinel [63]	SRG	118.1	-	-
CuO/CeO_2 [64]	CT	153	-	-
$CuMn_2O_4$ [64]	ST	144	-	-
$CuO/ZnO/Zr_2O_2$ [64]	CP	64	-	-

CP: Co-precipitation
CT: Carbon template
HP: Homogeneous precipitation
HS: Hydrothermal synthesis
IMP: Impregnation
OGCP: Oxalate gel co-precipitation
SRG: Soft reactive grinding technique
ST: Silica template
WT: Wet impregnation

Table 1.2 - Influence of the preparation method on the performance of different Cu-based catalysts for MSR.

Catalyst	Prep. method	*T* (°C)	X_{MeOH} (%)	Activity ($\mu mol_{H2} \cdot g_{cat}^{-1} \cdot s^{-1}$)	y_{CO}	S_{CO} (%)	W/F_0 $kg_{cat} \cdot mol^{-1} s$
Cu/ZrO_2 [56]	IMP	260	10	3	0	-	-
Cu/ZrO_2 [56]	CP	260	62	56	0.009	-	-
Cu/ZrO_2 [56]	OGCP	260	100	90	0.005	-	-
Cu/ZnO [40]	CP	250	46.4	51	-	0.4	-
Cu/ZnO [40]	HP	250	94.2	105	-	0.4	-
$Cu/ZnO/Al_2O_3$ [40]	HP	250	97.3	109	-	1	-
CuZn [65]	IMP	230	0	-	-	-	-
CuZn [65]	IMP	300	36.8	-	-	7.1	-
CuZn [65]	IMP-BD	230	59.5	-	-	0	-
CuZnZrAl [66]	SQ	260	61	-	-	4.5	150
CuZnZrAl [66]	CI-NP	260	63	-	-	3.0	150
CuZnZrAl [66]	CI	260	65	-	-	7.0	150
$Cu/Zn/Al_2O_3$ [66] (Commercial)	-	260	60	-	-	3.2	150
Cu-Mn [41]	OGCP	260	59.7	51	-	1.4	-
Cu-Mn [41]	CP	260	65.7	56	-	1.1	-
Cu-Mn spinel [41]	SRG	260	92.9	79	-	0.7	-
CuO/ZrO_2 [42]	PTSG	250	92	-	0.002	-	-
$CuO/ZnO/Al_2O_3$ [42] (Commercial)	-	250	92	-	0.1	-	-
Cu/Zn/Zr/Al [48]	WT	260	60	159	0.016	-	11.0
Cu/Zn/Zr/Al [48]	CP	260	97	261	0.008	-	11.0
Cu/ZnO [49]	CP	240	43.0	36	0.0018	-	
Cu/ZnO [49]	CP	240	48.6	41	0.0022	-	
Cu/ZnO [49]	SRG-C	240	52	44	0.0016	-	
Cu/ZnO [49]	SRG-N	240	70.9	59	0.0026	-	

CP: Co-precipitation

CI: Co-impregnation

CI-NP: Co-impregnation with nanoparticle precursor

HP: Homogeneous precipitation

IMP: Impregnation

IMP-BD: Modified impregnation with 1,3-butanediol

OGCP: Oxalate gel co-precipitation

PTSG: Polymer template sol-gel method

SQ: Sequential impregnation

SRG: Soft reactive grinding technique

SRG-N: Soft reactive grinding of oxalic acid with Cu/Zn nitrate precursors

SRG-C: Soft reactive grinding of oxalic acid with Cu/Zn carbonate precursors

WT: Wet impregnation

Promoters have been used to influence the status of copper and enhance the performance of the catalyst. Studies on the promotional effects of zirconia [59, 61] have revealed that this structural promoter decreases the CO selectivity – Table 1.3. For instances, Lindström *et al.* [50] studied the effect of zirconia in alumina-supported monolithic Cu-Zn catalysts. Although the Zr doped catalysts were less active than the ones without Zr, the selectivity towards CO_2 was higher. Jeong *et al.* [59] compared the performance of $Cu/ZnO/Al_2O_3$ to the one of $Cu/ZnO/ZrO_2/Al_2O_3$, and reported an increase of approximately 16 % in methanol conversion and a CO molar fraction 7.3 times lower, due to the presence of ZrO_2. Additionally, zirconia can promote copper dispersion as presented in Table 1.4. Agrell *et al.* [61] reported an increase of ca. 37.5 % in copper dispersion after adding ZrO_2 to Cu/ZnO catalyst. Finally, ZrO_2, as well as ZnO, can prevent copper particles from aggregation and help stabilize the crystal size of copper [68]. Another structural promoter is Al_2O_3, which provides a larger surface on which copper can be dispersed [59, 61]. Agrell *et al.* [61] observed an increase of both total surface area (48.6 to 91.9 $m^2 \cdot g^{-1}$) and copper dispersion (9.6 to 11.3 %) due to Al_2O_3 – Table 1.3. A similar effect can be attained by adding Cr_2O_3 [69, 70], which acts as stabilizer of the copper structure reducing sintering. The promotional effects of CeO_2 have been described in the literature [47, 52, 64, 70], in particular, Liu *et al.* [53] reported high activity of the Cu/CeO_2 catalysts compared to Cu/ZnO, Cu/Zn(Al)O and Cu/Al_2O_3 with the same Cu loading and under the same reaction conditions. It was suggested that the high activity of the Cu/CeO_2 catalysts was due to the highly dispersed Cu metal particles and the strong metal-support interaction between the Cu metal and CeO2 support. The catalytic activity has been reported to improve with the addition of yttria [71] which appears to stabilize a high copper surface area [72]. Finally, Houteit et al. [54] reports that cesium oxide can prevent copper oxide crystallites from sintering and its reduction into metallic Cu.

Table 1.3 - Influence of the type of promoter on the performance of different Cu-based catalysts for MSR.

Catalyst	T (°C)	X_{MeOH} (%)	Activity ($\mu mol_{H2} \cdot g_{cat}^{-1} \cdot s^{-1}$)	y_{CO}	S_{CO} (%)	W/F_0 $kg_{cat} \cdot mol^{-1} s$
Cu/ZnO [59]	260	75	-	0.0073	-	
Cu/ZnO/Al_2O_3 [59]	260	79	-	0.0073	-	
Cu/ZnO/ZrO_2/Al_2O_3 [59]	260	92	-	0.0010	-	
Cu/Zn/Al [73]	250	39	-	-	0.6	24.3
Cu/Zn/Zr/Al [73]	250	61	-	-	0.4	24.3
Cu/SiO_2 [74]	300	50	-	-	0.15	
ZnO/Cu/SiO_2 [74]	300	75	-	-	0.6	
Cu/Zn/Al_2O_3 [74] (Commercial)	300	57	-	-	1.1	
Cu/ZnO/Al_2O_3 [75] (Commercial)	270	59.0	-	-	-	8.0
Cu/ZnO/Al_2O_3 [75]	270	89.2	-	-	0.92	8.0
Cu/ZnO/ZrO2/Al_2O_3 [75]	270	92.4	-	-	0.97	8.0
Cu/ZnO/CeO_2/ZrO_2/Al_2O_3 [75]	270	89.4	-	-	0.85	8.0
Cu/ZnO/CeO_2/Al_2O_3 [75]	270	79.3	-	-	0.66	8.0
Cu/ZnO [61]	308	90	-	0.0014	-	
Cu/ZnO/Al_2O_3 [61]	305	90	-	0.0011	-	
Cu/ZnO/ZrO_2 [61]	295	90	-	0.0005	-	
Cu/ZnO/ZrO_2/Al_2O_3 [61]	278	90	-	0.00045	-	
Cu/Zn/Al [48]	260	76	203	0.011	-	
Cu/Zn/Ce/Al [48]	260	90	244	0.0006	-	
Cu/Zn/Al_2O_3 [76]	300	100	185	0.012	-	
Cu/Cr/Al_2O_3 [76]	300	63	117	0.011	-	
Cu/Zr/Al_2O_3 [76]	300	44	81	0.0075	-	
Cu-Cr_2O_3 [69]	240	-	28	-	5	
Cu-ZnO [69]	240	-	24	-	7	
Cu-CoO [69]	240	-	17	-	14	
CuO/CeO_2 [77]	250	80	75	-	-	
CuO/CeO_2/ZrO_2 [77]	250	-	97	-	-	
Cu/CeO_2 [53]	260	91	135	-	2.3	17.6
Cu/ZnO [53]	260	67	99	-	0.9	17.6
Cu/Zn(Al)O [53]	260	58	86	-	0.8	17.6
Cu/Al_2O_3 [53]	260	22	32	-	0.4	17.6
Cu-Mn-O [72]	240	99	-	-	3.1	
Cu-Ce-O [72]	240	37	-	-	0.8	
CuMn-spinel [78]	213	77	-	-	0.2	
non-spinel CuMn [78]	214	61	-	-	0.1	
CuZn [79]	250	39	-	0.0011	-	
Pd/CuZn [79]	250	47	-	0.003	-	
CuYPrAl [80]	320	99.1	120	-	0.2	25.0
CuCeAl [81]	350	99.8	16.7	0.0	-	

1.4.2. Group 8 – 10 Catalysts

The group 8 - 10 metal-based catalysts were firstly studied by Iwasa *et al.* [82-88]. Based on their preliminary findings, other authors have later studied the influence of several factors on the catalytic performance for MSR [36, 37, 89-98]. The most commonly used catalysts in this group are the palladium supported in zinc oxide (Pd/ZnO), due to its anomalous high performance after the formation of a PdZn alloy [83]. Accordingly, the preparation method and the pretreatment conditions of the Pd/ZnO catalysts have been thoroughly studied in the literature [89-94]. A different approach focused on the search of new types of supports, which presented higher surface areas than the commercially available ZnO support [38, 95-97]. Finally, other authors have synthesized catalysts based on different alloy species and studied the effect of Zn addition on bimetallic catalysts [39, 87, 99]. Table 1.4, presents a summary of the results obtained in the literature for the group 8-10 catalysts.

From the former review of results reported in the literature is easy to understand that ZnO is a common material in both groups of catalysts: copper-based and group 8-10. Despite being a controversy matter, the role of ZnO is proved to benefic for copper-based catalysts for stabilizing and increasing the dispersion of copper crystallites and in group 8-10 revelead to be essential for the formation of a selective alloy.

Table 1.4 - Summary table for MSR over various supported group 8–10 catalysts.

Catalyst	T (°C)	R.T. (°C)	Activity	S_{CO} (%)	X_{MeOH} (%)	S_{metal} (m^2 g^{-1})	Dispersion (%)
$Pd^{P1, L2}$ [87]	220	500	–	100	10.9	9.9	2.1
$Pd^{P2, L1}$ [83]	200	–	2.0	99.9	–	–	2.1
Pd/SiO_2 $^{P2, L1}$ [83]	200	–	0.13	100	–	–	7.2
Pd/SiO_2 $^{P2, L2}$ [100]	220	–	0.37	100	–	–	1.4
Pd/SiO_2 $^{P2, L2}$ [85]	220	500		100	0.09	–	–
Pd/SiO_2 $^{P1, L2}$ [87]	220	500		100	15.7	42.4	9
Pd/Al_2O_3 $^{P2, L1}$ [83]	200	–	1.9	98.6	–	–	13.1
Pd/La_2O_3 $^{P2, L1}$ [87]	200	–	3.1	92	–	–	5
Pd/Nd_2O_3 $^{P2, L1}$ [87]	200	–	3.7	93	–	–	25.3
Pd/Nb_2O_5 $^{P2, L1}$ [87]	200	–	1.5	95.8	–	–	19.6
$Pd/MgO^{P1,L2}$ [87]	220	500	–	93.4	41	49	10.4
Pd/In_2O_3 $^{P1, L2}$ [87]	220	250	–	4.5	28.3	9.9	2.1
Pd/Ga_2O_3 $^{P1, L2}$ [87]	220	500	–	5.4	21.2	12.3	2.6
Pd/CeO_2 $^{P1, L2}$ [87]	220	500	–	77.3	62.4	170.6	36.2
Pd/A.C.$^{P1, L2}$ [88]	220	500	–	100	2.3	–	–
Pd/HfO_2 $^{P1, L2}$ [88]	220	500	–	100	13.6	–	–
Pd/Ta_2O_5 $^{P1, L2}$ [88]	220	500	–	100	6.0	–	–
Pd/ZrO_2 $^{P2, L1}$ [83]	200	–	4.0	80	–	–	28.9
Pd/ZrO_2 $^{P1, L2}$ [87]	220	500	–	81.6	64.3	31.1	6.6
$Pd/ZnO^{P2, L1}$ [83]	200	–	8.3	3	–	–	10.7
$Pd/ZnO^{P1, L2}$ [87]	220	500	–	0.8	54.2	10.4	2.2
$Pd/ZnO^{P1, L2}$ [85]	220	500	–	1.9	56.3	–	–
Pd/ZnO $^{P2, L2}$ [85]	220	500	–	0.5	20.5	–	–
$Pt^{P1, L2}$ [87]	220	500	–	43.3	3	1.65	0.6
Pt/Ga_2O_3 $^{P1, L2}$ [87]	220	500	–	24.5	5.4	7.2	2.63
Pt/In_2O_3 $^{P1, L2}$ [87]	220	500	–	1.7	30.6	7.7	2.81
$Pt/ZnO^{P1, L2}$ [87]	220	500	–	4.6	27.6	7.1	2.58
$Pt/ZnO^{P1, L2}$ [85]	220	500	–	4.4	27.9	–	–
Pt/SiO_2 $^{P2, L2}$ [85]	220	500	–	74.4	0.3	–	–
Pt/SiO_2 $^{P2, L2}$ [100]	220	–	0.42	74.4	–	–	2.1
Pt/SiO_2 $^{P1, L2}$ [87]	220	500	–	81.2	10.3	92.3	33.5
$Ni/ZnO^{P1, L2}$ [85]	220	500	–	95.3	15.7	–	–
Ni/SiO_2 $^{P2, L2}$ [85]	220	500	–	98.9	7.3	–	–
Ni/SiO_2 $^{P2, L2}$ [100]	220	-	2.0	98.9	–	–	10.6
$Ni/ZnO^{P1, L2}$ [87]	220	500	–	97	19.1	2.7	0.4
$Co/ZnO^{P1, L2}$ [85]	220	500	–	91.1	20.3	–	–
$Co/ZnO^{P1, L2}$ [87]	220	500	–	86.7	13.1	6.2	0.92
$Ru/ZnO^{P1, L2}$ [88]	220	500	–	96.2	9.5	–	–
$Ir/ZnO^{P1, L2}$ [88]	220	500	–	79.6	2.6	–	–

P1: inlet partial pressure of water and methanol equal to 10.1 kPa. P2: inlet partial pressure of water and methanol equal to 24.3 kPa. L1: metal loading of 1 wt%. L2: metal loading of 10 wt%.R.T.: reduction temperature.

1.4.3. Zinc Oxide

Zinc oxide (ZnO) is a material that can be used for a wide range of applications and has a high added industrial value [101-103]. One of its major applications is in heterogeneous catalysis, for instance in the methanol reactions, as a main component in the catalysts for methanol synthesis or MSR [104-107]. Typically, ZnO has a wurtzite crystal structure, which is constituted by polar surfaces and non-polar surfaces. Surface studies indicate that the non-polar surfaces, $ZnO(10\bar{1}0)$ and $ZnO(10\bar{1}0)$, have a fairly low density of atomic defects such as vacancies and are electrostatic stable [108]. On the other hand, polar surfaces have unbalanced charges, one is terminated in Zn^{2+} and the other in O^{-2}, corresponding respectively to $Zn-ZnO(0001)$ and $O-ZnO(000\bar{1})$ planes of the crystal [109, 110]. The role of the specific crystallographic orientation of the exposed catalytic surface of ZnO and its morphology has been addressed in literature regarding methanol dissociation, more particularly for catalysts which are prepared using ZnO powder as a support. Karim *et al.* reported that faceted Pd/ZnO catalysts are more active for MSR [36]. Among the exposed surfaces, the polar $Zn-ZnO(0001)$ is considered to have an active pair of ions that readily dissociate methanol [112], whereas non-polar surfaces are not active for methanol dissociation [113]. The effect of different nanoshapes (short rods, long rods and polyhedral) of ZnO in MSR reaction were studied by Flytzani-Stephanopoulos *et al.*; these authors concluded that polyhedral shape was the most active for MSR, followed by the short rods and then for the long rods, due to the higher number of polar facets exposed [114]. Plane-density functional theory calculations performed by Guo *et al.* also indicate the contribution of polar facets for a low-temperature pathway reaction of MSR [115]; according to their calculations the dissociation of both water and methanol have low or null barriers on the polar $Zn-ZnO(0001)$.

Despite the attributed importance of the polar ZnO surfaces for catalysis, the non-polar surfaces are dominant in the commercially available ZnO powders [116]. These powders have a prismatic morphology where the non-polar surfaces correspond to six

of the exposed surfaces for chemical reactions (see Figure 1.5) [110]. Therefore, in the catalysis point of view, by increasing the polar surface ratio in comparison with the non-polar, the catalyst activity could be improved. Additionally, commercial ZnO has a low surface area, around 10 $m^2 \cdot g^{-1}$ [96].

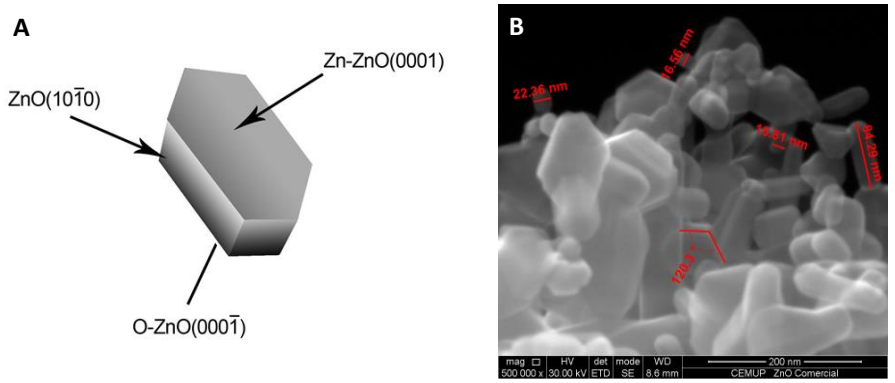

Figure 1.5 - Schematic representation of a commercially available ZnO crystal (A) and a SEM image of the ZnO material acquired to Sigma Aldrich under the framework of this thesis (B).

There are several methods for the synthesis of ZnO nanostructures being the hydrothermal method one of the most applied for its simplicity and mild conditions [117]. It is known that the growth velocities of the crystal planes in the hydrothermal method follow this preferential order: $V(0001) > V(1011) > V(1010)$ [118, 119]. Due to the faster growth in the $V(0001)$ plane direction the most exposed surfaces are the non-polar. This is easier to imagine in Figure 1.6, where a hexagonal unit cell of ZnO is represented and the growth along the c-axis would lead to higher proportion of non-polar facets.

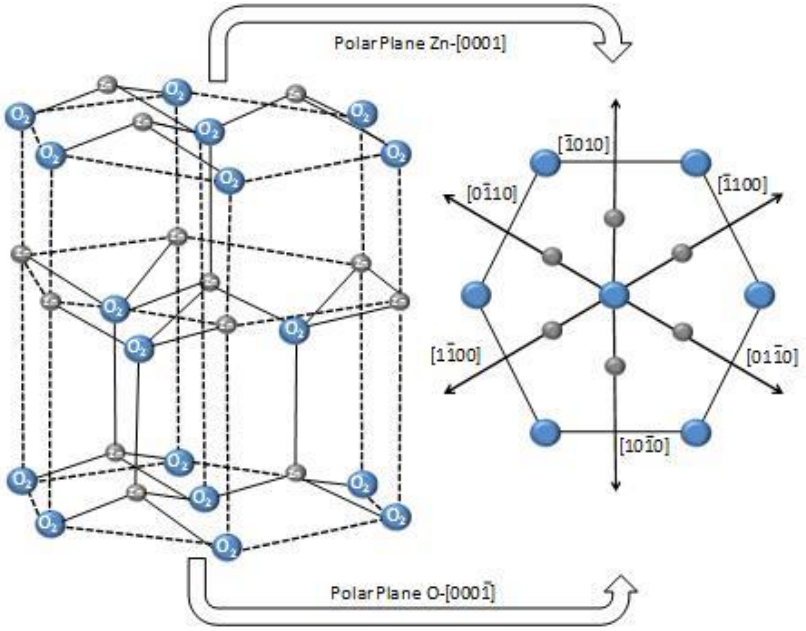

Figure 1.6 - - Schematic representation of the ZnO hexagonal unit cell.

In order to expose the polar ZnO facets, capping agents could be added to the synthesis method, since they can inhibit the growth in the *V*(0001) direction by chemical binding [101, 119, 120]. Block copolymers (i.e Pluronic P123) are well-known for their unique properties as template agents and structural polymorphism. The polyethylene oxide-polypropylene oxide polyethylene oxide (PEO-PPO-PEO) based triblock copolymers are an example of nonionic surfactants where the temperature, concentration and type of solvent medium extremely affect the molecular arrangement. Below the critical micellar temperature (CMT), molecules are present in solution in a non-aggregated state as unimers and they suffer a reorganization forming micelles above the CMT – Figure 1.7. These micelles are constituted by a hydrophobic core of PPO and a hydrophilic shell of PEO blocks.

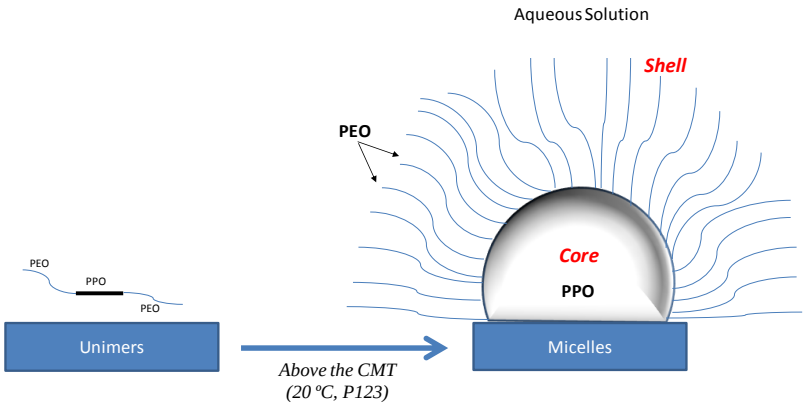

Figure 1.7 - Schematic representation of the molecular organization of Pluronic P123 below and above the CMT of 20 °C [121] in an aqueous solution (Legend: PEO is polyethylene oxide; PPO is polypropylene oxide).

There are many studies in the literature that report the behavior of triblock copolymers in water and their specific properties, such as CMT and cloud point (CP), however, only a few describe the interaction of urea with block copolymers in an aqueous medium. Recently, Jun-he Ma *et al.*, reported that urea has a direct interaction with the PEO shell of the block copolymer micelles [122]. In fact, when urea is dissolved in water, the polar urea molecules attach to the polar region of the micelles, replacing the water molecules around the PEO blocks, and directly interact through hydrogen bonds. Consequently, the hydrophobic core has an enhanced interaction with water and this increases the CMT from 20 °C to temperatures higher than 50 °C [122].

During this thesis work a urea-assisted hydrothermal synthesis method is described to control the physicochemical properties of ZnO.

1.5. Methanol Reformer and HT-PEMFC coupling

Coupling a HT-PEMFC with a methanol reformer that operates at the same temperature (< 200 ˚C) is an attractive configuration from the energy efficiency point of view. As consuming energy steps, the first one is the vaporization of the mixture water/methanol and further supply of energy to undergo the MSR reaction. Table 1,

presents the heat demand in each step at different operating temperatures of the reformer, per mol of methanol and considering a water/methanol molar feeding ratio of 1.5.

Table 1.5 - Energy consumption for heating the water/methanol mixture (molar ratio of 1.5) and for performing the MSR reaction.

Operating temperature of the reformer (°C)	Energy supply for heating the reactant mixture ($kJ \cdot mol^{-1}$)	MSR consumption ($kJ \cdot mol^{-1}$)	Total energy supply ($kJ \cdot mol^{-1}$)
170	109.2	55.8	165
180	109.8	56.2	166
190	110.5	56.6	167
200	111.1	57.0	168

The hydrogen electrochemical reaction in the HT-PEMFC anode is highly exothermic, and assuming an overall efficiency of 40 % it releases 144 kJ per mol of hydrogen fed. In the case of MSR, for each mol of methanol, three moles of hydrogen are produced, and therefore it gives a total of 432 kJ per mol of methanol available to supply the energy necessities of the reformer. This excess heat for methanol processing leads to an increase of the overall efficiency of the system. Jensen *et al.*, have performed heat balances for the possible utilization of the heat released by HT-PEMFC and report that 11.1 % of the methanol fuel energy can be saved by considering an operation of the reformer between the 150-200 °C [123].

Another alternative configuration that is reported in literature is the use of a burner to overcome the heat necessity of the first step of the process, which includes the fuel processing and the MSR reaction [123]. In this case, there are two choices of fuel to be used for the combustion: hydrogen or methanol. Conceptually, the source of hydrogen can be through the recycling of the tail gas from the fuel cell; on the other hand, methanol can be supplied from the reactant mixture or from the recycling of condensed and unreacted methanol. The enthalpy of combustion of hydrogen and methanol is respectively, -241.8 $kJ \cdot mol^{-1}$ and -685.8 $kJ \cdot mol^{-1}$ (lower heating value - LHV). Thus, the heat demand for vaporizing and perform MSR represents 68-69 % and 24-25 % of the fuel energy for hydrogen and methanol, respectively.

The integration of a HT-PEMFC with a methanol steam reformer for hydrogen production has been studied by Pan *et al.* [124]. Accordingly, it was studied the integration of a HT-PEMFC with a methanol reformer that was operated at low-temperatures: 180 °C, 190 °C and 200 °C. The methanol reformer was packed with 149 g of a $CuO/ZnO/Al_2O_3$ catalyst and the total conversion of methanol was achieved at 200 °C. The total hydrogen production of 50 $cm^3 \cdot h^{-1}$ was achieved by feeding the water/methanol mixture at a space time ratio of 578 $kg_{cat.} \cdot mol^{-1} \cdot s$. Hydrogen production was very dependent of the reaction temperature, increasing 2.5 times from 180 °C to 200 °C at total conversion conditions. CO production was similar for the different mixtures of water/methanol (molar ratio of 1.2, 1.5 and 2.0) and below the 0.2 % at 200 °C of operation temperature. This limit was accepted by the HT-PEMFC, and the loss of performance of the integrated system in comparison with a prepared mixture of 75 % H_2/25 % CO_2 was attributed to residual unreacted methanol that could entered the HT-PEMFC. This former study is an example of the importance of the reformer performance influence over the HT-PEMFC output energy, approaching several critical aspects related to the MSR catalyst kinetics. Despite, being possible to power the HT-PEMFC with the reformer operating at 185 °C, the conversion rate and the amount of hydrogen fed was significantly lower than the equivalent experiments at 220 °C [123].

A very interesting commercial example of the technology of HT-PEMFC combined with MSR is available from SerEnergy. This Danish company, is leader on the manufacturing power modules based on HT-PEMFCs, which has dedicated efforts on the development of hybrid systems with MSR. Figure 1.8 - presents a commercialized power source from SerEnergy, the H350 power system that is capable of supplying 350 W of power output. The former power source has been applied on auxiliary vehicles and also as a stationary back-up power unit.

Figure 1.8 - SerEnergy methanol power system H350 model [125].

1.6. Scope of thesis

The main purpose of this thesis was to study and develop highly efficient catalysts for MSR, which has a direct impact in the integration with HT-PEMFC technology. The synergetic integration of a HT-PEMFC with a methanol reformer operating at low-temperatures has the key challenge of improving the MSR state of art catalysts.

In **Chapter 1**, hydrogen limitations as a fuel for the environmentally friendly PEMFCs are presented. As an alternative, MSR provides an on-site generation of H_2 and takes into account all the advantages of the simplest of all alcohols, such as: reforming at low-temperatures, high energy density and easy transportation/storage. The importance of MSR is highlighted and ideally the catalysts should be highly active while producing low amounts of CO. The kinetic operation of the reformer at temperatures, below the 200 ˚C, is also presented as an attractive target for achieving a synergetic integration with the exothermic HT-PEMFCs.

In **Chapter 2**, an optimized hydrothermal synthesis method was deeply studied and allowed to control key properties of ZnO as a catalyst support: polarity, surface area and morphology. Afterwards, these physicochemical properties of the ZnO support were evaluated for MSR, by preparing CuO/ZnO catalysts using a simple

wetness impregnation method (**Chapter 3**). The polarity and surface area properties of ZnO revealed to influence both selectivity and activity. In the following chapter (**Chapter 4**), ZnO supports were prepared by the hydrothermal route and the influence of the calcination atmosphere was evaluated as an important preparation parameter to improve the activity of the Pd/ZnO catalysts. Finally in **Chapter 5**, a kinetic study was performed over a novel reported formulation CuZrDyAl, in the low-temperature range of MSR (170 °C, 180 °C, 190 °C and 200 °C). One empirical and two mechanistic models were adjusted to the experimentally obtained reaction rates.

1.7. References

[1] IEA (International Energy Agency) (2009).World Energy Outlook 2009. Paris: OECD/IEA.

[2] M. Ball, The hydrogen economy : opportunities and challenges. Cambridge University Press, 2009.

[3] IEA (International Energy Agency) (2013).World Energy Outlook 2013. Paris: OECD/IEA.

[4] A. Kirubakaran, S. Jain, R.K. Nema, A review on fuel cell technologies and power electronic interface, Renewable and Sustainable Energy Reviews, 13 (2009) 2430-2440.

[5] N. H. Behling, Fuel cells : current technology challenges and future research needs. Elsevier, 2013.

[6] R. O'Hayre, S.-W. Cha, W. Collela, F.B. Prinz, Fuel Cells Fundamentals, John Wiley & Sons, New York, 2006.

[7] Z. Lei, M. Sanjeev, Investigation of Durability Issues of Selected Nonfluorinated Proton Exchange Membranes for Fuel Cell Application, Journal of The Electrochemical Society, 153 (2006) A1062-A1072

[8] S. Wasmus, A. Küver, Methanol oxidation and direct methanol fuel cells: a selective review, Journal of Electroanalytical Chemistry, 461 (1999) 14-31.

[9] K. Scott, W.M. Taama, P. Argyropoulos, K. Sundmacher, The impact of mass transport and methanol crossover on the direct methanol fuel cell, Journal of Power Sources, 83 (1999) 204-216.

[10] A. Heinzel, V.M. Barragán, A review of the state-of-the-art of the methanol crossover in direct methanol fuel cells, Journal of Power Sources, 84 (1999) 70-74.

[11] D.R. Palo, R.A. Dagle, J.D. Holladay, Methanol Steam Reforming for Hydrogen Production, Chemical Reviews, 107 (2007) 3992-4021.

[12] S.J. Andreasen, S.K. Kær, S. Sahlin, Control and experimental characterization of a methanol reformer for a 350 W high temperature polymer electrolyte membrane fuel cell system, International Journal of Hydrogen Energy, 38 (2013) 1676-1684.

[13] Q. Li, R. He, J.A. Gao, J.O. Jensen, N.J. Bjerrum, The CO poisoning effect in PEMFCs operational at temperatures up to 200 °C, Journal of The Electrochemical Society, 150 (2003).

[14] http://www.fuelcelltoday.com, in 8-1-2014.

[15] http://www-toyota-global.com/innovation/environmental_technology/fuelcell_vehicle, in 12-10-2014.

[16] G.A. Olah, A. Goeppert, G.K.S. Prakash, Beyond Oil and Gas, Wiley, Los Angeles, 2006.

[17] G. Sandí, Hydrogen storage and its limitations, Electrochemical Society Interface, 13 (2004) 40-44.

[18] I. Cumalioglu, A. Ertas, Y. Ma, T. Maxwell, State of the art: Hydrogen storage, Journal of Fuel Cell Science and Technology, 5 (2008).

[19] A.Y. Esayed, Metal Hydrides, Energy Sources, Part A: Recovery, Utilization, and Environmental Effects, 23 (2001) 257 - 265.

[20] L. Zhou, Progress and problems in hydrogen storage methods, Renewable and Sustainable Energy Reviews, 9 (2005) 395-408.

[21] Christensen, C. H., Johannessen, T., Sørensen, R. Z. & Nørskov, J. K, Towards an ammonia-mediated hydrogen economy? Catalysis Today 111, (2006) 140–144.

[22] W.H. Cheng, H.H. Kung, Methanol Production and Use, New York, 1994.

[23]http://press.ihs.com/press-release/chemicals/driven-china-global-methanol-demand-rise-nearly-80-percent-2023-north-americ.

[24] P. Zegers, Fuel cell commercialization: The key to a hydrogen economy, Journal of Power Sources, 154 (2006) 497-502.

[25] Y. Chen, Y. Wang, H. Xu, and G. Xiong, Hydrogen production capacity of membrane reformer for methane steam reforming near practical working conditions, Journal of Membrane Science, 322 (2008) 453–459.

[26] S. Tosti, A. Basile, F. Borgognoni, V. Capaldo, S. Cordiner, S. Di Cave, F. Gallucci, C. Rizzello, A. Santucci, and E. Traversa, Low temperature ethanol steam reforming in a Pd-Ag membrane reactorPart 1: Ru-based catalyst, Journal of Membrane Science, 308 (2008) 250–257.

[27].B. Peppley, Methanol-steam reforming on $Cu/ZnO/Al_2O_3$. Part 1: The reaction network, Appl. Catal. A, 179 (1999) 21-29.

[28] B.A. Peppley, J.C. Amphlett, L.M. Kearns, R.F. Mann, Methanol steam reforming on $Cu/ZnO/Al_2O_3$ catalysts. Part 2. A comprehensive kinetic model, Appl. Catal., A, 179 (1999) 31-49.

[29] S. Sá, H. Silva, L. Brandão, J.M. Sousa, A. Mendes, Catalysts for methanol steam reforming—A review. Appl. Catal: B: Environ., 99 (2010) 43-57.

[30] K. Takahashi, N. Takezawa, H. Kobayashi, The mechanism of steam reforming of methanol over a copper-silica catalyst, Appl. Catal., 2 (1982) 363-366.

[31] C.J. Jiang, D.L. Trimm, M.S. Wainwright, N.W. Cant, Kinetic study of steam reforming of methanol over copper-based catalysts, Appl. Catal. A, 93 (1993) 245-255.

[32] Breen JP, Ross JRH. Methanol reforming for fuel-cell applications: development of zirconia-containing Cu–Zn–Al catalysts. Catalysis Today, 51 (1999) 521-533.

[33] B. Lindström, Hydrogen generation by steam reforming of methanol over copper-based catalysts for fuel cell applications, Int. J. Hydrogen Energy, 26 (2001) 923–933.

[34] J. Papavasiliou, G. Avgouropoulos, T. Ioannides, Production of hydrogen via combined steam reforming of methanol over CuO–CeO2 catalysts, Catal. Commun., 5 (2004) 231–235.

[35] C.-Z. Yao, L.-C. Wang, Y.-M. Liu, G.-S. Wu, Y. Cao, W.-L. Dai, H.-Y. He, K.-N. Fan, Effect of preparation method on the hydrogen production from methanol steam reforming over binary Cu/ZrO_2 catalysts, Appl. Catal. A, 297 (2006) 151–158.

[36] A.M. Karim, T. Conant, A.K. Datye, Controlling ZnO morphology for improved methanol steam reforming reactivity, Phys. Chem. Chem. Phys. , 10 (2008) 5584-5590.

[37] E.S. Ranganathan, S.K. Bej, L.T. Thompson, Methanol steam reforming over Pd/ZnO and Pd/CeO_2 catalysts, Appl. Catal., A 289 (2005) 153-162.

[38] T. Conant, A.M. Karim, V. Lebarbier, Y. Wang, F. Girgsdies, R. Schlögl, A. Datye, Stability of bimetallic Pd-Zn catalysts for the steam reforming of methanol, J. Catal., 257 (2008) 64-70.

[39] Y. Suwa, S.I. Ito, S. Kameoka, K. Tomishige, K. Kunimori, Comparative study between Zn-Pd/C and Pd/ZnO catalysts for steam reforming of methanol, Appl. Catal., A 267 (2004) 9-16.

[40] T. Shishido, Y. Yamamoto, H. Morioka, K. Takehira, Production of hydrogen from methanol over Cu/ZnO and Cu/ZnO/Al2O3 catalysts prepared by homogeneous

precipitation: Steam reforming and oxidative steam reforming, J. Mol. Catal. A: Chem., 268 (2007) 185–194.

[41] Q. Liu, L.-C. Wang, M. Chen, Y.-M. Liu, Y. Cao, H.-Y. He, K.-N. Fan, Waste-free Soft Reactive Grinding Synthesis of High-Surface-Area Copper–Manganese Spinel Oxide Catalysts Highly Effective for Methanol Steam Reforming, Catal. Lett., 121 (2008) 144–150.

[42] H. Purnama, F. Girgsdies, T. Ressler, J.H. Schattka, R.A. Caruso, R. Schomäcker, R. Schlögl, Activity and selectivity of a nanostructured CuO/ZrO2 catalyst in the steam reforming of methanol, Catal. Lett., 94 (2004) 61-68.

[43] T. Valdés-Solís, G. Marbán, A.B. Fuertes, Nanosized catalysts for the production of hydrogen by methanol steam reforming, Catal. Today, 116 (2006) 354–360.

[44] G. Marbán, T. Valdés-Solís, A.B. Fuertes, High Surface Area CuMn2O4 Prepared by Silica-Aquagel Confined co-precipitation. Characterization and Testing in Steam Reforming of Methanol (SRM), Catal. Lett., 118 (2007) 8–14.

[45] J. Papavasiliou, G. Avgouropoulos, T. Ioannides, Steam reforming of methanol over copper–manganese spinel oxide catalysts, Catal. Commun., 6 (2005) 497–501.

[46] J. Papavasiliou, G. Avgouropoulos, T. Ioannides, In situ combustion synthesis of structured Cu-Ce-O and Cu-Mn-O catalysts for the production and purification of hydrogen, Appl. Catal. B 66 (2006) 168–174.

[47] J. Papavasiliou, G. Avgouropoulos, T. Ioannides, Effect of dopants on the performance of CuO–CeO2 catalysts in methanol steam reforming, Appl. Catal. B, 69 (2007) 226–234.

[48] S. Patel, K.K. Pant, Influence of preparation method on performance of Cu(Zn)(Zr)-alumina catalysts for the hydrogen production via steam reforming of methanol, J. Porous Mater, 13 (2006) 373–378.

[49] L.-C. Wang, Y.-M. Liu, M. Chen, Y. Cao, H.-Y. He, G.-S. Wu, W.-L. Dai, K.-N. Fan, Production of hydrogen by steam reforming of methanol over Cu/ZnO catalysts prepared via a practical soft reactive grinding route based on dry oxalate-precursor synthesis, J. Catal., 246 (2007) 193–204.

[50] B. Lindström, L.J. Pettersson, Steam reforming of methanol over copper-based monoliths: the effects of zirconia doping, J. Power Sources, 106 (2002) 264–273.

[51] X. Huang, L. Ma, M.S. Wainwright, The influence of Cr, Zn and Co additives on the performance of skeletal copper catalysts for methanol synthesis and related reactions, Appl. Catal. A, 257 (2004) 235–243.

[52] X. Zhang, P. Shi, Production of hydrogen by steam reforming of methanol on CeO2 promoted Cu/Al2O3 catalysts, J. Mol. Catal. A: Chem., 194 (2003) 99–105.

[53] Y. Liu, T. Hayakawa, T. Tsunoda, K. Suzuki, S. Hamakawa, K. Murata, R. Shiozaki, T. Ishii, M. Kumagai, Steam reforming of methanol over Cu=CeO2 catalysts studied in comparison with Cu/ZnO and Cu/Zn(Al)O catalysts, Top. Catal., 22 (2003) 205-213.

[54] A. Houteit, H. Mahzoul, P. Ehrburger, P. Bernhardt, P. Légaré, F. Garin, Production of hydrogen by steam reforming of methanol over copper-based catalysts: The effect of cesium doping, Appl. Catal. A, 306 (2006) 22–28.

[55] M.M. Günter, T. Ressler, R.E. Jentoft, B. Bems, Redox Behavior of Copper Oxide/Zinc Oxide Catalysts in the Steam Reforming of Methanol Studied by in Situ X-Ray Diffraction and Absorption Spectroscopy, Journal of Catalysis, 203 (2001) 133-149.

[56] C.-Z. Yao, L.-C. Wang, Y.-M. Liu, G.-S. Wu, Y. Cao, W.-L. Dai, H.-Y. He, K.-N. Fan, Effect of preparation method on the hydrogen production from methanol steam reforming over binary Cu/ZrO_2 catalysts, Appl. Catal. A, 297 (2006) 151–158.

[57] B.L. Kniep, F. Girgsdies, T. Ressler, Effect of precipitate aging on the microstructural characteristics of Cu/ZnO catalysts for methanol steam reforming, J. Catal., 236 (2005) 34–44.

[58] M. Kurtz, H. Wilmer, T. Genger, O. Hinrichsen, M. Muhler, Deactivation of supported copper catalysts for methanol synthesis, Catal. Lett., 86 (2003) 77-80.

[59] H. Jeong, K.I. Kimb, T.H. Kimb, C.H. Ko, H.C. Park, I.K. Song, Hydrogen production by steam reforming of methanol in a micro-channel reactor coated with $Cu/ZnO/ZrO_2/Al_2O_3$ catalyst, J. Power Sources, 159 (2006) 1296–1299.

[60] J.-P. Shen, C. Song, Influence of preparation method on performance of Cu/Zn-based catalysts for low-temperature steam reforming and oxidative steam reforming of methanol for H2 production for fuel cells, Catal. Today, 77 (2002) 89–98.

[61] J. Agrell, H. Birgersson, M. Boutonnet, I. Melián-Cabrera, R.M. Navarro, J.L.G. Fierro, Production of hydrogen from methanol over Cu/ZnO catalysts promoted by ZrO2 and Al2O3, J. Catal., 219 (2003) 389–403.

[62] S. Patel, K.K. Pant, Activity and stability enhancement of copper–alumina catalysts using cerium and zinc promoters for the selective production of hydrogen via steam reforming of methanol, J. Power Sources, 159 (2006) 139–143.

[63] Q. Liu, L.-C. Wang, M. Chen, Y.-M. Liu, Y. Cao, H.-Y. He, K.-N. Fan, Waste-free Soft Reactive Grinding Synthesis of High-Surface-Area Copper–Manganese Spinel Oxide Catalysts Highly Effective for Methanol Steam Reforming, Catal. Lett., 121 (2008) 144–150.

[64] T. Valdés-Solís, G. Marbán, A.B. Fuertes, Nanosized catalysts for the production of hydrogen by methanol steam reforming, Catal. Today, 116 (2006) 354–360.

[65] O. Jakdetchai, N. Takayama, T. Nakajima, Activity Enhancement of CuZn-impregnated FSM-16 by Modification with 1,3-Butanediol for Steam Reforming of Methanol, Kinet. Catal., 46 (2005) 56–64.

[66] S.D. Jones, H.E. Hagelin-Weaver, Steam reforming of methanol over CeO_2- and ZrO2-promoted Cu-ZnO catalysts supported on nanoparticle Al2O3, Appl. Catal. B, 90 (2009) 195–204.

[67] G.-S. Wu, D.-S. Mao, G.-Z. Lu, Y. Cao, K.-N. Fan, The Role of the Promoters in Cu Based Catalysts for Methanol Steam Reforming, Catal. Lett., 130 (2009) 177–184.

[68] L. Ma, B. Gong, T. Tran, M.S. Wainwright, Cr_2O_3 promoted skeletal Cu catalysts for the reactions of methanol steam reforming and water gas shift, Catal. Today, 63 (2000) 499–505.

[69] X. Huang, L. Ma, M.S. Wainwright, The influence of Cr, Zn and Co additives on the performance of skeletal copper catalysts for methanol synthesis and related reactions, Appl. Catal. A, 257 (2004) 235–243.

[70] S. Patel, K.K. Pant, Influence of preparation method on performance of Cu(Zn)(Zr)-alumina catalysts for the hydrogen production via steam reforming of methanol, J. Porous Mater, 13 (2006) 373–378.

[71] W.-H. Cheng, I. Chen, J.-s. Liou, S.-S. Lin, Supported Cu catalysts with yttria-doped ceria for steam reforming of methanol, Top. Catal., 22 (2003) 225-233.

[72] P. Clancy, J.P. Breen, J.R.H. Ross, The preparation and properties of coprecipitated Cu–Zr–Y and Cu–Zr–La catalysts used for the steam reforming of methanol, Catal. Today, 127 (2007) 291–294.

[73] L. Yong-Feng, D. Xin-Fa, L. Wei-Ming, Effects of ZrO2-promoter on catalytic performance of CuZnAlO catalysts for production of hydrogen by steam reforming of methanol, Int. J. Hydrogen Energy, 29 (2004) 1617 – 1621.

[74] Y. Matsumura, H. Ishibe, Suppression of CO by-production in steam reforming of methanol by addition of zinc oxide to silica-supported copper catalyst, J. Catal., 268 (2009) 282–289.

[75] G. Huang, B.-J. Liaw, C.-J. Jhang, Y.-Z. Chen, Steam reforming of methanol over CuO/ZnO/CeO2/ZrO2/Al2O3 catalysts, Appl. Catal. A, 358 (2009) 7–12.

[76] B. Lindström, L.J. Pettersson, P.G. Menon, Activity and characterization of Cu/Zn, Cu/Cr and Cu/Zr on alumina for methanol reforming for fuel cell vehicles, Appl. Catal. A, 234 (2002) 111–125.

[77] H. Oguchi, T. Nishiguchi, T. Matsumoto, H. Kanai, K. Utani, Y. Matsumura, S. Imamura, Steam reforming of methanol over Cu/CeO2/ZrO2 catalysts, Appl. Catal. A, 281 (2005) 69–73.

[78] T. Fukunaga, N. Ryumon, N. Ichikuni, S. Shimazu, Characterization of CuMn-spinel catalyst for methanol steam reforming, Catal. Commun. , 10 (2009) 1800–1803.

[79] P. Bichon, M. Asheim, A. Jordal, T. Sperle, M. Fathi, A. Holmen, E.A. Blekkan, Hydrogen from methanol steam-reforming over Cu-based catalysts with and without Pd promotion, Int. J. Hydrogen Energy, 32 (2007) 1799 - 1805.

[80] H.-M. Yang, M.-K. Chan, Steam reforming of methanol over copper–yttria catalyst supported on praseodymium–aluminum mixed oxides, Catalysis Communications, 12 (2011) 1389-1395.

[81] M. Mrad, D. Hammoud, C. Gennequin, A. Aboukaïs, E. Abi-Aad, A comparative study on the effect of Zn addition to Cu/Ce and Cu/Ce–Al catalysts in the steam reforming of methanol, Applied Catalysis A: General, 471 (2014) 84-90.

[82] N. Iwasa, T. Mayanagi, N. Ogawa, K. Sakata, N. Takezawa, New catalytic functions of Pd-Zn, Pd-Ga, Pd-In, Pt-Zn, Pt-Ga and Pt-in alloys in the conversions of methanol, Catal. Lett., 54 (1998) 119-123.

[83] N. Iwasa, S. Kudo, H. Takahashi, S. Masuda, N. Takezawa, Highly selective supported Pd catalysts for steam reforming of methanol, Catal. Lett., 19 (1993) 211-216.

[84] N. Iwasa, S. Masuda, N. Ogawa, N. Takezawa, Steam reforming of methanol over Pd/ZnO: Effect of the formation of PdZn alloys upon the reaction, Appl. Catal., A 125 (1995) 145-157.

[85] N. Iwasa, S. Masuda, N. Takezawa, Steam reforming of methanol over Ni, Co, Pd and Pt supported on ZnO, React. Kinet. Catal. Lett., 55 (1995) 349-353.

[86] N. Iwasa, T. Mayanagi, S. Masuda, N. Takezawa, Steam reforming of methanol over Pd-Zn catalysts, React. Kinet. Catal. Lett., 69 (2000) 355-360.

[87] N. Iwasa, T. Mayanagi, W. Nomura, M. Arai, N. Takezawa, Effect of Zn addition to supported Pd catalysts in the steam reforming of methanol, Appl. Catal. A, 248 (2003) 153-160.

[88] N. Iwasa, N. Takezawa, New Supported Pd and Pt Alloy Catalysts for Steam Reforming and Dehydrogenation of Methanol, Top. Catal., 22 (2003) 215-224.

[89] Y.H. Chin, R. Dagle, J. Hu, A.C. Dohnalkova, Y. Wang, Steam reforming of methanol over highly active Pd/ZnO catalyst, Catal. Today, 77 (2002) 79-88.

[90] Y.H. Chin, Y. Wang, R.A. Dagle, X.S. Li, Methanol steam reforming over Pd/ZnO: Catalyst preparation and pretreatment studies, Fuel Process. Technol., 83 (2003) 193-201.

[91] R.A. Dagle, Y.H. Chin, Y. Wang, The effects of PdZn crystallite size on methanol steam reforming, Top. Catal., 46 (2007) 358-362.

[92] A. Karim, T. Conant, A. Datye, The role of PdZn alloy formation and particle size on the selectivity for steam reforming of methanol, J. Catal., 243 (2006) 420-427.

[93] Y. Wang, J. Zhang, H. Xu, Interaction between Pd and ZnO during Reduction of Pd/ZnO Catalyst for Steam Reforming of Methanol to Hydrogen, Chin. J. Catal., 27 (2006) 217-222.

[94] Y. Wang, J. Zhang, H. Xu, X. Bai, Reduction of Pd/ZnO catalyst and its catalytic activity for steam reforming of methanol, Chin. J. Catal., 28 (2007) 234-238.

[95] I. Eswaramoorthi, A.K. Dalai, A comparative study on the performance of mesoporous SBA-15 supported Pd-Zn catalysts in partial oxidation and steam reforming of methanol for hydrogen production, International Journal of Hydrogen Energy, 34 (2009) 2580-2590.

[96] G. Xia, J.D. Holladay, R.A. Dagle, E.O. Jones, Y. Wang, Development of Highly Active Pd-ZnO/Al_2O_3 Catalysts for Microscale Fuel Processor Applications, Chem. Eng. Technol., 28 (2005) 515-519.

[97] X. Guangwei, L. Laitao, L. Changquan, Y. Xiaomao, Synthesis of mesoporous ZnO (m-ZnO) and catalytic performance of the Pd/m-ZnO catalyst for methanol steam reforming, Energy Fuels, 23 (2009) 1342-1346.

[98] S. Penner, B. Jenewein, H. Gabasch, B. Klötzer, D. Wang, A. Knop-Gericke, R. Schlögl, K. Hayek, Growth and structural stability of well-ordered PdZn alloy nanoparticles, J. Catal., 241 (2006) 14-19.

[99] S.I. Ito, Y. Suwa, S. Kondo, S. Kameoka, K. Tomishige, K. Kunimori, Steam reforming of methanol over Pt-Zn alloy catalyst supported on carbon black, Catal. Commun. , 4 (2003) 499-503.

[100] N. Takezawa, N. Iwasa, Steam reforming and dehydrogenation of methanol: Difference in the catalytic functions of copper and group VIII metals, Catal. Today, 36 (1997) 45-56.

[101] Yahiro, J., T. Kawano, and H. Imai, Nanometric morphological variation of zinc oxide crystals using organic molecules with carboxy and sulfonic groups, Journal of Colloid and Interface Science, 310 (2007) 302-311.

[102] Luo, H., et al., Surfactant-Templated mesoporous metal oxide nanowires, J. Nanomaterials, (2010) 1-6.

[103] Meyer, B. and D. Marx, Density-functional study of the structure and stability of ZnO surfaces, Physical Review B, 67 (2003) 391-403.

[104] Meyer, B. and D. Marx, Density-functional study of Cu atoms, monolayers, films, and co adsorbates on polar ZnO surfaces, Physical Review B, 69 (2004) 412-420.

[105] Ostendorf, F., S. Torbrügge, and M. Reichling, Atomic scale evidence for faceting stabilization of a polar oxide surface, Physical Review B, 77 (2008) 391-405.

[106] Spencer, M.S., The role of zinc oxide in Cu/ZnO catalysts for methanol synthesis and the water–gas shift reaction. Topics in Catalysis, 8 (1999) 259-266.

[107] Wilmer, H., et al., Methanol synthesis over ZnO: A structure-sensitive reaction? Physical Chemistry Chemical Physics, 5 (2003) 4736-4742.

[108] Yin, X.-L., et al., Adsorption of atomic hydrogen on ZnO(10-10): STM study. Physical Chemistry Chemical Physics, 8 (2006) 1477-1481.

[109] Dulub, O., M. Batzill, and U. Diebold, Growth of Copper on Single Crystalline ZnO: Surface Study of a Model Catalyst, Topics in Catalysis, 36 (2005) 65-76.

[110] Wöll, C., The chemistry and physics of zinc oxide surfaces. Progress in Surface Science, 82 (2007) 55-120.

[111] Vohs, J.M. and M.A. Barteau, Conversion of methanol, formaldehyde and formic acid on the polar faces of zinc oxide, Surface Science, 176 (1986) 91-114.

[112] Cheng, W.H., S. Akhter, and H.H. Kung, Structure sensitivity in methanol decomposition on ZnO single-crystal surfaces, Journal of Catalysis, 82 (1983) 341-350.

[113] Boucher, M.B., et al., 'Shape effects' in metal oxide supported nanoscale gold catalysts, Physical Chemistry Chemical Physics, 13 (2011) 2517-2527.

[114] Smith, G.K., et al., Initial steps in methanol steam reforming on PdZn and ZnO surfaces: Density functional theory studies, Surface Science, 605 (2011) 750-759.

[115] Burton, P., et al., Synthesis of High Surface Area ZnO(0001) Plates as Novel Oxide Supports for Heterogeneous Catalysts. Catalysis Letters, 139 (2010) 26-32.

[116] Baruah, S. and J. Dutta, Hydrothermal growth of ZnO nanostructures. Science and technology of advanced materials, 1 (2009) 013001.

[117] Pérez-Hernández, R., et al., Hydrogen Production by Steam Reforming of Methanol over a Ag/ZnO One Dimensional Catalyst, Advanced Materials Research, 132 (2010) 205-219.

[118] Tang, Q., et al., A template-free aqueous route to ZnO nanorod arrays with high optical property, Chemical Communications, 6 (2004) 712-713.

[119] Qiu, Y., W. Chen, and S. Yang, Facile hydrothermal preparation of hierarchically assembled, porous single-crystalline ZnO nanoplates and their application in dye-sensitized solar cells. Journal of Materials Chemistry, 20 (2010) 1001-1006.

[120] Zhang, H., et al., Self-assembly fabrication of 3D flower-like ZnO hierarchical nanostructures and their gas sensing properties, CrystEngComm, 14 (2012) 1775-1782.

[121 Kadam, Y., et al., Micelles from PEO–PPO–PEO block copolymers as nanocontainers for solubilization of a poorly water soluble drug hydrochlorothiazide, Colloids and Surfaces B: Biointerfaces, 83 (2011) 49-57.

[122] Ma, J.-h., et al., Interaction of Urea with Pluronic Block Copolymers by 1H NMR Spectroscopy, The Journal of Physical Chemistry B, 111 (2007) 5155-5161.

[123] J.O. Jensen, Q. Li, C. Pan, A.P. Vestbø, K. Mortensen, H. Nybo Petersen, C. Lau Sørensen, T. Nedergaard Clausen, J. Schramm, N.J. Bjerrum, High temperature PEMFC and the possible utilization of the excess heat for fuel processing, International Journal of Hydrogen Energy, 32 (2007) 1567-1571.

[124] C. Pan, R. He, Q. Li, J.O. Jensen, N.J. Bjerrum, H.A. Hjulmand, A.B. Jensen, Integration of high temperature PEM fuel cells with a methanol reformer, Journal of Power Sources, 145 (2005) 392-398.

[125] http://serenergy.com/products/systems/h3-350/, in 22-10-2014.

Chapter 2

The contributions of the author of this thesis in the following chapter are: definition of the scientific problem - study of the hydrothermal route for tuning physicochemical properties of ZnO materials pointed out in literature as influencing factors for MSR catalytic systems; performance of experimental work (e.g. hydrothermal synthesis, specific surface area measurements, thermogravimetric analysis, photocatalytic activity); interpretation and discussion of the results. Writing of a first version of the manuscript results that had the important contribution of Dr. Cecilia Mateos Pedrero and Professor Adélio Mendes for obtaining the final version of the manuscript, which was revised by all the co-authors. The author of this thesis had a percentual contribution as part of the research team of 25 %.

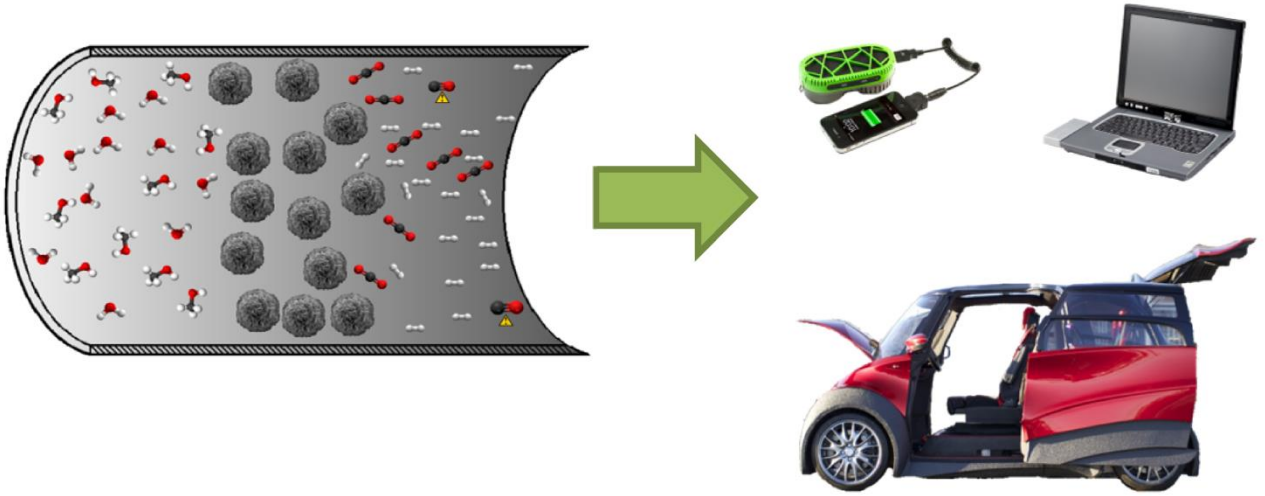

Chapter 2. Simple Urea-assisted Hydrothermal Synthesis Method for Tailoring the Physicochemical Properties of ZnO – Morphology, Surface Area and Polarity[1]

Abstract

A simple urea-assisted hydrothermal synthesis method was used to tailor the physicochemical properties of ZnO materials. The role of Pluronic P123 block copolymer in the crystal growth, morphology and specific surface area of the as-prepared ZnO was studied. When Pluronic P123 is used, well-dispersed hierarchical microspheres, with a flower-like morphology, are obtained, but in its absence large spherical agglomerated clusters are formed. The polarity of the ZnO, measured as the ratio between plane (002) and plane (100), is also significantly higher for the Pluronic P123 sample. The influence of zinc salt precursors was also analysed. The use of zinc nitrate led to the formation of urchin-like ZnO structures, instead of the microflowers that result from zinc acetate salt. Despite having similar surface areas, the polarity of the zinc nitrate sample was much smaller. The decomposition of methylene blue corroborated the higher photocatalytic activity of the ZnO materials with a higher proportion of polar planes (higher polarity). The formation mechanism of the crystals is also suggested based on the observed gradual growth and assembly of the hydrozincite during the initial steps of the synthesis for the samples with and without Pluronic P123.

[1] Silva, H., Mateos-Pedrero, C., Magen, C., Pacheco Tanaka, D. A., & Mendes, A. (2014). Simple hydrothermal synthesis method for tailoring the physicochemical properties of ZnO: morphology, surface area and polarity. *RSC Advances*, *4*(59), 31166–31176.

2.1. Introduction

ZnO is a semiconductor material that has attracted research interest during the last few years, mainly focusing in application-related aspects [1-3]. Among the wide range of multifunctional applications it is possible to highlight the following high-technology uses: emitting diodes [4], piezoelectric transducers [5], lasers [6], hydrogen sensors [5], biosensors [6] and inorganic antimicrobial agents [7]. Tailoring the main properties of such a versatile marterial towards a performance enhancement is of critical importance. Presently, looking inside the catalysis field, including photocatalysis, there is a continuous search of ZnO nanostructures that contain high surface areas and a large number of surface defects. These key propertities have proved to be valuable in methanol reactions, such as methanol steam reforming and methanol synthesis [8-11], and in photocatalysis where ZnO is pointed to be a suitable alternative of TiO_2 [12, 13].

ZnO has a würtzite crystalline structure with unbalanced charges either terminated in Zn^{2+} or O^{2-}, corresponding, respectively to $Zn-ZnO(0001)$ and $O-ZnO(000\bar{1})$ polar planes [14, 15]. The basal polar planes of ZnO were reported to be much more active in photocatalysis as compared to the non-polar facets, due to a higher density of defects such as oxygen vacancies [16]. Plane-density functional theory calculations performed by Guo *et al.* also indicate the contribution of polar facets for a low-temperature pathway reaction of methanol steam reforming [17]; according to their calculations the dissociation of both water and methanol have low or null barriers on the polar Zn – ZnO (0001). The effect of different nanoshapes of ZnO in methanol steam reforming and water gas-shift reactions was studied by Flytzani-Stephanopoulos *et al.* and the activity was higher with the increasing number of polar facets exposed [18]. According to the former studies, is easy to understand that a large surface area (0001) ZnO is beneficial from the catalysis point of view.

Different synthesis methods for preparing highly faceted nanostructures, which expose mainly polar planes, were investigated. For instance, Li *et. al*, prepared ZnO with various morphologies using a hydrothermal route [19]. The morphology of the

ZnO hexagonal planes presented a high proportion of polar planes and nevertheless the surface area was very low: 4.6 $m^2 \cdot g^{-1}$. A similar hexagonal plate-like morphology was produced by Mclaren *et al.* using a chemical synthetic route and oleic acid as capping agent, proving to be very effective towards the decomposition of methylene blue [20]. However, in the former study there is no mention to the surface area of ZnO. A non-hydrolytic aminolysis synthesis route was used for the preparation of nanocones with predominant [0001] polar planes but again the surface area was as low as 17.3 $m^2 \cdot g^{-1}$ [21]. Burton *et al.*, investigated routes for obtaining a high surface area ZnO material with increased proportion of polar planes using sodium citrate; these authors used a capping agent for blocking the growth along the [0001] direction [22]. Unfortunately, despite had achieving a highly faceted morphology the surface area dropped from 96 $m^2 \cdot g^{-1}$ to 48 $m^2 \cdot g^{-1}$ when the calcination temperature was raised from 120 °C to 340 °C, respectively; this former temperature corresponded to ZnO without traces of reactant intermediates. Therefore, it was concluded that the developed ZnO did not presented the desired thermal stability.

Thermally stable 3D microspheres of ZnO with a high surface area and proportion of polar planes were prepared in this work. The photocatalytic performance of the optimized materials was successfully tested in the decomposition of blue methylene. The hydrothermal method was followed due to its simplicity, low cost, high yields, easy scaling up, facile control over nanocrystal growth and mild conditions requirements [23]. It is known that the growth velocities (*V)* of the crystal planes follow this preferential order: $V(0001) > V(1011) > V(1010)$ due to the differences in surface energy between the planes [24, 25]. However, the slow hydrolyses of urea and the presence of block copolymer P123 as template agent inhibited the growth in the (0001) direction. The obtained ZnO materials were characterized by N_2 physisorption, electron energy disperse spectroscopy (EDS) in combination with scanning electron microscopy (SEM), high resolution transmission electron microscopy (HR-TEM) with selective area electron diffraction (SAED), X-ray powder diffraction (XRD), differential scanning calorimetry-thermal gravimetric analysis (DSC-TGA) and X-ray photoelectron spectroscopy (XPS).

2.2. Experimental

2.2.1. Synthesis of ZnO samples

Zinc acetate dihydrate ($Zn(CH_3COO)_2 \cdot 2H_2O$; 99.0%), zinc nitrate hexahydrate ($Zn(NO_3)_2 \cdot 6H_2O$; 98.0%), urea ($CO(NH_2)_2$; 99.5%), glacial acetic acid (CH_3COOH; 99.7%), block copolymer poly(ethylene glycol)-*block*-poly(propylene glycol)-*block*-poly(ethylene glycol) (Pluronic P123, PEG_{20}-PPG_{70}-PEG_{20}), all analytical grade reactants were obtained from Sigma-Aldrich and used without further purification. Distilled water was used throughout the experiments. In a typical synthesis the ZnO support precipitate was obtained as following: 5 mmol of zinc salt precursor (acetate or nitrate, Table 2.1), 100 mmol of urea and given amounts of Pluronic P123 (Table 2.1) were mixed in 100 ml of distilled water. The pH of the solution was adjusted to 5.0 with glacial acetic acid and stirred for 2 h under ambient conditions. Then, the mixture was poured into a 150 ml Teflon-lined autoclave and maintained at a given temperature (Table 2.1) for 24 h and cooled down to room temperature naturally. The white precipitate was thoroughly washed with distillated water and dried overnight at 110 °C. The final ZnO powder was obtained after calcination in a muffle furnace at a given temperature (Table 2.1) for 30 minutes.

2.2.2. Characterization

The specific surface area (S_{BET}) of the ZnO materials was determined by standard N_2 gas adsorption method using a Quantachrome Autosorb-1 apparatus. XRD measurements were taken on a Rigaku Miniflex 2. SEM analysis was performed using a FEI Quanta 400 scanning electron microscope equipped with an energy dispersive X-ray high vaccum detector (EDX). HRTEM/SAED images were obtained using a FEI Titan High Base microscope. DSC-TGA analyses were performed using a Netzsch TG 209 F1 Iris instrument. The photocatalytic activity of selected ZnO samples was assessed based on the decomposition of methylene blue (MB solution: 0.01 $g \cdot L^{-1}$). During the experiments, 100 ml of solution was poured

into a glass flask with 50 mg of ZnO. A UV lamp (Vilber Lourmat, BLB 365 nm, 2 x 6 W) was placed over the solution and maintained at the same distance during the experimental tests (irradiance of 10 $W \cdot m^{-2}$). The extent of MB degradation was determined measuring the absorbance of the solution at 645 nm. XPS analyses were performed using a Kratos Axis Ultra HSA equipment, with Vision software for data acquisition and CASA XPS software for data analysis. The analysis was carried out with a monochromatic Al Kα X-ray source (1486.7 eV), operating at 15 kV. For the quantification of the elements, sensibility factors provided by the manufacturers were used. For these experiments, Zn 2p, O 1s and C 1s bands were recorded. The binding energies were calibrated by fixing the C-(C, H) contribution of the C 1s adventitious carbon at 285.0 eV.

2.3. Results and discussion

2.3.1. Characterization of the ZnO precursor: the role of Pluronic P123

The thermal decomposition of the ZnO precursor (before calcination) for the samples prepared in the absence ($Zn_{Ac}P0T90$) and presence of Pluronic P123 ($Zn_{Ac}P10T90$, Table 2.1) was examined by TG-DSC.

The following nomenclature for the prepared ZnO samples was used (Table 2.1), $Zn_xP_yT_z$, where: x denotes the zinc precursor, zinc-acetate (Ac) or zinc-nitrate (N); Py stands for the amount of Pluronic P123 expressed as (n_{P123}/n_{Ac}) molar ratio percentage (Table 2.1) and Tz represents the synthesis temperature in ˚C (Table 2.1). Accordingly, the $Zn_{Ac}P_{10}T_{90}$ sample was prepared from zinc-acetate as precursor, with a (n_{P123}/n_{Ac}) molar ratio percentage of 10 and at 90 ˚C.

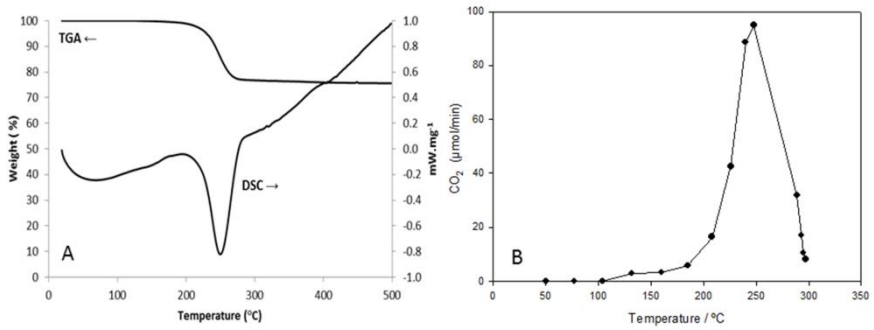

Figure 2.1 - (A) TGA-DSC analyses of the ZnO-precursor (before calcination at heating rate of $10°\cdot min^{-1}$ in static air for $Zn_{Ac}P10T90$sample; (B) thermal decomposition of the ZnO-precursor (HZC) followed by mass spectroscopy

The TG-DSC results obtained for sample $Zn_{Ac}P_{10}T_{90}$ are shown in Figure 2.1-A. As depicted in this figure, this sample was decomposed in only one fast step, denoted by a sharp peak centered at 250 °C. This was accompanied by a weight loss of 26 % in the temperature interval of 175-300 °C. The sample prepared without P123 behave similarly (results not shown here). In fact both samples exhibit the same TG profile, indicating that Pluronic P123 was removed during the washing step.

The evolution of the CO_2 during the thermal decomposition of Zn_{Ac}P10T90 sample was followed by mass spectroscopy. As shown in Figure 2.1-B, a large CO_2 peak is observed centered at 250 °C, in agreement with TG-DSC data. The decomposition value for the zinc hydroxycarbonate (hydrozincite) according to equation (2.1) is 26.3 wt.%, which is in good agreement with the TG results (26 %).

$$Zn_5(CO_3)_2(OH)_6 \rightarrow 5ZnO + 3H_2O + 2CO_2 \qquad (2.1)$$

On the other hand, according to the XRD pattern of both samples (not shown), all the diffraction peaks could be indexed as hydrozincite (hereafter referred to as HZC, Fig. 2.2), $Zn_5(CO_3)_2(OH)_6$, (JCPDS Card No. 19-1458).

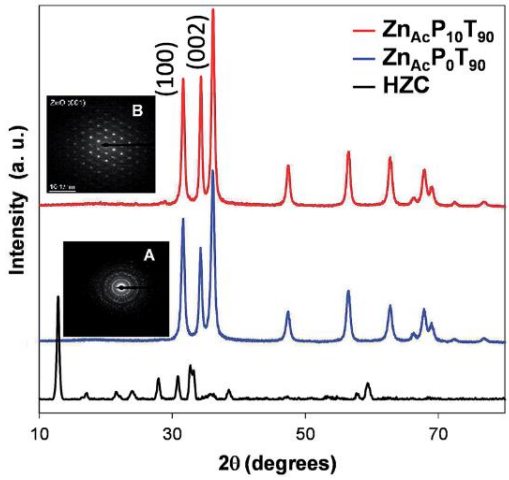

Figure 2.2 - XRD pattern of $Zn_5(CO_3)_2(OH)_6$ precursor (HZC) and ZnO samples prepared in the absence (Zn_{Ac}P0T90) and presence of Pluronic P123 (Zn_{Ac}P10T90) after calcination at 375 °C for 30 minutes. Inset (A): SAED pattern of Zn_{Ac}P0T90 sample. Inset (B): SAED pattern of Zn_{AC}P10T90 sample.

The effect of Pluronic P123 on the morphology of the as-prepared HZC samples (before calcination) is nicely illustrated in Figure 2.3. In the absence of additive, spherical clusters of HZC appear to be agglomerated forming larger clusters of about 200 μm (Figure 2.3-A). The addition of Pluronic P123 resulted in well-dispersed microspheres (Figure 2.3-B), which are in fact microflower-like in morphology (inset Figure 2.3-B).

Comparing images in Figure 2.3, it is clear that spherical HZC architectures are obtained, regardless of Pluronic P123 content, being the main difference the higher dispersion of these microspheres in the presence of Pluronic P123. The calcination effect on the structure and morphology of the resulting ZnO solids (from HZC prepared in the absence and presence of Pluronic P123) was analyzed by XRD and SEM.

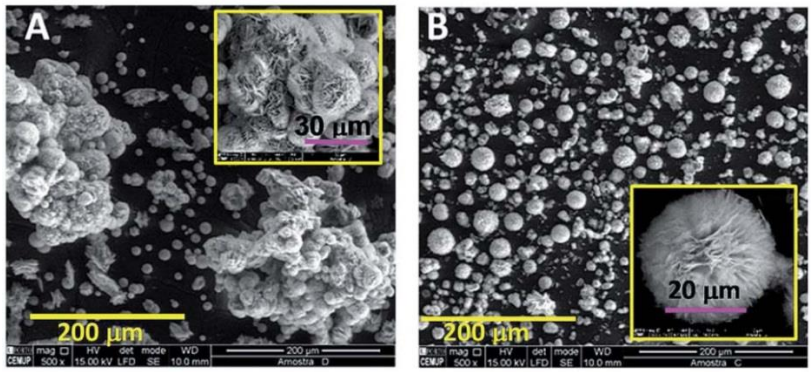

Figure 2.3 - SEM images of the as-prepared HZC samples obtained in the absence (A) and presence of Pluronic P123 (B) (n_{P123}/n_{ZnAc} molar ratio = 0.10).

It is important to mention that repetition of the synthesis under identical conditions led to similar results. SEM micrographs in Figure 2.4 reveal very different morphologies for both samples. In the absence of Pluronic P123 (Figure 2.4-A) non homogeneous ZnO structures ($Zn_{Ac}P_0T_{90}$), consisting of a combination of plates and spheres, were formed. The enlarged SEM image of one single sphere in Figure 2.4-B-C, shows that it is composed of randomly close-packed porous nanosheets.

On the contrary, in the presence of Pluronic P123 (sample Zn_{Ac}P10T90) well-dispersed ZnO microspheres were obtained (Figure 2.4-D). Moreover, SEM images in Figure 2.4-D and E clearly show that the ZnO product calcined at 375 °C inherited the flower-like morphology of the HZC precursor (Figure 2.3-B), evidencing its thermal stability.

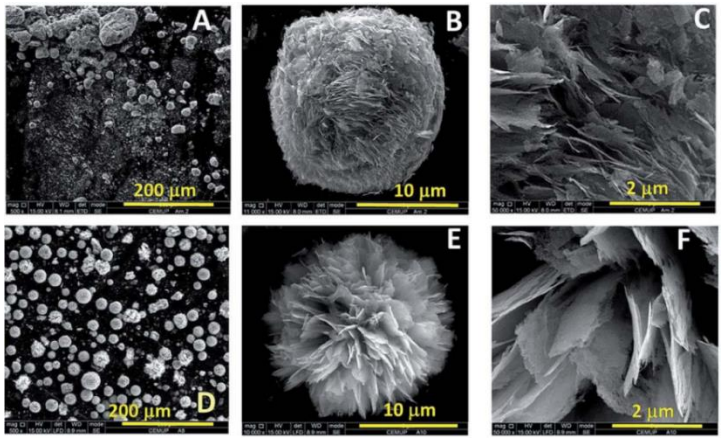

Figure 2.4 - Low and high magnification SEM images of ZnO samples Zn_{Ac}P0T90 (A-C) and Zn_{Ac}P10T90 (D-F).

According to Figure 2.4-D-F, calcination of HZC resulted in ZnO samples (sample Zn_{Ac}P10T90) made up of micro-flowers uniformly distributed and of smaller diameter (21 µm) than those seen in the HZC precursor (35 µm) (Figure 2.3-B). Detailed observation of a single micro-flower in Figure 2.4-E shows that they are in fact an assembly of nanosheets that grow radially from the center outward, and the entire structure resembles a carnation. The micro-flowers in Zn_{Ac}P10T90 sample show a lot of voids between the various nanosheets (Figure 2.4-E and F), in opposition to the compact structure shown by the Zn_{Ac}P0T90 sample (prepared without Pluronic P123; Figure 2.4-B and C). This is also reflected in the higher specific surface area that is 43% larger for sample Zn_{Ac}P10T90 (80 $m^2 \cdot g^{-1}$) than that of the sample Zn_{Ac}P0T90 (46 $m^2 \cdot g^{-1}$). Thus, the presence of Pluronic P123 helps to enhance the formation of spherical ZHC structures during the hydrothermal synthesis. As a result the ZnO product obtained after calcination, inherits the flower-like morphology of the ZHC precursor maintaining also the high dispersion.

The XRD patterns of Zn_{Ac}P0T90 and Zn_{Ac}P10T90 samples are shown in Figure 2.2 with an SAED image of each nanostructure in the inset.

It is found that both samples are highly crystalline, and the diffraction peaks in every pattern can be indexed to hexagonal würtzite-type ZnO (JCPDS No. 36–1451).

No other phases were detected indicating pure ZnO samples. Further EDX results confirmed that the ZnO samples were composed of solely Zn and O. However, the diffraction intensity ratios of (002) polar plane to (100) nonpolar plane are clearly different from one sample to another. In the present work, the term "polarity" is used to refer the relative intensities ratio of the polar and the nonpolar planes, ($I_{(002)}/I_{(100)}$). In this way, intensity ratio values higher than the würtzite reference ($I_{(002)}/I_{(100)}$= 0.73) denote a higher polarity, and consequently a higher ratio of exposed polar facets, and *vice versa*. The polarity values ($I_{(002)}/I_{(100)}$) for samples Zn_{Ac}P0T90 and Zn_{Ac}P10T90 are 0.74 and 1.10, respectively. Clearly, the former sample shows the same polarity as the reference würtzite whereas the later has a higher polarity. This indicates that the use of Pluronic P123 enhances the polarity of the ZnO material.

SAED patterns were also obtained of samples Zn_{Ac}P0T90 and Zn_{Ac}P10T90 (insets A and B in Figure 2.2). The Zn_{Ac}P0T90 sample shows a diffraction pattern characteristic of a fully polycrystalline material with preferential growth along the *c*-axis direction (inset A in Figure 2.2). On the other hand, the SAED pattern of the Zn_{Ac}P10T90 sample, confirms that they are single crystals (inset B in Figure 2.2).

These results demonstrate that the addition of Pluronic P123 strongly influences the morphology and the growth preference of ZnO materials prepared by the hydrothermal route. In particular, in the presence of Pluronic P123 hierarchical ZnO microflowers whose surface is dominated by their (002) polar planes were formed.

2.3.2. The influence of the ZnO precursor

Since the most promising ZnO material was obtained in the presence of Pluronic P123 (Zn_{Ac}P10T90), we focused on the optimization of its preparation. Accordingly, a series of ZnO samples were prepared following the same procedure as for the Zn_{Ac}P10T90 sample by only changing one parameter while keeping the rest to be constant. The following parameters were studied: ZnO precursor, Pluronic P123 concentration and hydrothermal synthesis temperature (Table 2.1). The influence of

these parameters on the specific surface area, morphology, structure and growth habit (polarity) of ZnO products is discussed in next sections.

Table - 2.1 - Experimental parameters studied for the preparation of ZnO samples (Zn_xPyTz: x Zn-precursor; Py Pluronic P123 amount; Tz synthesis temperature).

Parameter studied	Range	Sample name
ZnO - precursor	Zn acetate	$Zn_{Ac}P10T90$
	Zn nitrate	$Zn_{N}P10T90$
P123 concentration (n_{P123}/n_{Ac}) molar ratio%	0	$Zn_{Ac}P0T90$
	3	$Zn_{Ac}P3T90$
	7	$Zn_{Ac}P7T90$
	10	$Zn_{Ac}P10T90$
	20	$Zn_{Ac}P20T90$
Synthesis temperature (°C)	70	$Zn_{Ac}P10T70$
	90	$Zn_{Ac}P10T90$
	110	$Zn_{Ac}P10T110$

The influence of the Zn-precursor on the morphology of the prepared ZnOs is presented in Figure 2.5.

The use of Zn-nitrate ($Zn_NP10T90$) resulted in the formation of sea urchin-like ZnO structures (Figure 2.5-A) made of very thin ZnO nanowires (*ca.* 25 nm thick; Figure 2.5-B). As previously indicated, the sample synthesized from Zn-acetate ($Zn_{Ac}P10T90$) presents a lamellar flower-like architecture (Figure 2.5-C and D), made up of assembled porous ZnO nanosheets (*ca.* 23 nm thick). Considering the size of these ZnO materials, it is found that the Zn-nitrate precursor leads to smaller ZnO structures (mean size 12 µm; Figure 2.5-A) in comparison with its Zn-acetate counterpart (mean size 20 µm; Figure 2.5-B).

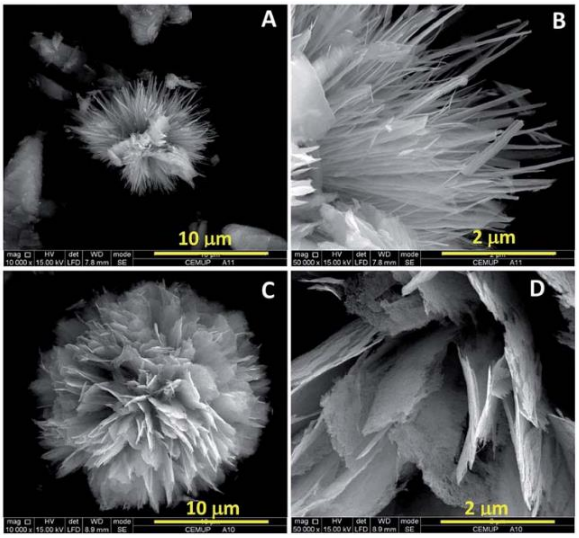

Figure 2.5 - SEM images of ZnO samples prepared with different types of metal salts: zinc nitrate, Zn_NP10T90, (A and B) and zinc acetate, Zn_{Ac}P10T90, (C and D).

Both samples have a quite similar specific surface area (80 and 76 $m^2 \cdot g^{-1}$ for samples Zn_{Ac}P10T90 and Zn_NP10T90 samples, respectively), and also show the same würtzite structure although the relative intensities of the polar (002) and nonpolar (100) XRD planes is very different. The latter suggests that the growth habit of ZnO crystals is different in both samples. As already mentioned, the Zn_{Ac}P10T90 sample has a higher polarity ($I_{(002)}/I_{(100)}$= 1.10) than the reference würtzite. In contrast, the Zn_NP10T90 sample (prepared from Zn nitrate) shows lower polarity ($I_{(002)}/I_{(100)}$= 0.60). This indicates that the Zn salt precursor influences the growth habit of the resulting ZnO products.This might be related to the different morphologies of both ZnO products as reported in [26-28]. In the case of Zn_{Ac}P10T90 sample the flowers are composed of plates (Figure 2.5-D); these kind of structures are likely originated from lateral growth along the nonpolar facets of ZnO then explaining their increased polarity in a similar fashion as described in [20, 22, 29, 30]. On the other hand, the urchin structures formed in Zn_NP10T90 are made up of needles (Figure 2.5-B). According to the literature [31-33] the usual growth along *c*-axis is expected to occur in such case, explaining the lower polarity of the sample Zn_NP10T90 sample.

2.3.3. *The influence and role of the Pluronic P123 concentration*

The SEM images of the samples prepared with increasing Pluronic P123 concentration (Table 2.1) are depicted in Figure 2.6. The sample prepared with the lowest Pluronic P123 amount (Zn_{Ac}P3T90; n_{P123}/n_{Ac} molar ratio = 0.03) consists of ZnO particles of irregular shapes (Figure 2.6-A). The morphology of Zn_{Ac}P7T90 and Zn_{Ac}P10T90 samples (n_{P123}/n_{Ac} molar ratio = 0.07 and 0.10, respectively; Table 2.1) is similar. In fact, both samples have a flower-like morphology (mean size of 20 µm) assembled from ZnO plates (Figure 2.6-B and C), although sample Zn_{Ac}P10T90 has a higher number of voids between the sheets (compare inset in Figure 2.6-B and C). The structure became more compact as the P123 concentration increases (Figure 2.6-D), resulting in the formation of non-uniform agglomerated particles, where no ZnO nanoplates are apparent (inset Figure 2.6-D) as for the Zn_{Ac}P20T90 sample (n_{P123}/n_{ZnAc} molar ratio= 0.20).

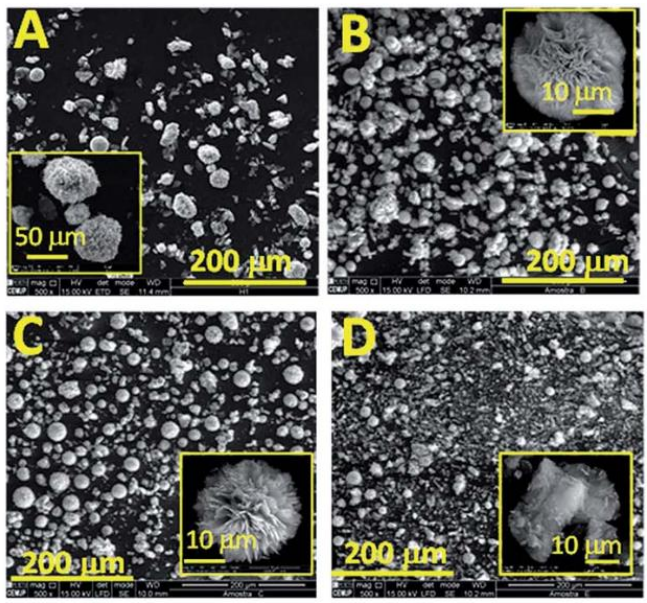

Figure 2.6 - SEM images of the ZnO products prepared with different n_{P123}/n_{Ac} molar ratios: A) 0.03 (ZnAcP3T90), B) 0.07 (ZnAcP7T90), C) 0.10 (Zn_{Ac}P10T90) and D) 0.20 (Zn_{Ac}P20T90).

The evolution of the specific surface area with the Pluronic P123 content (Figure 2.7) also points to the same conclusions. As shown in Figure 2.7 the surface area steadily increases with the Pluronic P123 content until an optimum value (0.10 molar ratio, Zn_{Ac}P10T90, S_{BET} = 80 $m^2 \cdot g^{-1}$). Further increase causes to significantly decrease the surface area, in good agreement with the agglomeration of this sample as suggested by SEM.

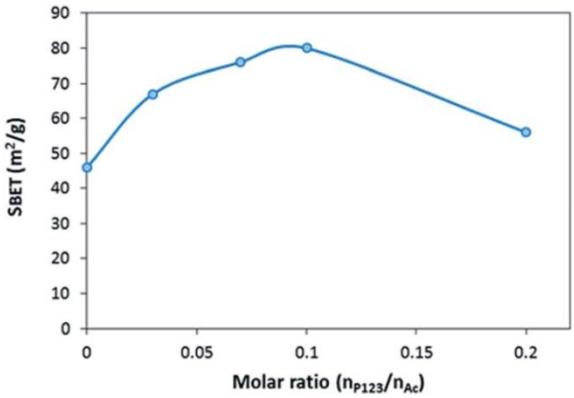

Figure 2.7 - Evolution of the specific surface area of ZnO samples as a function of the Pluronic P123 content (Zn_{Ac}PyT90 series: Zn-acetate and hydrothermal temperature 90 ˚C). Lines were added for readability.

In all cases the final ZnO solids displayed XRD patterns characteristic for würtzite (Figure 2.8). As observed in Figure 2.8, significant changes in the relative intensities of the polar (002) and nonpolar (100) planes are observed with varying the Pluronic P123 content.

The sample with the lowest Pluronic P123 content (Zn_{Ac}P3T90) has essentially the same polarity (Figure 2.8) as the würtzite reference ($I_{(002)}/I_{(100)}$ = 0.76 and 0.73 for Zn_{Ac}P3T90 and würtzite, respectively), indicating that this sample follows the growth habit of ZnO crystals along *c*-axis.

As the P123 molar ratio was increased (Zn_{Ac}P7T90 and Zn_{Ac}P10T90 samples) substantial growth of the polar (002) plane is found (Figure 2.8). Both samples have higher polarity than the würtzite ($I_{(002)}$ /$I_{(100)}$ = 0.94 and 1.10 for Zn_{Ac}P7T90 and

Zn_{Ac}P10T90, respectively). In contrast, further increase of P123 content, (Zn_{Ac}P20T90) resulted in the opposite effect. Therefore, for Zn_{Ac}P20T90 sample the nonpolar (100) peak has a higher intensity than that of the würtzite, indicating a lower polarity, namely, a lower ratio of exposed polar facets.

Additionally, the microspheres are almost absent from the Zn_{Ac}P20T90 sample, which is mainly constituted by nanoflakes without a clear and well-defined morphology. Peng Bai *et al.*, had a similar result when the concentration of Pluronic was increased to a extreme value. This phenomena was attributed to an excess of surfactant in solution leading to high viscosities that can reduce the mobility of nanoparticles and hinder the self-assembly process [34].

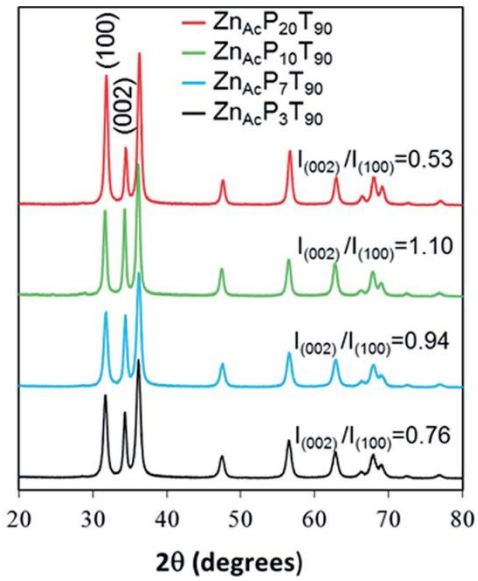

Figure 2.8 - XRD pattern and $I_{(002)}/ I_{(100)}$ ratio of the ZnO samples synthesized from Zn-acetate, at 90 ˚C and with different Pluronic P123 content.

The surface of this series of samples was characterized by XPS – Figure 2.9. All samples show Zn and O as main elements (being the atomic ratio about 1, as expected for ZnO) along with trace amount of adventitious carbon contaminant. For all the samples, the Zn $2p_{3/2}$ XPS spectrum is centered at 1021.3 ± 0.2 eV with a

symmetrical peak type, indicating that it exists only in the oxidized state Zn^{2+} [35]. On the other hand, the O 1s photoelectron peak is asymmetrical and presents a visible shoulder on the high binding energy side (Figure 2.9). The O 1s XPS peak can be fitted using two Gaussian components centered at 530.1 (low binding energy oxygen, reffered as O_{LBE}) eV and 531.5 eV (high binding energy oxygen, reffered as O_{HBE}), respectively. According to the literature the first component 530.1 eV (O_{LBE}) is attributed to O^{2-} ions on würtzite structure of hexagonal Zn^{2+} ion array, surrounded by Zn atoms with their full complement of nearest-neighbour O^{2-} ions. The O_{HBE} is associated with O^{2-} in oxygen deficient regions within the matrix of ZnO.

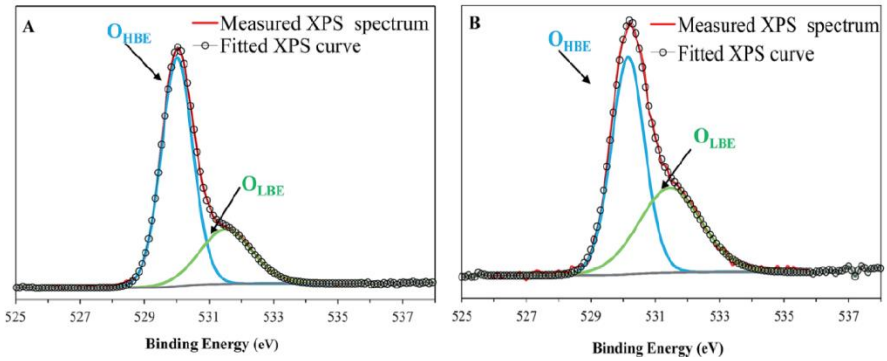

Figure 2.9 – O 1s XPS spectrum for (A) Zn_{Ac}P0T90 and (B) ZnAcP10T90 samples prepared in the absence and presence of Pluronic P123, respectively.

As clearly visible in Figure 2.9 and Table 2.2, the relative ratio of both components is different for the various samples. In fact, the relative ratio of the O_{HBE} O 1s component appears to increase with P123 amount between 0.03 and 0.10 molar ratio, indicating that increasing the amount of P123 within this ratio contributes to enhance the number of oxygen defects, in good agreement with the above conclusions. The surface composition of the ZnO samples, based on XPS spectra, revealed that the concentration of oxygen vacancies tend to increase with the P123 concentration.

Table 2.2 - XPS relative composition of the O1s peak for the series of ZnO samples prepared with increasing Pluronic P123 concentration.

Sample	P123 concentration (n_{P123}/n_{ZnAc}) molar ratio	O_{LBE}* (at. %)	O_{HBE}** (at. %)
Zn_{Ac}P0T90	0.00	45	15
Zn_{Ac}P7T90	0.07	39	21
Zn_{Ac}P14T90	0.14	37	23
Zn_{Ac}P10T90	0.10	33	27

Atomic percentage of low binding energy (*O_{LBE}) and high binding energy (**O_{HBE}) O 1s component for the various ZnO samples prepared with different amount of Pluronic P123.

It is clear that the P123 content strongly influences the morphology, the specific surface area, the surface composition and the growth habit of ZnO samples. Our results evidence that there is an optimum range that allows preparing homogeneous hierarchical ZnO structures with enhanced specific surface area and polarity. All these properties make this kind of ZnO materials good candidates for a wide range of applications such as: catalysis [8-11], emitting diodes [4], piezoelectric transducers [5], lasers [6], hydrogen sensors [5], biosensors [6] and inorganic antimicrobial agents [7].

2.3.4. The role of Pluronic P123 on the morphology of ZnO

Due to their amphiphilic structure, the triblock copolymer Pluronics, forms micelles in aqueous solutions to lower the free energy in a similar fashion as the non-ionic surfactants. As for the former surfactants, the concentration and temperature of the solution is crucial for the formation of micelles. On the other hand, micellization of Pluronic copolymers in water is very sensitive to the presence of additives. The interaction of urea (a salting-in compound) with various Pluronics copolymers is detailed in [36]. According to these authors, in the presence of urea the CMT (critical micelles temperature) of Pluronic copolymers is shifted to higher values [36]. These micelles consist of a hydrophobic polypropylene oxide core surrounded by hydrophilic polyethylene oxide chains that form a shell around the core. Therefore, polar urea molecules and Zn aquo-complex would interact with the terminal hydroxyl

groups of the hydrophilic shell of P123 micelles. As the temperature increases, the urea hydrolysis begins leading to $NH4^+$ and HCO_3^- ions that react with Zn^{2+} to form HZC nuclei. Because of this particular interaction, the precipitation and subsequent growth of HZC particles is expected to occur in these preferential sites near the micelles-urea interface, resulting in the oriented growth of ZnO crystals in the form well dispersed of micro-flowers. In the absence of Pluronic P123, the homogeneous nucleation of ZHC particles occurs and large spherical structures are formed during the growth process (Figure 2.3-A and 2.15-E). The copolopymer is then removed during washing and the obtained ZHC solid is then heated forming either well-dispersed ZnO microflowers (Zn_{Ac}P10T90, with P123) or larger crystals of ZnO in the absence of P123 (Zn_{Ac}P0T90)

Apart from the morphological differences, the polarity of ZnO products, ($I_{(002)}/I_{(100)}$), is also affected by the use of Pluronic P123. In fact, in the absence of Pluronic P123, the growth of ZnO crystals occurs mainly along the *c*-axis leading to the preferential exposure of nonpolar facets. On the contrary, in the Pluronic-assisted hydrothermal reaction, ZnO crystals are formed according to an oriented-growth process that preferentially occurs perpendicularly to the *c*-axis direction. As a result, more polar structures are obtained.

The growth habit of ZnO solids under hydrothermal conditions is well-documented in the literature [33, 37, 38]. The growth velocities under hydrothermal conditions along the different directions are known to follow the pattern V(0001) > V(1011) > V(1010) [39]. The relative growth rate of these crystal faces will determine the final shape and aspect ratio of the ZnO structures. In the absence of any external driving force, growth along the polar facets (*c*-axis direction) is favoured due to their high surface energy. As such, the preferred morphology of ZnO is hexagonal with crystals elongated along the *c*-axis, as for the sample prepared without Pluronic P123 herein. However, the crystal growth habit can be modified by selective adsorption of additives on the polar planes [19].

Under our experimental conditions, the preferential interaction of P123 micelles with the surface of metastable polar facets of ZnO lowers their surface energy, slowing down their growth. Because of this, the lateral growth of ZnO crystals

(perpendicular to the *c*-axis) is stabilized leading to the formation of ZnO micro-flowers whose surface is dominated by polar facets. Similarly, in the absence of Pluronic P123 the ZHC particles formed during the nucleation step grow and evolve into large cluster in order to minimize the surface energy, as a consequence the growth occurs preferentially at expense of the polar planes (along the *c*-axis), which are less stable [39], leading to the typical ZnO solids with preferential exposure of nonpolar facets.

2.3.5. *The influence of the hydrothermal reaction temperature*

The morphological evolution of the ZnO samples prepared at different reaction temperatures is illustrated in Figure 2.10. The sample prepared at 70 °C (Zn_{Ac}P10T70, Figure 2.10-A) exhibits an irregular shape (quasi-flower-like structure) that resembles to an early stage of the flower-like morphology obtained at 90 °C (Zn_{Ac}P10T90); the latter is composed of assemblies of ZnO sheets (Figure 2.10-B). Further increase of reaction temperature up to 110 °C (Zn_{Ac}P10T110) resulted in the agglomeration of ZnO particles that appear assembled in the form of large cauliflower-like structures (Figure 2.10-C). On the other hand, it was found that the end pH of the hydrothermal reaction medium also increases with synthesis temperature; it increases from its initial value of 5.0 to 7.0, 8.4 and 9.1, when the reaction temperature was 70 °C, 90 °C and 110 °C, respectively. Hence, it is observed that the morphology of ZnO samples markedly changes with reaction temperature, in particular, the degree of compactness increases while increasing the temperature. Clearly the morphology strongly depends on the reaction temperature (and pH), which in turn controls the rate of urea decomposition.

The morphological changes observed in Figure 2.10 are likely due to the temperature dependence of urea decomposition. Seeing that the urea content was identical in the three experiments, the lower pH values encountered at lower reaction temperature suggest slow urea decomposition rates and *vice versa*. According to the literature, the urea decomposition is a temperature-dependent reaction that is favored at relatively high temperatures, typically above 90 °C [40, 41]. At 70 °C (lower pH)

the urea hydrolysis is slow, so that the concentration of ammonium and bicarbonate ions is low and consequently less ZnO particles are formed leading to the quasi-flower structures of Figure 2.10-A. However, at 90 °C the urea decomposition is faster and more ZnO particles are formed, giving rise to the micro-flowers in Figure 2.10-B. Finally, at 110 °C the urea hydrolysis is likely too fast which might cause the agglomeration and formation of the large cauliflower-like architectures shown in Figure 2.10-C.

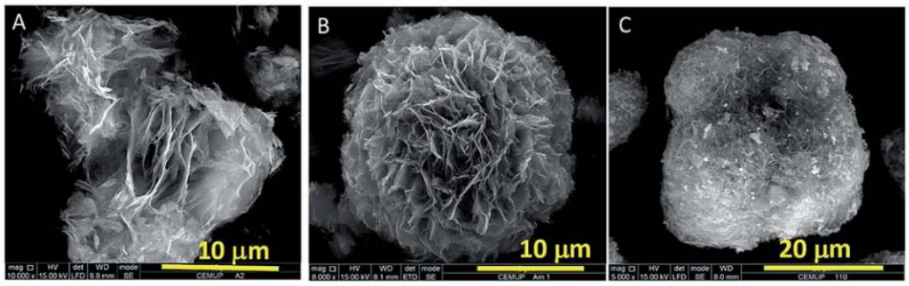

Figure 2.10 - SEM images of the ZnO samples synthesized at different hydrothermal temperatures: A) 70 °C (Zn_{Ac}P10T70); B) 90 °C (Zn_{Ac}P10T90) and C) 110 °C (Zn_{Ac}P10T110).

The specific surface area of this group of samples increases with hydrothermal temperature in the 70 °C - 90 °C interval (S_{BET} = 64 and 80 $m^2 \cdot g^{-1}$, for Zn_{Ac}P10T70 and Zn_{Ac}P10T90). Further increase of reaction temperature causes a significant decrease of the specific surface area (Zn_{Ac}P10T110 S_{BET} = 50 $m^2 \cdot g^{-1}$). The evolution of the S_{BET} with temperature is in good agreement with the formation of larger ZnO agglomerates at higher reaction temperature, as evidenced by SEM.

It was found that the peak intensity of XRD for the analyzed samples tends to increase with the temperature – Figure 2.11. Since the sample weight used in XRD analysis is nearly the same, this is attributed to a higher degree of crystallinity of the resulting ZnOs. Regarding the polarity of this series of samples, it is observed that sample Zn_{Ac}P10T70 shows nearly the same value ($I_{(002)}/I_{(100)}$= 0.75) as the würtzite ($I_{(002)}/I_{(100)}$= 0.73). This suggests that both samples follow the typical growth habit of würtzite with preferential orientation along *c*-axis, resulting in ZnO materials whose

surface is dominated by non-polar planes. The sample Zn_{Ac}P10T90 exhibits the highest polarity ($I_{(002)}/I_{(100)}$= 1.10), which represents a higher ratio of exposed polar facets, as already indicated. The Zn_{Ac}P10T110 sample has the lowest polarity among this series of samples, which is even lower than the würtzite. This indicates that this sample has a higher ratio of non-polar planes. The variation in polarity observed here is probably related to the different morphology of the various samples. By comparison, the ZnO particles obtained at 90 °C show the optimal morphology, S_{BET} and also polarity.

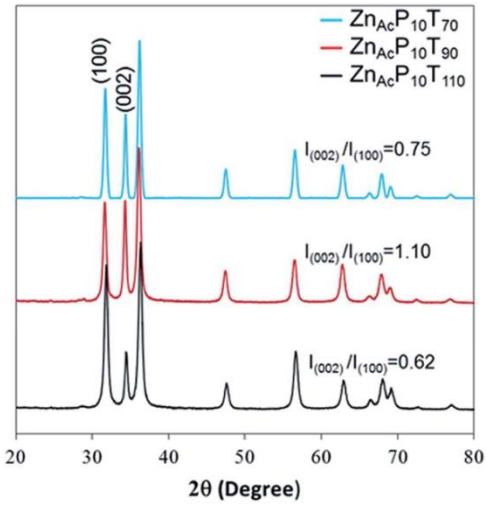

Figure 2.11 - XRD pattern and $I_{(002)}/I_{(100)}$ ratio of the ZnO samples prepared at different hydrothermal temperatures.

2.3.6. Evaluation of the photocatalytic activity

The photocatalytic activity of a semiconductor such as ZnO dependents on the optical properties, specific surface area, particle size and morphology of the particles [13, 42-44]. In particular a high polarity (higher number of defects) and high specific surface area are expected to increase the photocatalytic activity of ZnO materials [13, 45].

The results presented in preceding sections evidence that both the polarity and specific surface area of ZnO materials prepared by the hydrothermal route depend on the synthesis conditions. To discriminate if the photoactivity of the prepared ZnO samples is influenced by the S_{BET} and/or the polarity, samples with similar S_{BET} but greatly differing in polarity (Zn_{Ac}P10T90 and Zn_{N}P10T90) and samples with similar polarity but with very different specific surface areas (Zn_{Ac}P10T90 and Zn_{Ac}P7T90) were selected. The idea is to use the photocatalytic test as an indirect confirmation of polarity trends. Accordingly, the degradation of methylene blue (MB) was assessed using three ZnO samples already mentioned: Zn_{Ac}P10T90, Zn_{N}P10T90 and Zn_{Ac}P7T90. Figure 2.12 shows the results obtained. Sample Zn_{N}P10T90 (lowest polarity) exhibited a lower degradation rate, taking approximately 200 min to achieve total photocatalytic degradation. On the other hand, samples with higher polarity (Zn_{Ac}P10T90 and Zn_{Ac}P7T90) exhibited a prominent photocatalytic activity degrading the MB in 100-120 min, despite having different S_{BET} areas. These results show that the photoactivity of the prepared ZnO materials, under the present operation conditions, dependes on the polarity rather then the S_{BET} surface area. On the other hand our "more polar" ZnO materials (Zn_{Ac}P10T90 and Zn_{Ac}P7T90) show comparable [46] or better photocatalytic performance [47, 48] as compared to other ZnOs tested under similar operating conditions.

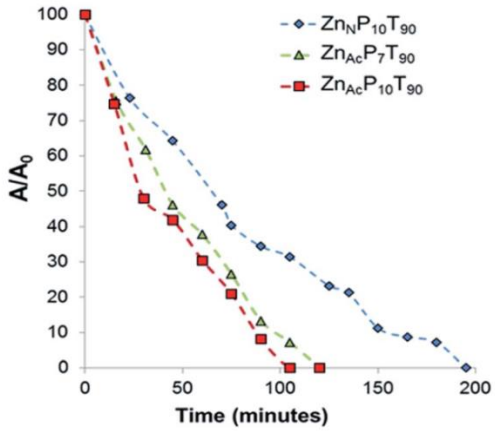

Figure 2.12 - Photocatalytic degradation of MB over: Zn_{Ac}P10T90 (S_{BET}= 80 $m^2 \cdot g^{-1}$; $I_{(002)}/I_{(100)}$ = 1.10), Zn_{N}P10T90 (S_{BET}=76 $m^2 \cdot g^{-1}$;$I_{(002)}/I_{(100)}$= 0.62) and Zn_{Ac}P7T90 (S_{BET}=53 $m^2 \cdot g^{-1}$; $I_{(002)}/I_{(100)}$= 0.92). Lines are added for readability.

2.3.7. *Role of Pluronic P123 on the ZnO formation mechanism*

To gain some understanding about the role of the Pluronic P123 on the formation, growth process and morphology of HZC precursor, two samples, with and without P123, were prepared following the same experimental protocol as that used for the synthesis of samples Zn_{Ac}P10T90 and Zn_{Ac}P0T90. During both syntheses a small amount of sample was taken out at different intervals and characterized by SEM-EDX. It should be noted that no product was collected if the hydrothermal time was inferior to 30 minutes (in the presence of P123) and 215 minutes (without P123). The evolution of the pH and temperature of hydrothermal solution during sampling was also recorded. The results are displayed in Figure 2.13.

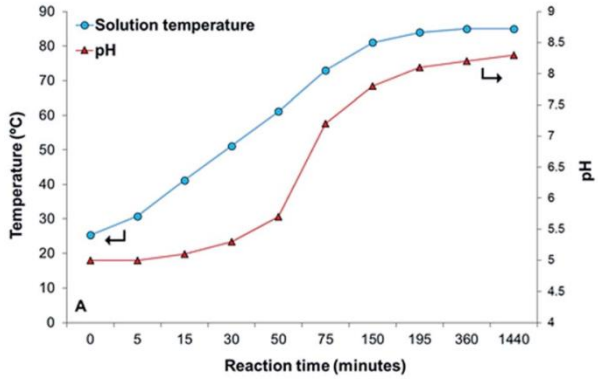

Figure 2.13 - pH and temperature of the hydrothermal solution as a function of the reaction time for Zn_{Ac}P10T90 sample. Lines are for readability.

The temperature of the solution steadily increased during the first 3 h of reaction and stabilizing at *ca.* 85 °C (Figure 2.13) until the end of the synthesis (24 h). The variation of pH with reaction time follows a similar trend (Figure 2.13); it slightly increases with temperature during the first 50 minutes of reaction, then it increases sharply between 60 °C to 82 °C, and finally reaches a constant value of around 8.4. The pH history is essentially related to the homogeneous urea decomposition.

Consequently, the formation and growth of HZC precipitate particles should be governed by the gradual urea hydrolysis, as nicely illustrated in Figure 2.13.

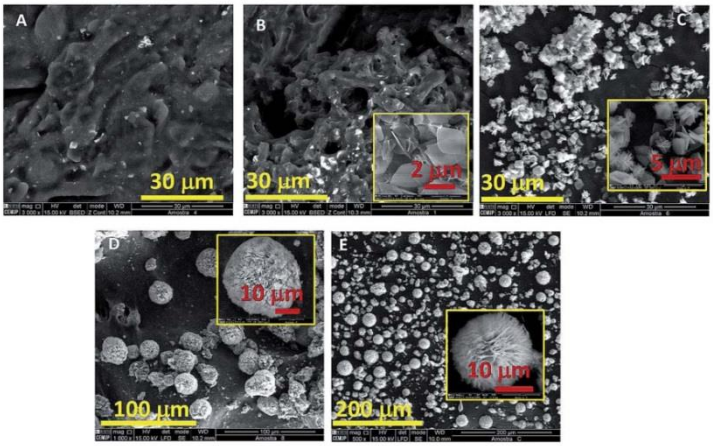

Figure 2.14 – SEM images showing the morphology evolution during the hydrothermal synthesis of the HZC in the presence of Pluronic P123 (same synthesis conditions as for $Zn_{Ac}P10T90$ sample: Zn-acetate, 0.10 (n_{P123}/n_{Ac}) molar ratio and 90 °C), after: (A) 30 min, (B) 75 min, (C) 150 min, (D) 195 min and (E) 24 h.

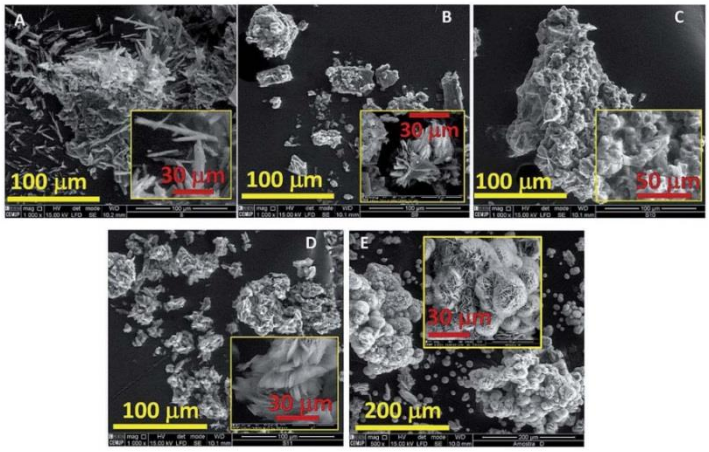

Figure 2.15 - SEM images showing the morphology evolution during the hydrothermal synthesis of the HZC in the absence of Pluronic P123 (same synthesis conditions of $Zn_{Ac}P0T90$ sample: Zn-acetate, no P123 and 90 °C), after: (A) 215 min, (B) 230 min, (C) 250 min, (D) 270 min and (E) 24 h.

The different contrast in the low voltage SEM images in Figure 2.14-A and B suggests some degree of heterogeneity in these samples. Accordingly, the EDX images of the materials show that in the bright areas Zn is the major element. The dark shades have a different composition, where N and C appear as the main components along with O and traces of Zn; urea should be the main component of these regions.

As mentioned, some Zn-rich particles (bright areas in Figure 2.14-A) are already formed during the first 30 minutes of the hydrothermal reaction. At this stage and according to Figure 2.13, the urea hydrolysis is likely very slow due to the low temperature of hydrothermal solution, so the equilibrium of urea hydrolysis is shifted towards the left side, in good agreement with EDX results that indicate high N contents. This is also consistent with the low pH (Figure 2.13), which evidences that the equilibrium of urea hydrolysis (Equation 2.2) lies to the left side; there is a much greater concentration of urea than bicarbonate and ammonium ions, and no significant H^+ consumption take place, so pH remains essentially unchanged at 5. This also agrees with reported works on urea hydrolysis [40]. After 75 minutes of reaction, HZC species in the form of thin sheets are formed, as shown in the inset of Figure 2.14-B. As the reaction proceeds, the number of HZC particles increases (Figure 2.14-C), and the sheets appear now assembled in larger structures (inset in Figure 2.14-C). The spherical particles observed after 3 h of reaction (Figure 2.14-D) strongly resemble the micro-flowers observed after 24 h of hydrothermal reaction (inset in Figure 2.3-B).

Similar experiments were conducted in the absence of Pluronic P123. The obtained SEM images are shown in Figure 2.15. In this case the precipitated particles are formed at much higher reaction times (215 min vs. 30 min in the synthesis without P123). As apparent in this figure, the morphology evolution of the various materials with reaction time follows a similar tendency to that found in the presence of P123, although the solids show quite different morphology. In general, larger clusters are formed in the absence of Pluronic P123, as observed in Figures 2.3-A and 2.15-E (final product). Interestingly, the SEM images of the resulting HZC material in Figure 2.14-E (after 24 h of reaction), shows that spherical clusters are

formed regardless of Pluronic P123, but they appear better dispersed and have a more uniform aggregate size when P123 is used. Thus, it is clear that under identical synthesis conditions, the use of Pluronic P123 enhances the dispersion of the formed HZC precipitates with the spherical morphology being characteristic of this kind of zinc basic hydroxy carbonates (ZHC).

2.3.8. ZnO Formation Mechanism

In order to understand the role played by the Pluronic P123 on the formation process of ZnO in our experimental conditions, the aqueous chemistry of zinc and the urea hydrolysis will be analyzed henceforth.

Upon dissolution of a zinc salt (Zn-Acetate herein) in water, Zn^{2+} cations become octahedrally coordinated forming $[Zn(OH_2)_6]^{2+}$. The hexaqua zinc species are quite stable in very acidic medium but undergo hydrolysis at higher pHs. According to the literature [49, 50] around pH 5 cations $[Zn(OH_2)_5(OH)]^+$ are the predominant species in solution. Thus, initial conditions of pH and temperature (at instant t = 0, in Fig. 2.13), urea and Pluronic P123 are stable in solution, since the solution temperature is very low (room temperature) for the urea decomposition and Pluronic micellization, and zinc is mostly as $[Zn(OH_2)_5(OH)]^+$. The mixture is then heated and the temperature of the solution gradually increases and around 50 °C micellization of Pluronic P123 is expected to occur [36]. The Pluronic micelles would interact with the polar species existing in solution, creating in this way the active sites for further nucleation and growth. At this point, the temperature is still too low for urea hydrolysis, and since the pH remains unchanged around 5, $[Zn(OH_2)_5(OH)]^+$ species are stable in solution. However, the solution temperature continues increasing and around 70 °C fast urea decomposition occurs. The optimum temperature for the urea hydrolysis is at about 85 °C [40], which is accompanied by a sharp increase of pH (herein, after 75 minutes, Figure 2.13). The decomposition of urea in aqueous solutions takes place in two stages [40]. The first one involves the formation of ammonium cyanate, which is followed by the irreversible hydrolysis of cyanate ions. Thus, the hydrolysis of urea can be written as follows:

$$CO(NH_2)_2 + 3H_2O \leftrightarrow HCO_3^- + 2NH_4^+ + OH^- \quad (2.2)$$

Obviously, the extent of the reaction defines the release of bicarbonate ions and OH^-, resulting in a gradual increase of pH, as observed in Fig. 2.13. According to [50], $[Zn(OH_2)_5(OH)]^+$ species are complexed by HCO_3^- anions giving rise to $[Zn(OH)(HCO_3)(OH_2)_3]$. On the other hand, as pH raises the former species become unstable and undergo ligand exchange between the OH^- and HCO_3^- leading to neutral $[Zn(OH_2)_4(OH)_2]$ species.

Then, in the experimental conditions of the present study, the HZC nuclei are likely generated from condensation reactions between both $[Zn(OH_2)_4(OH)_2]$ and $[Zn(OH)(HCO_3)(OH_2)_3]$ according to equation 2.3 [50]:

$$3\left[Zn(OH_2)_4(OH)_2\right] + 2\left[Zn(OH)(HCO_3)(OH_2)_3\right] \rightarrow Zn_5(OH)_6(CO_3)_2 + 20H_2O \quad (2.3)$$

The formed nuclei then grew up to produce primary ZHC nanoparticles, which aggregated to form sheets (Figure 2.14-B). Subsequent growth leads to larger HZC structures (Figure 2.14-C and D), which are thermodynamically more stable, and finally to the hierarchical micro-flowers in Figure 2.14-E. In the synthesis carried out with Pluronic P123, since the nucleation process occurs in preferential sites, highly dispersed ZHC microflowers are generated from an oriented growth mechanism. However, in the absence of Pluronic, homogeneous nucleation takes place randomly, which leads to the formation of larger HZC particles during the growth step (Figure 2.14) that undergo agglomeration giving rise to the large structures displayed in Figure 2.14-E. Finally, the HZC solid will decompose into ZnO upon heating according to equation 2.1, releasing CO_2 and H_2O (as evidenced by TPD and TG) to generate the porous ZnO microstructures illustrated in Figure 2.4-E. Moreover the ZnO solid synthesized in the presence of P123, Zn_{Ac}P10T90 sample, after calcination maintains the original flower-like architectures as well as the high dispersion of the HZC precursor (Figure 2.4-E). As a result of the low dispersion, the sample obtained without P123 (Zn_{Ac}P0T90), leads to a more compact and shapeless ZnO material after calcination, as illustrated in Figure 2.4-C.

Comparing Figures 2.14 and 2.15 it can be seen that the nucleation-growth process depends on the presence of P123. In this former case, P123 acts as a template, providing the sites for nucleation and growth, contributing to the formation of highly dispersed ZHC particles during growth. As a result homogeneous and dispersed ZnO solids in the form of microflowers are obtained upon calcination. Our results suggest that Pluronic P123 acts as growth director and dispersing agent.

2.4. Conclusions

Pluronic P123 block copolymer strongly influenced the morphology, polarity and specific surface area of the ZnO materials prepared by the urea-assisted hydrothermal method. In the presence of Pluronic P123, hierarchical ZnO microflowers whose surface is dominated by (002) polar planes were formed. Contrarily to this, large clusters agglomerates are formed in its absence and surface is dominated by (100) non-polar planes. Moreover the use of Pluronic P123 leads to ZnO materials with enhanced S_{BET}. The morphology and polarity is also affected by changing the metal salt from zinc acetate to zinc nitrate precursor. In this latter case, an urchin-like structure is obtained and proportion of polar planes is only of 0.60 (Zn_NP10T90). The synthesis temperature seems to affect the decomposition rate of urea, being obtained at 70 °C and 110 °C quasi-flower and large cauliflower-like architectures, respectively. The materials with higher polarity showed higher photocatalytic activity for the decomposition of methylene blue, evidencing that even with similar surfaces areas the polar surfaces are more reactive, mainly due to the higher number of defects such as oxygen vacancies. The role of Pluronic 123 in the initial steps of the hydrothermal synthesis was clearly visible through backscattering images on SEM, acting as a template and providing the sites for nucleation and growth. This simple and easily scalable method allows the synthesis of ZnO with a highly faceted morphology, combined with high surface area and polarity, making these materials very promising for several applications, such as catalysis.

2.5. Acknowledgments

The research leading to these results has received funding from the European Union's Seventh Framework Programme (FP/2007- 2013) for the Fuel Cells and Hydrogen Joint Technology Initiative under grant agreement nº. [303476] 10. The work of Hugo Silva was supported by FCT, grant SFRH/BD/45890/2008. The authors also acknowledge financing from FCT through the project PTDC/EQU-EQU-EQU/104217/2008. Ms. Joana Angelo is acknowledged for her help in photocatalytic tests. CEMUP is also thanked.

2.6. References

[1] S. Du, Y. Tian, H. Liu, J. Liu, Y. Chen, Calcination Effects on the Properties of Gallium-Doped Zinc Oxide Powders, Journal of the American Ceramic Society, 89 (2006) 2440-2443.

[2] D. Polsongkram, P. Chamninok, S. Pukird, L. Chow, O. Lupan, G. Chai, H. Khallaf, S. Park, A. Schulte, Effect of synthesis conditions on the growth of ZnO nanorods via hydrothermal method, Physica B: Condensed Matter, 403 (2008) 3713-3717.

[3] O. Lupan, L. Chow, G. Chai, B. Roldan, A. Naitabdi, A. Schulte, H. Heinrich, Nanofabrication and characterization of ZnO nanorod arrays and branched microrods by aqueous solution route and rapid thermal processing, Materials Science and Engineering: B, 145 (2007) 57-66.

[4] J. Bao, M.A. Zimmler, F. Capasso, X. Wang, Z.F. Ren, Broadband ZnO Single-Nanowire Light-Emitting Diode, Nano Letters, 6 (2006) 1719-1722.

[5] T. Aeugle, H. Bialas, K. Heneka, W. Pleyer, Large area piezoelectric ZnO film transducers produced by r.f. diode sputtering, Thin Solid Films, 201 (1991) 293-304.

[6] M.H. Huang, S. Mao, H. Feick, H. Yan, Y. Wu, H. Kind, E. Weber, R. Russo, P. Yang, Room-Temperature Ultraviolet Nanowire Nanolasers, Science, 292 (2001) 1897-1899.

[7] L. Shen, N. Bao, K. Yanagisawa, K. Domen, C.A. Grimes, A. Gupta, Organic Molecule-Assisted Hydrothermal Self-Assembly of Size-Controlled Tubular ZnO Nanostructures, The Journal of Physical Chemistry C, 111 (2007) 7280-7287.

[8] B. Meyer, D. Marx, Density-functional study of Cu atoms, monolayers, films, and coadsorbateson polar ZnO surfaces, Physical Review B, 69 (2004) 235420.

[9] F. Ostendorf, S. Torbrügge, M. Reichling, Atomic scale evidence for faceting stabilization of a polar oxide surface, Physical Review B, 77 (2008) 041405.

[10] M.S. Spencer, The role of zinc oxide in Cu/ZnO catalysts for methanol synthesis and the water–gas shift reaction, Topics in Catalysis, 8 (1999) 259-266.

[11] H. Wilmer, M. Kurtz, K.V. Klementiev, O.P. Tkachenko, W. Grunert, O. Hinrichsen, A. Birkner, S. Rabe, K. Merz, M. Driess, C. Woll, M. Muhler, Methanol synthesis over ZnO: A structure-sensitive reaction?, Physical Chemistry Chemical Physics, 5 (2003) 4736-4742.

[12] P.P.C. Udani, P.V.D.S. Gunawardana, H.C. Lee, D.H. Kim, Steam reforming and oxidative steam reforming of methanol over CuO–CeO_2 catalysts, Int. J. Hydrogen Energy, 34 (2009) 7648-7655.

[13] R. Ullah, J. Dutta, Photocatalytic degradation of organic dyes with manganese-doped ZnO nanoparticles, Journal of Hazardous Materials, 156 (2008) 194-200.

[14] O. Dulub, M. Batzill, U. Diebold, Growth of Copper on Single Crystalline ZnO: Surface Study of a Model Catalyst, Topics in Catalysis, 36 (2005) 65-76.

[15] C. Wöll, The chemistry and physics of zinc oxide surfaces, Progress in Surface Science, 82 (2007) 55-120.

[16] K. Dai, G. Zhu, Z. Liu, Q. Liu, Z. Chen, L. Lu, Facile preparation and growth mechanism of zinc oxide nanopencils, Materials Letters, 67 (2012) 193-195.

[17] G.K. Smith, S. Lin, W. Lai, A. Datye, D. Xie, H. Guo, Initial steps in methanol steam reforming on PdZn and ZnO surfaces: Density functional theory studies, Surface Science, 605 (2011) 750-759.

[18] M.B. Boucher, S. Goergen, N. Yi, M. Flytzani-Stephanopoulos, 'Shape effects' in metal oxide supported nanoscale gold catalysts, Physical Chemistry Chemical Physics, 13 (2011) 2517-2527.

[19] G.R. Li, T. Hu, G.L. Pan, T.Y. Yan, X.P. Gao, H.Y. Zhu, Morphology−Function Relationship of ZnO: Polar Planes, Oxygen Vacancies, and Activity, The Journal of Physical Chemistry C, 112 (2008) 11859-11864.

[20] A. McLaren, T. Valdes-Solis, G. Li, S.C. Tsang, Shape and Size Effects of ZnO Nanocrystals on Photocatalytic Activity, Journal of the American Chemical Society, 131 (2009) 12540-12541.

[21] J. Chang, E.R. Waclawik, Facet-controlled self-assembly of ZnO nanocrystals by non-hydrolytic aminolysis and their photodegradation activities, CrystEngComm, 14 (2012) 4041-4048.

[22] P. Burton, E. Peterson, T. Boyle, A. Datye, Synthesis of High Surface Area ZnO(0001) Plates as Novel Oxide Supports for Heterogeneous Catalysts, Catalysis Letters, 139 (2010) 26-32.

[23] S. Baruah, J. Dutta, Hydrothermal growth of ZnO nanostructures, Science and technology of advanced materials, 10 (2009).

[24] R. Pérez-Hernández, A. Gutiérrez-Martinez, A. Mayoral, F.L. Deepak, M.E. Fernandéz-Garcia, G. Mondragón-Galicia, M. Jose-Yacaman, Hydrogen Production by Steam Reforming of Methanol over a Ag/ZnO One Dimensional Catalyst, Advanced Materials Research, 132 (2010) 205-219.

[25] Q. Tang, W. Zhou, J. Shen, W. Zhang, L. Kong, Y. Qian, A template-free aqueous route to ZnO nanorod arrays with high optical property, Chemical Communications, (2004) 712-713.

[26] M. Raula, M.H. Rashid, T.K. Paira, E. Dinda, T.K. Mandal, Ascorbate-Assisted Growth of Hierarchical ZnO Nanostructures: Sphere, Spindle, and Flower and Their Catalytic Properties, Langmuir, 26 (2010) 8769-8782.

[27] F. Fang, A.M.C. Ng, X.Y. Chen, A.B. Djurišić, W.K. Chan, Effect of zinc precursor on the morphology and optical properties of ZnO nanostructures prepared by electrodeposition, AIP Conference Proceedings, 1399 (2011) 251-252.

[28] M. Gusatti, G.S. Barroso, C.E.M. Campos, D.A.R. Souza, J.A. Rosário, R.B. Lima, C.C. Milioli, L.A. Silva, H.G. Riella, N.C. Kuhnen, Effect of different precursors in the chemical synthesis of ZnO nanocrystals, Materials Research, 14 (2011) 264-267.

[29] Z.L. Wang, Zinc oxide nanostructures: growth, properties and applications, Journal of Physics: Condensed Matter, 16 (2004) R829.

[30] Y.K. Hsu, Y.G. Lin, Y.C. Chen, Polarity-dependent photoelectrochemical activity in ZnO nanostructures for solar water splitting, Electrochemistry Communications, 13 (2011) 1383-1386.

[31] S. Xu, Z. Wang, One-dimensional ZnO nanostructures: Solution growth and functional properties, Nano Research, 4 (2011) 1013-1098.

[32] P. Yang, H. Yan, S. Mao, R. Russo, J. Johnson, R. Saykally, N. Morris, J. Pham, R. He, H.J. Choi, Controlled Growth of ZnO Nanowires and Their Optical Properties, Advanced Functional Materials, 12 (2002) 323-331.

[33] H. Zhang, D. Yang, X. Ma, Y. Ji, J. Xu, D. Que, Synthesis of flower-like ZnO nanostructures by an organic-free hydrothermal process, Nanotechnology, 15 (2004) 622.

[34] P. Bai, P. Wu, Z. Yan, J. Zhou, X.S. Zhao, Self-Assembly of Clewlike ZnO Superstructures in the Presence of Copolymer, The Journal of Physical Chemistry C, 111 (2007) 9729-9733.

[35] Y. Peng, D. Huo, L. Zhu, $Zn_{1-x}Co_xO$ film valence by photoelectron spectroscopy, Journal of Physics: Conference Series, 263 (2011) 012018.

[36] J.h. Ma, C. Guo, Y.l. Tang, L. Chen, P. Bahadur, H.z. Liu, Interaction of Urea with Pluronic Block Copolymers by 1H NMR Spectroscopy, The Journal of Physical Chemistry B, 111 (2007) 5155-5161.

[37] L. Shi, A.J.T. Naik, J.B.M. Goodall, C. Tighe, R. Gruar, R. Binions, I. Parkin, J. Darr, Highly Sensitive ZnO Nanorod- and Nanoprism-Based NO2 Gas Sensors: Size and Shape Control Using a Continuous Hydrothermal Pilot Plant, Langmuir, 29 (2013) 10603-10609.

[38] H. Zhang, D. Yang, Y. Ji, X. Ma, J. Xu, D. Que, Low Temperature Synthesis of Flowerlike ZnO Nanostructures by Cetyltrimethylammonium Bromide-Assisted Hydrothermal Process, The Journal of Physical Chemistry B, 108 (2004) 3955-3958.

[39] Z. Zhang, J. Mu, Hydrothermal synthesis of ZnO nanobundles controlled by PEO–PPO–PEO block copolymers, Journal of Colloid and Interface Science, 307 (2007) 79-82.

[40] G.A. Soler-Iltia, M. Jobbagy, R.J. Candal, A.E. Regazzoni, M.A. Blesa, Synthesis of metal oxide particles from aqueous media: The homogeneous alkalinization method, Journal of Dispersion Science and Technology, 19 (1998) 207-228.

[41] M.L. Kieke, J.W. Schoppelrei, T.B. Brill, Spectroscopy of Hydrothermal Reactions. 1. The CO_2−H_2O System and Kinetics of Urea Decomposition in an FTIR Spectroscopy Flow Reactor Cell Operable to 725 K and 335 bar, The Journal of Physical Chemistry, 100 (1996) 7455-7462.

[42] L. Zhou, W. Wang, L. Zhang, H. Xu, W. Zhu, Single-Crystalline $BiVO_4$ Microtubes with Square Cross-Sections: Microstructure, Growth Mechanism, and Photocatalytic Property, The Journal of Physical Chemistry C, 111 (2007) 13659-13664.

[43] L. Zhang, W. Wang, L. Zhou, H. Xu, Bi_2WO_6 Nano- and Microstructures: Shape Control and Associated Visible-Light-Driven Photocatalytic Activities, Small, 3 (2007) 1618-1625.

[44] L. Zhang, W. Wang, Z. Chen, L. Zhou, H. Xu, W. Zhu, Fabrication of flower-like Bi_2WO_6 superstructures as high performance visible-light driven photocatalysts, Journal of Materials Chemistry, 17 (2007) 2526-2532.

[45] A. Moulahi, F. Sediri, Pencil-like zinc oxide micro/nano-scale structures: Hydrothermal synthesis, optical and photocatalytic properties, Materials Research Bulletin, 48 (2013) 3723-3728.

[46] Q. I. Rahman, M. Ahmad, S. K. Misra, M. B. Lohani, Hexagonal ZnO nanorods assembled flowers for photocatalytic dye degradation: Growth, structural and optical properties, Super lattices and Microstructures, 64 (2013) 495–506.

[47] H. Usui, Surfactant concentration dependence of structure and photocatalytic properties of zinc oxide rods prepared using chemical synthesis in aqueous solutions. Journal of Colloid and Interface Science, 336 (2009) 667–741.

[48] T. Sun, J. Qiu, C. Liang, Controllable fabrication and photocatalytic activity of ZnO nanobelt arrays, The Journal of Physical Chemistry C, 112 (2008) 715–721.

[49] D. Kisailus, B. Schwenzer, J. Gomm, J.C. Weaver, D.E. Morse, Kinetically Controlled Catalytic Formation of Zinc Oxide Thin Films at Low Temperature, Journal of the American Chemical Society, 128 (2006) 10276-10280.

[50] M. Bitenc, P. Podbršček, P. Dubček, S. Bernstorff, G. Dražić, B. Orel, S. Pejovnik, Z. Crnjak Orel, In and Ex Situ Studies of the Formation of Layered Microspherical Hydrozincite as Precursor for ZnO, Chemistry – A European Journal, 16 (2010) 11481-11488.

Chapter 3

The contributions of the author of this thesis in the following chapter are: performance of experimental work (e.g. hydrothermal synthesis of ZnO, synthesis of the catalysts, evaluation of the catalysts performance in a conventional packed-bed reactor system, TPR/TPD characterization); interpretation and discussion of the results regarding the studied catalysts. Assembly of a carbon monoxide (CO) Infrared gas analyser to accurately quantify the produced ppm levels of CO during MSR, as an alternative analytical method with respect to the mass spectrometer. Dr. Cecilia Mateos Pedrero is acknowledged for her significant contribution as first author of the presented chapter.

The Pd-composite membrane reactor tests were conducted by the Institute on Membrane Technology (ITMCNR) as part of the collaboration related to the European Project BeingEnergy (303476).

The author of this thesis had a percentual contribution as part of the research team of 20 %.

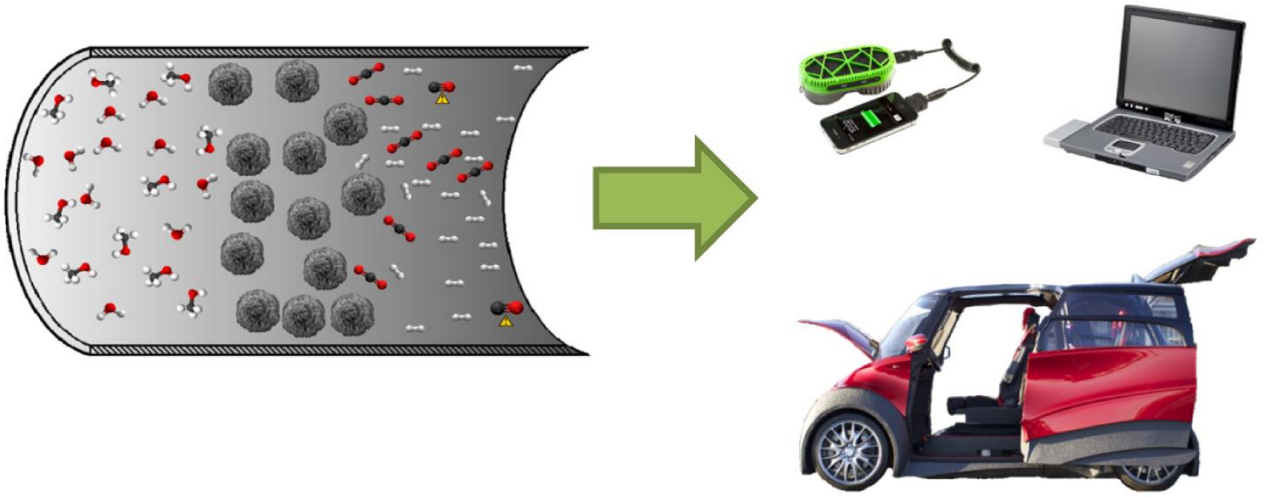

Chapter 3. CuO/ZnO catalysts for methanol steam reforming: the role of the support polarity and surface area[2]

Abstract

The effect of surface area and polarity ratio of ZnO support on the catalytic properties of CuO/ZnO catalyst for methanol steam reforming (MSR) are studied. The surface area of ZnO was varied changing the calcination temperature and its polarity ratio was modified using different Zn precursors, zinc acetate and zinc nitrate. It was found that the copper dispersion and copper surface area increase with the surface area of the ZnO support, and the polarity ratio of ZnO strongly influences the reducibility of copper species; a higher polarity ratio promotes the reducibility, which is attributed to a strong interaction between copper and the *more polar* ZnO support. Interestingly, it was observed that the selectivity of CuO/ZnO catalysts (lower CO yield) increases with the polarity ratio of ZnO carriers. As another key result, CuO/ZnO_{Ac375} catalyst has proven to be more selective (up to 90 %) than a reference $CuO/ZnO/Al_2O_3$ sample (G66-MR, Süd Chemie).

The activity of the best performing catalyst, CuO/ZnO_{Ac375}, was assessed in a Pd-composite membrane reactor and in a conventional packed-bed reactor. A hydrogen recovery of ca. 75 % and a hydrogen permeate purity of more than 90 % was obtained. The Pd-based membrane reactor allowed to improve the methanol conversion, by partially supressing the methanol steam reforming backward reaction, besides upgrading the reformate hydrogen purity for use in HT-PEMFC.

[2]C. Mateos-Pedrero, H. Silva, D.A. Pacheco Tanaka, S. Liguori, A. Iulianelli, A. Basile, Adélio Mendes, CuO/ZnO catalysts for methanol steam reforming: The role of the support polarity ratio and surface area, Appl. Catal. B Environ. 174-175 (2015) 67–76.

3.1. Introduction

The methanol steam reforming (MSR) reaction has received much attention in the past few decades as an attractive route of producing hydrogen for small-scale polymer electrolyte membrane fuel cells (PEMFC):

$$CH_3OH + H_2O \rightleftarrows 3H_2 + CO_2 \qquad \Delta H_0 = 49.7\ KJ \cdot mol^{-1} \qquad (3.1)$$

MSR catalysts are usually divided in two main groups: Cu-based and the more recent Pd-based ones [1]. Regardless the catalyst type ZnO support has a ubiquitous presence. Although CuO/Zn-based catalysts are used in industry since the 1960s, the role of ZnO in these catalysts system remains unclear despite the efforts made to elucidate its role [2-6]. For instance, Karim *et al.* investigated the effect of ZnO morphology on the reactivity of PdZnO catalysts for MSR [7] and concluded that the activity was higher for faceted ZnO materials [7]. In line with the former work, the theoretical studies by Smith *et al.* demonstrated that the polar crystalline surfaces of ZnO has null energetic barrier for both methanol and water dissociation [8]. On this basis, one could assume that ZnO with higher ratio of polar surfaces, namely higher polarity ratio, would lead to MSR catalysts with enhanced activity. This concept has in fact gained more attention as evident from the studies by Boucher et *al.* [9, 10], who investigated the influence of the properties of various carriers (mainly shape and defects) on the reactivity of Au-based catalysts for WGS and MSR reactions. These authors concluded that for different ZnO nanoshapes the activity increased when the binary catalysts were prepared with *more polar* supports (higher polarity ratio). Nevertheless, to our knowledge there is no study over CuO/ZnO catalysts that establishes a relation between the support polarity and the selectivity towards MSR. However, this aspect is of crucial importance for fuel cell applications where the presence of CO should be minimized as much as possible since even ppm levels of CO irreversibly poison Pt electrodes.

Recently, a simple urea-assisted hydrothermal method for tailoring the physicochemical properties of ZnO materials was reported by the research team [11]. It was found that the specific surface area, morphology and polarity ratio of the resulting ZnO solids were strongly affected by the synthesis conditions employed

[11], in particular, the presence and concentration of surfactant (Pluronic P123) and type of metal salt precursor (Zn-acetate vs. Zn-nitrate). The main conclusions of this study were: (i) the addition of Pluronic P123 results in better dispersion of ZnO particles (hierarchical ZnO microflowers are formed), higher polarity ratio (higher ratio of (002) polar planes), and ZnO materials with enhanced surface area; (ii) the morphology, polarity ratio and reactivity are also affected by the Zn salt used as precursor. The use of Zn-nitrate led to urchin-like ZnO structures (ZnO microflowers were formed when using Zn-acetate) with lower polarity ratio (higher proportion of (100) non-polar planes) than their acetate derived counterparts . The ZnO sample with the highest polarity ratio (the acetate derived ZnO) also exibithed the highest photoactivity, which is *ca.* 2 times higher than that of the "*less polar*" (lower polarity ratio) nitrate derived ZnO. These results suggest that both samples have different reactivity, being higher for the ZnO with higher polarity ratio [11].

MSR reaction should be carried out at low temperature to exploit the favorable thermodynamics to yield low CO, but it is equilibrium limited and then, for high conversions, the back reaction penalizes the overall reaction rate. The use of a Pd-based membrane reactor allows hydrogen product to be continuously removed from the reaction medium and then enhances the overall reaction kinetics resulting in enhanced conversions and in the production of a high purity hydrogen stream. Low temperature PEMFCs require hydrogen with very low concentrations of CO; the automotive standard imposes a maximum CO concentration of 0.2 ppm (ISO 14687-2). This high purity hydrogen can be obtained using a Pd-based purification process or, with advantages, using a Pd-based membrane reactor. However, Pd-membranes are poisoned by CO, which adsorbs on the membrane surfaces inhibiting the hydrogen permeation [12]. Pd-based composite membranes are characterized by a thin Pd layer deposited onto porous substrates and show high permeability and selectivity to hydrogen [13-16]. A growing attention is then been devoted to Pd-composite membranes that have - among others - the advantage of lower cost and higher permeability because of the reduced palladium content utilized in these membranes [13-18]. Numerous studies deal with MSR reaction carried out in both dense and composite Pd-based MRs [17-25]. In most of them, it has been demonstrated that these MRs made possible higher performances than conventional

packed bed reactors (CR) in terms of methanol conversion and hydrogen yield with the further benefit of producing high-grade hydrogen. Dense self-supported Pd-Ag membranes with a thickness of 50 μm and composite Pd-based membranes with Pd-layers thicker than 10 μm were used in previous in previous studies of steam reforming of methanol [18, 21-23]. This work used a thin composite membrane of *ca.* 8 μm deposited onto a ceramic support and the direct content of the catalyst with the composite membrane is accessed in terms of methanol conversion, hydrogen recovery and hydrogen permeate purity as well as permeation characteristics stability.

In this context, the first part of this work investigates the role of ZnO surface area and polarity ratio on the activity-selectivity of CuO/ZnO catalysts at low temperature. Two types of ZnO samples were prepared as detailed in [11] and used as supports of CuO/ZnO catalysts: a series of ZnO samples with different specific surface area and similar polarity and a group of ZnO samples with similar specific surface area but different polarity ratio. It should be noted, however, that in the present work the term "polarity ratio" is used to refer the relative intensities of the polar and nonpolar planes of ZnO, **(**$I_{(002)}/I_{(100)}$**).** A commercial isotropic würtzite ZnO from Sigma-Alldrich was taken as a reference and studied by XRD. The reference ZnO sample gave a value 0.73 for the (002)/(100) intensity ratio, thus, intensity ratio values higher than the würtzite reference **(**$I_{(002)}/I_{(100)}=0.73$**)** denote a higher polarity ratio, and consequently, a higher ratio of exposed polar facets, and *vice-versa*.

The second part of this work evaluates the performances of the best CuO/$ZnO_{Ac\text{-}375}$ catalyst, among the ones reported in this work, in a Pd-membrane reactor.

3.2. Experimental

3.2.1. Preparation of ZnO supports

ZnO samples were prepared by a modified hydrothermal method as detailed elsewhere [11]. In a typical preparation, 1.1 g of Zn salt precursor (zinc acetate or

zinc nitrate), 6 g of urea and 3 g of P123 Pluronic block copolymer were mixed 100 mL of water. The pH was adjusted to 5 and the solution was stirred for 2 hours under ambient conditions. Then, the mixture was poured into a teflon lined autoclave and kept at 90 °C for 24 h. The precipitate was thoroughly washed with distillated water and dried at 110 °C overnight. The resulting solid was calcined in a muffle furnace at given temperature for 30 min.

Table 3.1 - Table 1. Experimental parameters studied for the preparation of ZnO samples, calcination temperature series (ZnAc-CT: Ac Zn-acetate as precursor; CT: calcination temperature); Zn-precursor series (ZnOx-375: x stands for Zn-acetate (Ac) or Zn-nitrate (N); both samples were calcined at 375 °C).

Parameter studied	**Range**	**Sample name**	S_{BET} **($m^2 \cdot g^{-1}$)**	**Polarity*** $I_{(002)} / I_{(100)}$
Calcination temperature (CT) (°C)	300	Zn_{AC-300}	64	0.76
	350	Zn_{AC-350}	71	0.78
	375	Zn_{AC-375}	80	1.10
	400	Zn_{AC-400}	54	0.80
ZN-precursor	Zn-acetate	Zn_{AC-375}	80	1.10
	Zn-nitrate	Zn_{AC-375}	77	0.60

*Ratio between XRD plane (002) and plane (100) – indicates the polarity degree of the ZnO carriers. The polarity ratio of a isotropic würtzite ZnO from Sigma-Alldrich was 0.73.

Table 3.1 shows the ZnO samples prepared. The following nomenclature for ZnO samples was used (Table 3.1), ZnO*x*-CT, where: *x* denotes the zinc precursor, zinc-acetate (Ac) or zinc-nitrate (N) and CT represents the calcination temperature in °C (Table 3.1). Accordingly, the ZnAc-375 sample was prepared from zinc-acetate as precursor and calcined at 375 °C for 30 minutes. SEM images of the series ZnO materials (ZnO_{AC-CT}) obtained at different calcination temperatures are shown in Fig. 3.1.

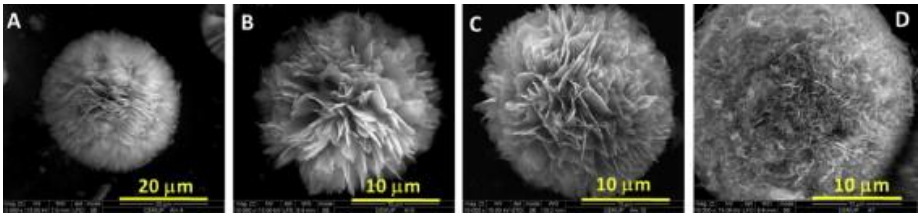

Figure 3.1 - Influence of the calcination temperature on the morphology of ZnOAc-CT samples: (A) before calcination and calcined in air at 300 °C (B), 375 °C (C) and 400 °C (D).

3.2.2. Preparation of the CuO/ZnO catalysts

CuO/ZnO catalysts were prepared by impregnation of the ZnO supports with an aqueous solution of copper nitrate (the amount of copper calculated to achieve a nominal metal loading of 15 wt. %). The pH was adjusted to 6 by dropwise addition of ammonium hydroxide. The resulting slurry was dried at 110 °C overnight and calcined at 360 °C during 8.5 h. As for ZnO carriers, CuO/ZnO catalysts will be denoted in terms of the ZnO supports calcination temperature (CT) and the type of zinc precursor used; thus when zinc nitrate was used the catalyst was named $CuO/ZnO_{N\text{-}CT}$ and when prepared from zinc acetate it was named $CuO/ZnO_{Ac\text{-}CT}$, where CT denotes the calcination temperature in °C.

3.2.3. Materials characterisations

The specific surface area was measured by N_2 physisorption at -196 °C in a Quantachrome Autosorb-1 Instruments apparatus. The surface area (S_{BET}) was calculated using the Brunauer-Emmett-Teller (BET) equation. X-ray powder diffraction (XRD) analyses were carried using a Cu-Kα radiation (30 KV/15 mA and λ=0.154 nm) in a Rigaku Miniflex 2 equipment. CuO crystallite size was assessed by the Debye-Scherrer equation, $D = K\lambda/(\beta\cos\theta)$, where D is the average size of the CuO crystallites, K is the Scherrer's constant 0.94, λ is the wavelength of X-ray, and β is the full width at half maximum. The XRD pattern was measured at ambient temperature and for the calcined samples of CuO/ZnO at a 2θ range of 10-80° with a

step width of 0.06°·s^{-1}. Temperature-programmed reduction (TPR) experiments were performed using a ChemBET Pulsar TPR/TPD equipped with a thermal conductivity detector (TCD). In a typical TPR experiment approximately 50 mg of sample was held by quartz wool and placed in a Ushaped quartz reactor. The sample was heated from 50 °C to 400 °C at a heating rate of 5 °C·min^{-1} under a flow of 5 % H_2/Ar. Hydrogen consumption was measured by TCD. The copper dispersion was determined by temperature programmed desorption of H_2 (H_2-TPD), following a similar procedure as reported by Amorim de Carvalho *et al.* [26]. Accordingly, the sample was reduced under a flow of 5 % H_2/Ar. Then, the sample was cooled to 0 °C with an ice bath and pure H_2 was passed during 1 h. Then, the temperature was lowered to -196 °C using liquid nitrogen under a pure H_2 flow (30 cm^3·min^{-1}). After 1 h, H_2 was switched to He flow (50 cm^3·min^{-1}) for 30 min. The temperature was then raised up to the 400 °C and desorption of H_2 was monitored by using a TCD detector. Copper dispersion is defined as the ratio of the surface copper atoms to the total copper atoms present in the catalyst.

3.2.4. MSR with a conventional reactor

The activity and selectivity of the catalysts were determined for MSR reaction using an in house built set-up. Steam reforming of methanol was performed at atmospheric pressure in a tubular reactor (7.25 mm i.d.) placed inside an oven. The reaction temperature was recorded inside the packed bed reactor using a thermocouple. The reactor was loaded with 200 mg of catalyst (180-350 µm) diluted with 200 mg of glass spheres. Plug flow conditions were ensured keeping catalyst bed length to catalyst size ratio above 50 ($L_{reactor}/d_{particle} \geq 50$) and the reactor diameter to size ratio above 30 ($d_{reactor}/d_{particle} \geq 30$) [27]. Activity measurements were performed in the temperature range of 180 °C to 300 °C and space-time ratio of $W_{cat.}/F^0_{CH_3OH} = 83\,kg_{cat.} \cdot mol^{-1} \cdot s$. Prior to the catalytic activity measurements, the catalyst was reduced *in situ* using a diluted hydrogen stream (40 vol. % of H_2 balanced with N_2), at 240 °C for 2 h. The gas feed flow rate was controlled by mass flow controllers from Bronkhorst (model F-201C, ± 0.1 FS). Required flow rate of

methanol aqueous solution was controlled using a Controlled Evaporation and Mixing (CEM) system (Bronkhorst). The condensable reactants were separated from the gas mixture in a condenser at *ca*. 0 °C, placed outside the oven.

Hydrogen and carbon dioxide were analysed in a quadruple mass spectrometer (Pfeiffer Vacuum OmniStar GSD 320). Trace amounts of carbon monoxide were measured using a CO infra-red analyser (Signal Instruments, 7100 FM, accuracy: ± 0.2 ppm). The methanol conversion (X_{CH_3OH}) and CO output molar fraction (γ_{CO}) were calculated by applying equations (3.2) and (3.3).

$$\text{Methanol Conversion}: \; x_{MeOH} = \frac{Q_{CO,out} + Q_{CO_2,out}}{Q_{CH_3OH,in}} \tag{3.2}$$

$$\text{CO output molar fraction}: \; Y_{CO} = \frac{Q_{CO,out}}{Q_{TOT,out}} \tag{3.3}$$

3.2.5. MSR with a composite Pd-Al_3O_3 membrane reactor

A sketch of the Pd/Al_2O_3 membrane reactor (MR) used is shown in Figure 3.2. The composite Pd-based membrane is made of a thin Pd layer (~ 7 μm) deposited *via* electroless plating onto a porous Al_2O_3 support. The membrane has been produced at Nanjing University of Technology (the porous Al_2O_3 support is from Gao Q Funct. Mat. Co.), and used at ITM-CNR, with 7.5 cm of total length and 5.0 cm of active length, 1.3 cm of O.D. It was housed in a stainless steel module, having 12 cm of length, 1.5 cm of O.D., equipped with two gaskets at both membrane ends for preventing permeate and retentate streams to mix. The MR annulus was packed with the CuO/ZnO catalyst. Prior to the reaction tests, the permeability of the composite Pd-membrane to hydrogen has been obtained at T = 300 °C and for a transmembrane pressure (ΔP) of 1.0 bar.

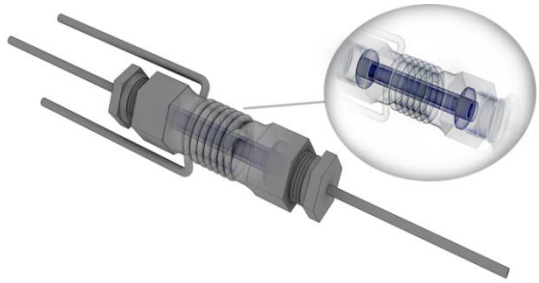

Figure 3.2 – Conceptual scheme of the composite Pd-Al2O3 MR with the catalyst (in powder form) packed in two the MR annulus.

The performance of the MR has been first analysed, in terms of methanol conversion and gas selectivity. The effect of temperature in the range 220 – 300 °C was assessed at 2.0 bar, ~ 0.95 h^{-1} weight hourly space velocity (WHSV) and H_2O/CH_3OH feed molar ratio equal to 2.5/1. The permeate pressure has been kept constant at 1.0 bar in the whole experimental campaign. Afterwards, the investigation has been focused on MR performance in terms of hydrogen recovery and hydrogen permeate purity by varying both reaction pressure and WHSV. The reaction pressure was varied from 1.5 bar to 2.5 bar, WHSV from 1.37 h^{-1} to 2.73 h^{-1}. The temperature was kept constant at 330 °C and H_2O/CH_3OH feed molar ratio equal to 1.5/1.

The MR has been heated up under helium and a P680 HPLC pump (Dionex) has been used for supplying liquid methanol and water. The mixture was vaporized with nitrogen supplied at a constant flow rate of 22.0 mL/min and fed to the MR. The retentate stream was directed to a cold trap in order to condensate the unreacted water and methanol. Both permeate and retentate stream compositions were analysed using a temperature programmed HP 6890 GC with two thermal conductivity detectors, heated at 250 °C and using Ar as carrier gas. The GC was equipped with three packed columns: Porapack R 50/80 (8 ft 1/8 inch) and CarboxenTM 1000 (15 ft 1/8 inch) connected in series, and a Molecular Sieve 5 Å (6 ft 1/8 inch). The permeability of the membrane was obtained for monocomponent streams of H_2, N_2 and He using a bubble-flow meter; at least 10 experimental values were obtained.

Concerning the reaction tests, each experimental value obtained averages at least 10 measurements taken in a period of 120 min in steady-state conditions, with a relative difference smaller than 3 %. Before reaction, the catalytic bed was reduced using a mixture of hydrogen and helium ($1.1 \cdot 10^{-2}$ mol·min^{-1}) at 240 °C for 2 h.

The equations used for computing the parameters that characterise the Pd-based MR are indicated below.

Permeability characterizing parameters:

Ideal selectivity: $\alpha_{H_2/i} = \frac{L_{H_2}}{L_i}$ (3.4)

Permeance: $L_i = \frac{J_i}{\Delta P_i}$ (3.5)

where *i* can be He, N_2, H_2; J_i is the permeating flux of i-gas through the composite Pd/Al_2O_3 membrane.

Equation characterizing the reactor performance:

Methanol conversion: $X_{MeOH} = \frac{Q_{CO,out} + Q_{CO_2,out}}{Q_{CH_3OH,\text{in}}}$ (3.2)

Output molar fraction: $\gamma_i = \frac{Q_{i,\text{out}}}{Q_{TOT,out}}$ (3.3)

Hydrogen recovery: $R_{H_2} = \frac{Q_{H_2,permeate}}{Q_{H_2,\text{retentate}} + Q_{H_2,permeate}}$ (3.6)

Hydrogen permeate molar fraction: $y_{H_2} = \frac{Q_{H_2,permeate}}{Q_{TOT,permeate}}$ (3.7)

where $Q_{CO,out}$, $Q_{CO_2,out}$ and $Q_{TOT,out}$ are the CO, CO_2 and total outlet molar flow rates, respectively, $Q_{H_2,\text{retentate}}$ and $Q_{H_2,\text{permeate}}$ are the H_2 outlet molar flow rates of

retentate and permeate sides; and $Q_{TOT,retentate}$ and and $Q_{TOT,permeate}$ are the total outlet molar flow rates of retentate and permeate sides; $Q_{CH_3OH,in}$ is the inlet stream of methanol fed to the MR and $Q_{i,out}$ is the outlet molar flow rate of "i"-component (CO, CO_2, H_2).

3.3. Results and Discussion

3.3.1. Physicochemical characterization

The XRD patterns of some representativeZnO supports and CuO/ZnO catalysts are shown in Figure 3.3. All CuO/ZnO samples present well defined peaks which can be ascribed to ZnO (würtzite, JCPDS file no. 36-1451) and CuO (tenorite, JCPDS file no. 48-1548). It is important to note that the polarity ratio (defined as $I_{(002)}/I_{(100)}$) of ZnO supports remained unchanged after copper impregnation (Figure 3.3): this evidences that copper deposition does not alter at least in a significant way the structure of the ZnO carriers, which maintain the initial preferential exposure of polar ($ZnO_{Ac\text{-}375}$) or nonpolar ($ZnO_{N\text{-}375}$) faces (Figure 3.3)

As seen in Table 3.2, the average CuO crystallite was not significantly affected either by the Zn-precursor (Table 3.2) or by the support calcination temperature. Most samples have similar crystallite size (16-18 nm, Table 3.2). The $CuO/ZnO_{Ac\text{-}400}$ sample has the largest CuO crystallite size (*ca.* 20 nm), which is likely due to the lower specific surface area of the ZnO support ($ZnO_{Ac\text{-}400}$, Table 3.1).

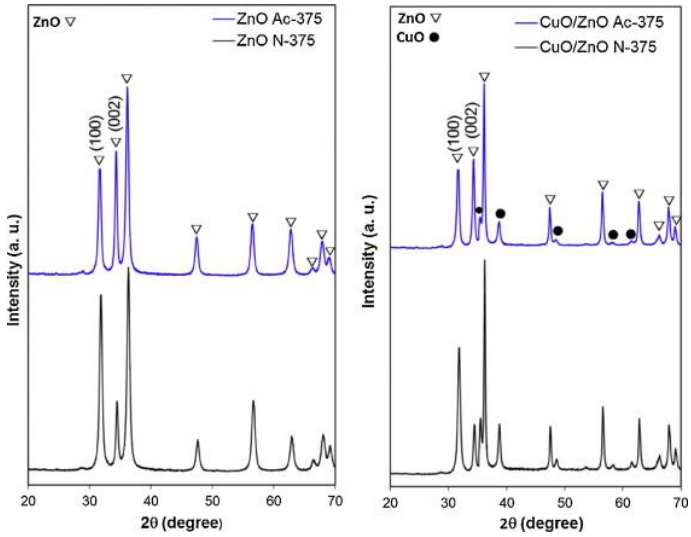

Figure 3.3 – XRD patterns for calcined CuO/ZnO catalysts.

Table 3.2 - H_2-TPR data, CuO mean crystallite size and dispersion for CuO/ZnO samples.

Sample	d_{CuO}[a] (nm)	S_{Cu}[b] (m^2/g)	D[c] (%)	$T_{max.}$ (°C)				Overall TPR peak area (au)	Peak contribution to the overall TPR peak area (%)	
				P_1	P_2	P_3	P_4	A	LT-peak	HT-peak
$CuO/ZnO_{Ac\text{-}300}$	18	4.7	12	220	247	272	339	2276	79	21
$CuO/ZnO_{Ac\text{-}350}$	18	6.1	18	214	233	257	320	2878	88	12
$CuO/ZnO_{Ac\text{-}375}$	16	23.1	26	173	287	-	-	5470	91	9
$CuO/ZnO_{Ac\text{-}400}$	20	2.4	7	202	303	-	-	1762	81	19
$CuO/ZnO_{N\text{-}300}$	17	18.9	22	234	260	290	335	3017	87	13

[a]: CuO mean crystallite size determined from Debye Scherrer's method; [b]: copper surface determined by H_2 TPD experiments; [c] : copper dispersion: ratio between amount of surface copper and total copper content

The temperature programmed desorption with H_2 was performed to evaluate the surface copper area the dispersion of copper. This technique was used as an alternative to the N_2O chemisorption since N_2O multilayer adsorption on copper oxide and N_2O dissociation by other catalyst components have been reported [26, 28-29]. Additionally, the utilization of the H_2 TPD procedure appears to be easier and precise when compared to other methods.

Clearly both the copper surface and the dispersion increases steadily with the surface area of ZnO support according to the following trend: CuO/ZnO_{Ac-400} << CuO/ZnO_{Ac-300} < CuO/ZnO_{Ac-350} < CuO/ZnO_{N-375} ~ = CuO/ZnO_{Ac-375} (Table 3.2, Figure. 3.5).

The H_2-TPR profiles of CuO/ZnO catalysts prepared with ZnO supports calcined at different temperatures are shown in Figures 3.4A and 3.4B. The morphology of the TPR curves, intensity and reduction temperature for these groups of samples are different, indicating that the calcination temperature of the ZnO support affects the reducibility of copper species. According to the shape of the TPR curve, this series of samples can be grouped as follows: low temperature (CuO/ZnO_{Ac-300} and CuO/ZnO_{Ac-350}, Figure 3.4A) and high temperature samples (CuO/ZnO_{Ac-375} and CuO/ZnO_{Ac-400}, Figure 3.4B), henceforth labelled as LT- and HT-catalysts, respectively.

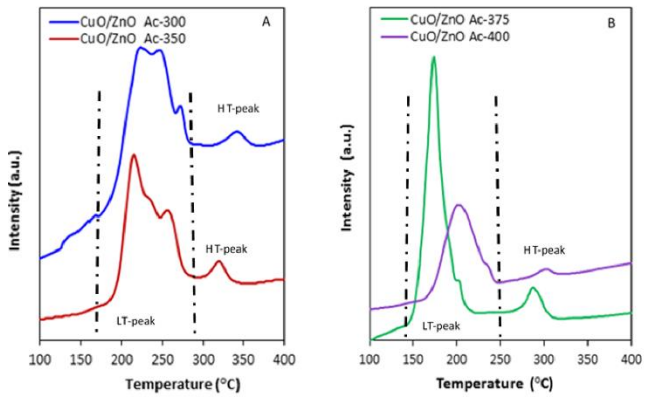

Figure 3.4 – TPR profiles of the CuO/ZnOAc-300 and CuO/ZnOAc-350 (A) and CuO/ZnOAc-375 and CuO/ZnOAc-400 (B) samples.

The LT-catalysts present very complex TPR profiles (Figure 3.4A). A broad reduction peak is observed in the 200 - 300 °C temperature range, with maxima at 220 °C, 247 °C and 272 °C, and 214 °C, 233 °C and 257 °C (denoted as P1, P2 and P3 in Table 3.2) for CuO/ZnO_{Ac-300} and CuO/ZnO_{Ac-350}, respectively. A small H_2 uptake (HT-peak in Figure 3.4A) between 300 and 350 °C is also seen. The existence

of several peaks implies that different kinds of reducing copper oxide sites (with different environments, particle sizes, and/or oxidation state) coexist in the LT-catalysts. On the other hand, the broadness of the TPR curves shown in Figure 3.4A could be likely due to the broad size distribution of the copper oxide particles.

The TPR profiles of the HT-catalysts (Figure 3.4B) are dominated by a major peak centered at 173 °C and 202 °C for $CuO/ZnO_{Ac\text{-}375}$ and $CuO/ZnO_{Ac\text{-}400}$, respectively. As for the abovementioned LT-catalysts, a small peak above 275 °C is observed (HT-peak in Figure 3.4 B). Despite their similarities, the $CuO/ZnO_{Ac\text{-}375}$ sample shows a great higher hydrogen consumption accompanied by a lower reduction temperature (Table 3.2), indicating an easier reducibility of Cu^{2+} cations on this sample. HT-catalysts exhibit reduction peaks considerably sharper and more symmetric than their LT-counterparts, suggesting smaller copper oxide particles with narrow size distribution.

According to the literature, the LT-peaks (150 °C - 300 °C) can be assigned to the reduction of copper oxide species in intimate contact with zinc oxide [30, 31], since a strong interaction with ZnO can promote the reduction of CuO [30, 31]. The small HT-peak (300 °C - 350 °C) may suggest the presence of a minor portion of CuO interacting less strongly with ZnO and/or larger CuO crystallites that need higher temperatures to be reduced.

In either case all CuO/ZnO samples exhibit reduction temperatures much lower than that for bulk CuO. This fact is consistent with other published works reporting that the addition of promoters facilitates the reduction of copper oxide [30, 31].

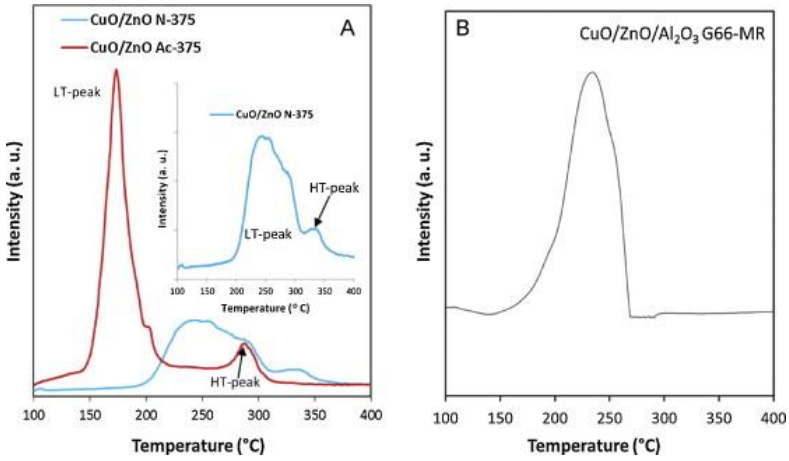

Figure 3.5 – TPR profiles of the CuO/ZnO samples prepared from different Zn-precursor, CuO/ZnOAc-375 and CuO/ZnON-375 (A) and commercial CuO/ZnO/Al2O3 (66/24/10 wt.%) catalyst (G66-MR) supplied by Süd-Chemie (B).

The TPR profiles for the catalysts prepared from different Zn-precursor ($CuO/ZnO_{N\text{-}375}$ and $CuO/ZnO_{Ac\text{-}375}$) displayed in Figure 3.5A clearly highlight the large differences between both samples (curve shape and intensity, reduction temperature). The lower reduction temperatures along with the higher hydrogen consumption shown by $CuO/ZnO_{Ac\text{-}375}$ are clear indications of an enhanced reducibility of Cu^{2+} species. Such an improvement could be due to: (i) a higher dispersion (smaller size) of copper particles, and/or (ii) a strong interaction between copper species and the polar ZnO carrier. The first hypothesis seems unlike in view of the fact that both samples have comparable copper particle sizes (as showed by XRD and HR-TEM, see Table 3.2) and dispersion (Table 3.2). On the other hand, both samples were prepared from ZnO carriers with very different polarity, namely, preferential exposure of polar ($CuO/ZnO_{Ac\text{-}375}$) or nonpolar facets ($CuO/ZnO_{N\text{-}375}$). TPR results evidence that the reducibility of our CuO/ZnO catalysts is notably influenced by the polarity of ZnO carrier. Moreover, the symmetric shape of the LT-peak for the *more polar* sample, $CuO/ZnO_{Ac\text{-}375}$, suggests a narrow size distribution of copper species on this sample.

As indicated before, the LT-peak represents copper species intimately interacting with ZnO and from Figure 3.5A is clear that the fraction of these species is higher in

the *more polar* sample. Thus, it could be concluded that ZnO polar surfaces interacts strongly, at least to a higher extent than the *less polar* ZnO surfaces ($ZnO_{N\text{-}375}$), with highly dispersed copper particles modifying their electronic properties, and resulting in samples with enhanced reducibility. A recent study of Pd/ZnO catalysts pointed out in the same direction [32]. In fact, authors reported preferential formation of a PdZnβ alloy on polar ZnO facets [32], suggesting a different interaction between palladium particles and polar ZnO surfaces, as in the present case.

3.3.2. Catalytic activity of CuO/ZnO samples in conventional reactor

The evolution of methanol conversion with the reaction for some reprensentative CuO/ZnO catalysts is presented in Figure 3.6. Overall the methanol conversion, H_2 and CO_2 yields increase with temperature, as expected (Figure 3.6, Table 3.3). Regardless the catalyst and the temperature, H_2 and CO_2 are the main products with CO formation initiating at 300 °C when methanol approaches complete conversion (Table 3.3). No CO was observed below 300 °C, expecting for $CuO/ZnO_{N\text{-}375}$ (Table 3.3). This is easily understood since CO is a by-product produced by endothermic reactions methanol decomposition (MD) and reverse water gas shift (RWGS) [1].

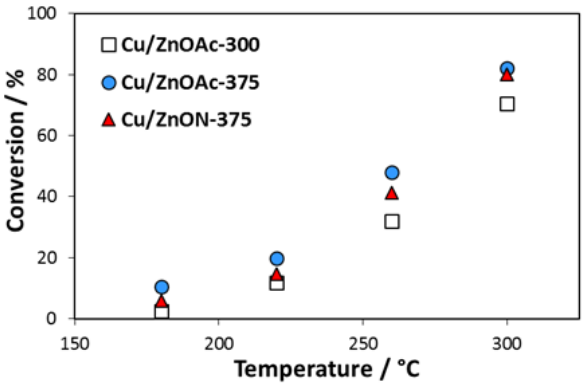

Figure 3.6 – Evolution of methanol conversion with reaction temperature for CuO/ZnOAc-300, $CuO/ZnO_{Ac\text{-}375}$ and $CuO/ZnO_{N\text{-}375}$ catalysts $\left(W_{cat}/F^{0}_{CH_3OH} = 83 kg_{cat} \cdot mol^{-1} \cdot s\right)$.

Table 3.3 - Methanol conversion, CO_2 and H_2 yields, and CO amount measured at 220 °C and 300 °C in the conventional fixed bed reactor; $\left(W_{cat}/F^{0}_{CH_3OH} = 83 kg_{cat} \cdot mol^{-1} \cdot s\right)$.

Sample	Activity ($\mu mol/g_{met}$ s)	X_{CH_3OH} (%)		y_{CO_2} (%)		y_{H_2} (%)		CO[b] (µmol)
Temperature (°C)	**180**	**220**	**300**	**220**	**300**	**220**	**300**	**300**
$CuO/ZnO_{Ac\text{-}300}$	20.8	11.7	70.6	11.6	70.3	11.7	73.1	1.32
$CuO/ZnO_{Ac\text{-}350}$	22.6	13.8	74.8	13.7	76.6	13.8	76.5	1.29
$CuO/ZnO_{Ac\text{-}375}$	39.6	15.9 (<1)	82.2 (1.8)	15.7	80.9	16.1	84.1	1.06 (0.015)
$CuO/ZnO_{Ac\text{-}400}$	17.4	7.9	64.2	7.8	60.1	7.9	62.5	1.25
$CuO/ZnO_{N\text{-}375}$	24.1	14.7 (<1)	80.1 (2.4)	14.1	72.7	14.3	75.6	7.42 (0.010)
$Cu/ZnO/Al_2O_3$[a]	7.65	63.8	90.1	60.3	82.1	62.1	83.5	9.61

[a]: Commercial $CuO/ZnO/Al_2O_3$ (66/24/10 wt. %) catalyst (G66-MR) supplied by Süd Chemie. Values in brackets correspond to conversion and µmol of CO obtained when MSR tests were performed only with ZnO support; [b]: corresponds to the CO reformate concentration at 300 °C, no CO was detected below this temperature (< 0.5 µmol/mL) except for $CuO/ZnO_{N\text{-}375}$ sample that produces 1.67 µmol/mL and 3.1 µmol/mL of CO at 220 °C and 260 °C, respectively.

The catalytic activity at 180 °C as a function of the specific surface of ZnO support and CuO dispersion is illustrated in Figure 3.7. Overall, the activity of the CuO/ZnO catalyst increases with the copper dispersion, with the later increasing as the surface area of ZnO support does. ZnO supports with larger surface areas are able to better disperse Cu particles, leading to a higher number of exposed active sites (Cu sites) and consequently to a higher activity. It is also interesting to note that catalysts prepared from ZnO supports with similar surface areas ($CuO/ZnO_{Ac\text{-}375}$ and $CuO/ZnO_{N\text{-}375}$) have comparable copper dispersion and behave similarly in terms of activity (Figure 3.7), in good agreement with our previous assumption.

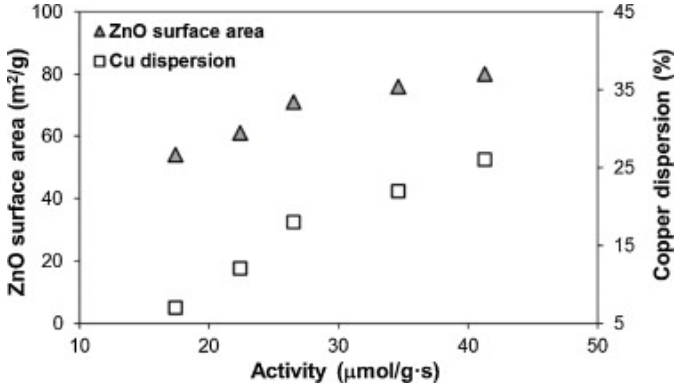

Figure 3.1 - Catalytic activity at 180 °C as a function of the specific surface area of ZnO carriers and copper dispersion.

Under the conditions of the present study, the dispersion of copper (or copper surface area) is the predominant factor governing the activity of CuO/ZnO catalysts in MSR. This agrees with other published results [33-35] reporting a linear correlation between the activity of Cu-based catalysts and the copper surface area.

On the contrary, there is no clear correlation between the CO production and the surface area of ZnO carriers or copper dispersion. In fact, all the catalysts obtained from ZnO with different S_{BET} produce similar amounts of CO (Table 3.1 and 3.3, series of CT catalysts). However, the two catalysts with similar surface areas but very different polarity ratio ($CuO/ZnO_{Ac\text{-}375}$ and $CuO/ZnO_{N\text{-}375}$) show the largest difference in selectivity. Clearly, the different selectivity of $CuO/ZnO_{Ac\text{-}375}$ and $CuO/ZnO_{N\text{-}375}$ samples cannot be ascribed to the ZnO surface area or copper dispersion.

The CO produced at 300 °C as a function of the ZnO polarity ratio is illustrated in Figure 3.8. Data presented in this figure suggests that the selectivity (regarded as CO produced) is related to the polarity ratio of the ZnO supports, or in other words to the preferential exposure of polar or nonpolar facets of ZnO. In fact, copper catalysts supported on ZnOs with similar polarity ratio (Table 3.1), which in turn are very close to that of the würtzite reference (no anisotropic), produced nearly the same amount of CO (Table 3.3, Figure 3.7). Conversely, copper catalyst supported on the ZnOs showing the highest difference in polarity ratio $ZnO_{N\text{-}375}$ $ZnO_{Ac\text{-}375}$ (Table 3.1),

which in turn are significantly different from that of the würtzite reference (anisotropic), show also the largest differences in selectivity (Table 3.3, Figure 3.7): the lower the polarity ratio, the higher the CO production (Figure 3.9). Thus, a *more polar* ZnO support gives more selective samples ($CuO/ZnO_{Ac\text{-}375}$), namely, producing lower CO amounts and *vice versa*.

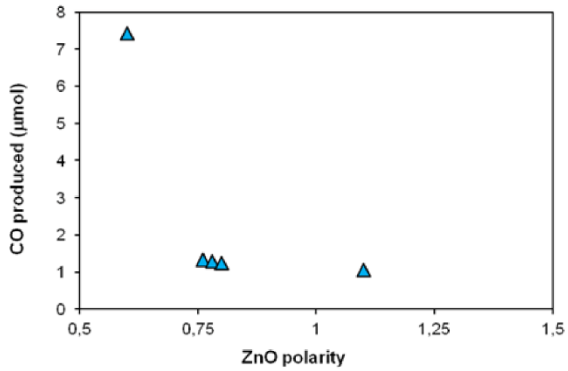

Figure 3.2 - Evolution of CO concentration (at 300 °C) as a function of the polarity ratio of ZnO carriers.

The polarity of ZnO is linkely related to the presence of defects. Typical ZnO materials exhibit a würtzite structure with the polar planes corresponding to the basal planes of the hexagonal würtzite unit cell [36-38]. The würtzite configuration has preferential exposure of non-polar facets (lower polarity ratio). It is well-accepted that higher proportion of polar facets means also a higher number of defects, such as oxygen vacancies, that may play a crucial role in methanol and water activation [39, 40]. It might be thought that the polar ZnO support itself is responsible for the enhanced MSR selectivity. In order to verify this hypothesis, MSR activity measurements were conducted over both polar ($ZnO_{Ac\text{-}375}$) and nonpolar ($ZnO_{N\text{-}375}$) ZnO samples under the same operating conditions as those used for CuO/ZnO samples. It was observed that both supports give very low methanol conversions (< 3 %) with almost complete selectivity towards CO_2 (so, negligible CO production - Table 3.3). Therefore, the ZnO support alone does not explain the enhanced selectivity.

It is then reasonable to assume that in the present case the nature of copper ZnO support interaction (evidenced by TPR) could account for the differences in selectivity.

ZnO was also found to affect the activity and selectivity of PdZnO catalysts in MSR reaction [32]. In line with this finding, a recent study about the influence of ZnO facets on the performances of Pd/ZnO catalysts for MSR also reached the same conclusion [41, 42]. Authors reported that at comparable Pd/ZnO catalyst composition, the polar sample was more selective than the nonpolar due to the preferential formation of the PdZnβ phase, which is selective towards CO_2, on the polar ZnO [41, 42].

From the results compiled in Table 3, it can be inferred that the polarity ratio of ZnO support does not exert any promoting effect on activity but clearly affects the selectivity (Figure 3.7). TPR results evidenced strong interactions between copper and the *more polar* $ZnO_{Ac\text{-}375}$ support, which facilitates the reducibility of copper oxide leading to enhanced selectivity (decreases CO formation). This suggests that sites of particular reactivity may exist at the Cu–ZnO *polar* interfaces that are responsible for the higher selectivity of the *more polar* catalyst, $CuO/ZnO_{Ac\text{-}375}$. Despite our results do not allow identifying the exact role of the ZnO polarity ratio on the selectivity of CuO/ZnO catalysts, they clearly point out to its relevant role on the selectivity of the catalyst and suggest that the CuO-ZnO interface is involved in the MSR selectivity.

Another interesting finding of the present study is that the activity (per mass of metal) at 180 °C of the best in-house catalyst, $CuO/ZnO_{Ac\text{-}375}$, is up to 5-fold higher (Table 3.3) than that of a commercial $CuO/ZnO/Al_2O_3$ catalyst (66/24/10 wt. %; G66-MR, from Süd Chemie). Moreover, at comparable methanol conversion (300 °C, Table 3.3) the in-house sample produces considerably less CO (up to 90% lower, Table 3.3), further evidencing the high selectivity of CuO/ZnOAc-375 catalyst.

The first part of this study identified catalyst $CuO/ZnO_{Ac\text{-}375}$ to have the highest catalytic activity among the prepared catalysts and the highest selectivity of all

catalysts. This catalyst was then selected to pack a Pd-based membrane reactor. The results obtained are presented and discussed in the next section.

3.3.3. *Catalytic activity of CuO/ZnO_{AC-375} in the Pd/Al_2O_3 composite membrane reactor*

Before the reaction tests, the permeation characteristics of the fresh Pd/Al_2O_3 membrane were investigated at T = 300 °C and ΔP = 1.0 bar. Table 3.4 shows the ideal selectivities obtained during the pure gas permeation tests.

Table 3.4 - Permeation characteristics of the fresh composite Pd/Al_2O_3 membrane at 300 °C and ΔP = 1.0 bar.

Pure gas (i)	J_i (mol·$^{-2}$·s^{-1})	Permeance$_i$ (mol·$^{-2}$·s^{-1}·Pa^{-1})	$\alpha_{H_2/i}$
H_2	1.42x10^{-1}	1.42x10^{-6}	1
N_2	2.36x10^{-5}	2.36x10^{-10}	>6000
He	4.29x10^{-5}	4.29x10^{-10}	~ 3300

The MSR on the composite Pd/Al_2O_3 MR were carried out by varying the temperature in the range 220 - 300 °C, at 2.0 bar, H_2O/CH_3OH feed molar ratio of 2.5/1 and WHSV = 0.95 h^{-1}. The objective of this first experimental campaign was evaluating the CuO/ZnO_{Ac-375} catalyst performance in terms of activity and stability. Based on both permeate and retentate streams, Table 3.5 illustrates both methanol conversion and output molar fractions for different reaction temperatures. Though the composite Pd-based membrane has defects, besides hydrogen only CO_2 was found in the permeate stream. In particular, it is worth noting that a temperature increase allows two positive effects on the MR system: the first effect is related to the increase of the reaction rate with the temperature; the second one is due to the H_2 permeation through the membrane. In the latter case, at higher temperature the hydrogen permeation through the membrane is enhanced and, consequently, this induces a higher H_2 removal from the reaction to the permeate side, favouring the shift of the

MSR reaction towards further products formation as well as higher methanol consume.

Table 3.5 - Methanol conversion (into gas) and output molar fractions (H_2, CO and CO_2) at different temperatures, WHSV = 0.95 h^{-1} and transmembrane pressure = 1.0 bar

	Temperature (°C)		
Overall product molar fraction (%)	220	260	300
H_2	74.56	74.46	74.18
CO	0.75	0.88	1.25
CO_2	24.69	24.66	24.57
CH_3OH conversion (%)	12.4	47.1	97.4

Figure 3.10 highlights the stability of the catalyst as confirmed by the constant trend of H_2, CO, CO_2 selectivities with respect to time on stream up to 3 h of operation at steady state conditions. A similar trend was confirmed in all the MR experimental tests of this work, suggesting that the catalyst is stable under long time operation.

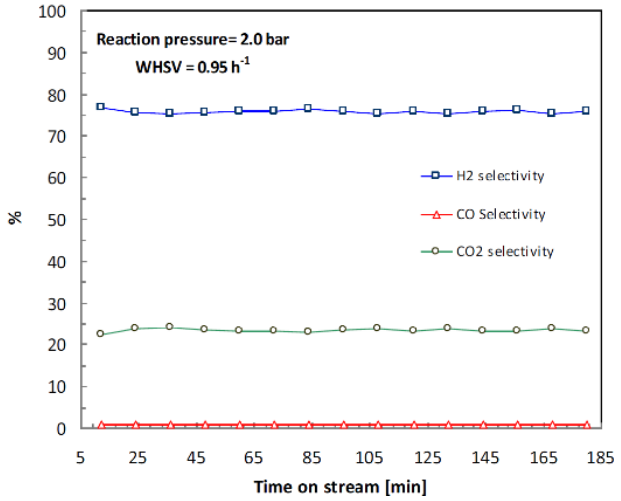

Figure 3.3 - Overall product molar fraction vs time on stream for MSR reaction in the Pd/Al_2O_3 MR at T = 220 °C, transmembrane pressure = 2.0 bar, WHSV = 0.95 h^{-1}, H_2O/CH_3OH = 2.5/1.

Pressure Effect

The second campaign of experiments aimed to obtain high grade and high yields of hydrogen in permeate side. The reaction tests were carried out at 330 °C, feed molar ratio equal to 1.5/1, WHSV = 2.73 h^{-1} and by varying the reaction pressure between 1.5 - 2.5 bar. Table 3.6 shows the permeated hydrogen purity and the hydrogen recovery at 330 °C and at various reaction pressures.

Table 3.6 – Hydrogen permeate purity and hydrogen recovery vs reaction pressure at 330 °C H_2O/CH_3OH = 1.5/1 and WHSV = 2.73 h^{-1} during MSR reaction in the Pd/AL_2O_3 MR.

Pressure (bar)	H_2 permeate purity (%)	H_2 recovery (%)
1.5	90	57
2.0	90	62
2.5	88	64

The hydrogen recovery increases with the reaction pressure, overcoming 65 % at 2.5 bar. Indeed, the highest reaction pressure maximizes the permeation driving force to hydrogen favouring the hydrogen permeation and then the hydrogen recovery. Nevertheless, the permeated hydrogen purity decreases with the reaction pressure. The composite palladium membrane should have pinholes that allow the diffusion/convection of other gas species. As the reaction pressure increases, more hydrogen is removed from the reaction medium making its permeation driving force to decrease. At the same time, the driving force to the other gas species increases, causing the purity of hydrogen at the permeate side to decrease. On the other hand, no CO was detected in the permeate side, as shown in Table 3.7.

Table 3.7 – Flow rates of the gases present in the permeate stream at different reaction pressure during MSR reaction at 330 °C, WHSV = 2.73 h^{-1}.

	Reaction Pressure (bar)		
Flow rate gas in the permeate ($mL \cdot min^{-1}$)	1.5	2.0	2.5
H_2	1.27	1.90	1.97
CO_2	0.11	0.16	0.2

WHSV Effect

Hydrogen recovery and hydrogen permeate purity have been determined as a function of the WHSV at T = 330 °C, 2.5 bar reaction pressure and H_2O/CH_3OH feed molar ratio equal to 1.5/1. Table 3.8 shows that, as expected, the hydrogen recovery increases when WHSV decreases (higher residence times); the hydrogen recovery increased to around 75 % at 1.37 h^{-1}.

Table 3.8 – Hydrogen permeate purity and hydrogen recovery vs WHSV at 330 °C, H2O/CH3OH = 1.5/1 and reaction pressure = 2.5 bar during MSR in a Pd/Al_2O_3 MR.

WHSV (h^{-1})	H_2 permeate purity (%)	H_2 recovery (%)
1.37	88	72
2.05	88	66
2.73	87	63

Furthermore, the permeated hydrogen purity did not vary significantly with WHSV being *ca*. 91 %. Also in this case, no CO presence was noticed in the permeate side.

At the end of the whole experimental reaction campaigns, the permeation characteristics of the Pd/Al_2O_3 membrane have been checked again at T = 300 °C and ΔP = 1.0 bar. Table 3.9 reports the new ideal selectivities values, which are different from the fresh membrane; the permeability increased and the selectivity decreased by a factor of *ca.* 2. This probably occurred because of the effect of thermal cycles that greatly affect the gas permeation characteristics of the composite Pd-membrane.

Table 3.9 - Permeation characteristics of the composite Pd/Al_2O_3 membrane at the end of the whole experimental campaign.

Pure gas (i)	J_i (mol·$^{-2}$·s^{-1})	Permeance$_i$ (mol·$^{-2}$·s^{-1}·Pa^{-1})	$\alpha_{H_2/i}$
H_2	$9.87 \cdot 10^{-2}$	$1.95 \cdot 10^{-6}$	1
N_2	$2.60 \cdot 10^{-5}$	$5.14 \cdot 10^{-10}$	~ 3800
He	$6.70 \cdot 10^{-5}$	$1.32 \cdot 10^{-9}$	~ 1500

3.4. Conclusions

The effect of the surface area and polarity ratio (related to the facet defects) of ZnO supports on the activity-selectivity of CuO/ZnO catalysts for MSR was studied. The ZnO surface area was varied by changing the calcination temperature of the prepared ZnO materials, whereas, its polarity was modified using different Zn precursors, acetate or nitrate.

Both the copper surface area and the dispersion increased with the surface area of ZnO support. The polarity ratio of ZnO carrier carrier did not significantly affectcopper dispersion dispersion but it influences notably the reducibility of copper species. A higher polarity ratio of ZnO promotes the reducibility of copper oxide, which is attributed to a strong interaction between copper species and the *more polar* facets of ZnO, which in higher proportion in the ZnO support with higher polarity ratio.

The activity of CuO/ZnO catalysts shows a marked dependence on the surface area of the ZnO supports, which in turn affect the dispersion of copper. In fact, those catalysts with higher surface area (and also Cu dispersion) also exhibit higher activity. Interestingly, the experimental results evidence that the selectivity of CuO/ZnO catalysts is closely related to the polarity ratio of ZnO carriers: the selectivity increases with the polarity ratio, probably due to the presence of more selective Cu-ZnO sites at the Cu-ZnO polar interface. The $CuO/ZnO_{Ac\text{-}375}$ catalyst also shows a drastic improvement of selectivity as compared to commercial $CuO/ZnO/Al_2O_3$ sample. In fact, at similar methanol conversion the in-house catalyst has proven to be up to 90 % more selective than the commercial sample.

Best performing catalyst $CuO/ZnO_{Ac\text{-}375}$ was further tested in a Pd-membrane reactor, made of a thin Pd-layer deposited on Al_2O_3 support. Two studies were performed, one concerning the catalyst performance in terms of methanol conversion and gas selectivity stability and the other concerning the MR performance in terms of hydrogen recovery and hydrogen permeate purity for various operating conditions.

During the first set experiments, the best result has been reached for 300 °C, 2.0 bar and WHSV = 2.73 h^{-1} with 97 % of methanol conversion. Furthermore, a

good stability of both conversion and gas selectivity was observed. The second set of experiments allowed to achieve a hydrogen recovery of *ca.* 75% and a hydrogen permeate purity higher than 90 % at 330 °C, 2.5 bar and WHSV = 1.37 h^{-1}. This work pointed out that the Pd-based MR allows obtaining higher methanol conversions and a high purity permeate hydrogen, free of CO.

3.5. Acknowledgement

The authors would like to thank the European Union's Seventh Framework Programme (FP7/2007-2013) for the Fuel Cells and Hydrogen Joint Technology Initiative under grant agreement No [303476] due to the funding received for part of this work. This work was performed under the project "SYM – Produção de Metanol por Electrólise de Água, usando Electrodos de Grafite" (ref. FCOMP-01-0202-FEDER- 038899), financed by European Regional Development Fund (ERDF), through the Operational Program for Competitiveness Factors (POFC) in the National Strategic Reference Framework (NSRF), in the framework of the Incentive system for technology research and development. Dr. C. Mateos-Pedrero is grateful to the Portuguese Foundation for Science and Technology (FCT) for her Post-Doctoral grant (SFRH/BPD/97114/2013). Prof. Y. Huang of Nanjing Tech-University (China) is particularly acknowledged for the preparation of Pd-composite membrane used in this work. The work of H. Silva was supported by FCT, grant SFRH/BD/45890/2008.

3.6. References

[1] S. Sá, H. Silva, L. Brandão, J.M. Sousa, A. Mendes, Catalysts for methanol steam reforming—A review. Appl. Catal: B: Environ., 99 (2010) 43-57.

[2] G.C. Chinchen, K.C. Waugh, The activity and state of the copper surface in methanol synthesis catalysts, Appl. Catal. 25 (1986) 101-107.

[3] S.T. Yong, C.W. Ooi, S.P. Chai, X.S. Wu, Review of methanol reforming-Cu-based catalysts, surface reaction mechanisms, and reaction schemes, Int. J. Hydrogen En., 38 (2013) 9541-9552.

[4] M.S. Spencer, The role of zinc oxide in Cu/ZnO catalysts for methanol synthesis and the water– gas shift reaction, Top. Catal. 8 (1999) 259-266.

[5] M. Berens, F. Studt, I. Kasatkin, S. Kühl, M. Hävecker, F. Abild-Pedersen, S. Zander, F. Girgsdies, P. Kurr, B.L. Kniep, M. Tovar, R.W. Fischer, J.K. Nørskov, R. Schlögl,. The active site of methanol synthesis over Cu/ZnO/Al2O3 industrial catalysts, Science, 336 (2012), 893-897.

[6] Y. Kanai, T. Watanabe, T. Fujitani, T. Uchijima, J. Nakamura, The synergy between Cu and ZnO in methanol synthesis catalysts, Catal. Lett., 38 (1996) 157-163.

[7] A.M. Karim, T. Conant, A.K. Datye, Controlling ZnO morphology for improved methanol steam reforming reactivity, Phys. Chem. Chem. Phys., 10 (2008) 5584-5590.

[8] G.K. Smith, S. Lina, W. Laia, A. Datyeb, D. Xiec, H. Guo, Initial steps in methanol steam reforming on PdZn and ZnO surfaces: Density functional theory studies, Surface Sci., 605 (2011) 750-759.

[9] M.B. Boucher, S. Goergen, N. Yia, M. Flytzani-Stephanopoulos, Shape effects' in metal oxide supported nanoscale gold catalysts, Phys. Chem. Chem. Phys., 13 (2011) 2517-2527.

[10] M.B. Boucher, N. Yi, F. Gittleson, B. Zugic, H. Saltsburg, M. Flytzani-Stephanopoulos, Hydrogen Production from Methanol over Gold Supported on ZnO and CeO_2 Nanoshapes, The Journal of Phys. Chem.: C, 115 (2010) 1261-1268.

[11] H. Silva, C. Mateos-Pedrero, C. Magén, D.A. Pacheco-Tanaka, A. Mendes, Simple hydrothermal synthesis method for tailoring the physicochemical properties of ZnO: morphology, surface area and polarity, RSC Adv., 4 (2014) 31166-31176.

[12] Y.M. Lin, M. H. Rei, Study on hydrogen production from methanol steam reforming in supported palladium membrane reactor, Catal. Today, 67 (2001) 77-84.

[13] X. Hu, W. Chen, Y. Huang, Fabrication of Pd/ceramic membranes for hydrogen separation based on low-cost macroporous ceramics with pencil coating, Int. J. Hydrogen En., 35 (2010) 7803- 7808.

[14] Y. Huang, R. Dittmeyer, Preparation of thin palladium membranes on a porous support with rough surface, J. Membrane Sci., 302 (2007) 160-170.

[15] A.W. Li, J.R. Grace, C.J. Lim, Preparation of thin Pd-based composite membrane on planar metallic substrate part II. Preparation of membranes by electroless plating and characterization, J. Membrane Sci., 306 (2007) 159-165.

[16] S. Liguori, A. Iulianelli, F. Dalena, P. Pinacci, F. Drago, M. Broglia, Y. Huang, A. Basile, Performance and long-term stability of Pd/PSS and Pd/Al2O3 membranes for hydrogen separation, Membranes, 4 (2014) 143-162.

[17] N. Itoh, Y. Kaneko, A. Igarashi Efficient hydrogen production via methanol steam reforming by preventing back-permeation of hydrogen in a palladium membrane reactor, Ind. Eng. Chem. Res., 41 (2002), pp. 4702–4706.

[18] S. Liguori, A. Iulianelli, F. Dalena, V. Piemonte, Y. Huang, A. Basile, Methanol steam reforming in an Al_2O_3 supported thin Pd-layer membrane reactor over $Cu/ZnO/Al_2O_3$ catalyst, Int. J. Hydrogen En., in press, http://dx.doi.org/10.1016/j.ijhydene.2013.11.113.

[19] A. Basile, Hydrogen production using Pd-based membrane reactors for fuel cells, Top Catal., 51 (2008) 107-122.

[20] S. Sà, J.M. Sousa, A. Mendes, Methanol steam reforming in a dual-bed membrane reactor for producing PEMFC grade hydrogen, Catal. Today, 156 (2010) 254-260.

[21] A. Iulianelli, T. Longo, A. Basile, Methanol steam reforming in a dense Pd-Ag membrane reactor: The pressure and WHSV effects on CO-free H2 production, J. Membrane Sci., 323 (2008) 235-240.

[22] A. Iulianelli, T. Longo, A. Basile, Methanol steam reforming reaction in a Pd-Ag membrane reactor for CO-free hydrogen production, Int. J. Hydrogen En., 33 (2008) 5583-5588.

[23] K. Ghasemzadeh, S. Liguori, P. Morrone, A. Iulianelli, V. Piemonte, A.A. Babaluo, A. Basile, H_2 production by low pressure methanol steam reforming in a

dense Pd-Ag membrane reactor in concurrent flow configuration: experimental and modeling analysis, Int. J. Hydrogen En., 36 (2013) 16685-16697.

[24] S. Sá, H. Silva, Jose M. Sousa, A. Mendes, Hydrogen production by methanol reforming in a membrane reactor: palladium vs carbon molecular sieve membranes, J. Membrane Sci., 339 (2009) 160-170.

[25] A. Iulianelli, P. Ribeirinha, A. Mendes, A. Basile, Methanol steam reforming for hydrogen generation via conventional and membrane reactors: A review, Ren. Sust. En. Rev., 29 (2014) 355- 368.

[26] M.C.N. Amorim de Carvalho, F.B. Passos, M. Schmal, Quantification of metallic area of high dispersed copper on ZSM-5 catalyst by TPD of H2, Catal. Commun., 3 (2002) 503-509.

[27] G.F. Froment, K.B. Bischoff, Chemical Reactor Analysis and Design. Second ed. 1990, New York: Wiley.

[28] M. Muhler, L.P. Nielsen, E. Törnqvist, B.S. Clausen, H. Topsøe, Temperature-programmed desorption of H2 as a tool to determine metal surface areas of Cu catalysts. Catal. Letters, 14 (1992) 241-249.

[29] S.G. Sanches, J. Huertas Flores, R.R. de Avillez, M.I. Pais da Silva, Influence of preparation methods and Zr and Y promoters on Cu/ZnO catalysts used for methanol steam reforming, Intern. J. of Hydrogen Energy, 37 (2012) 6572-6579.

[30] L.-C. Wang, Y.-Mei Liu, M. Chen, Y. Cao, H.-Y. He, G.-S. Wu, W.-L. Dai, K.-N. Fan Production of hydrogen by steam reforming of methanol over Cu/ZnO catalysts prepared via a practical soft reactive grinding route based on dry oxalate-precursor synthesis, J. Catal., 246 (2007) 193-204.

[31] B.L. Kniep, F. Girgsdies, T. Ressler, Effect of precipitate aging on the microstructural characteristics of Cu/ZnO catalysts for methanol steam reforming, J. Catal., 236 (2005) 34-44.

[32] H. Zhang, J. Sun, V.L. Dagle, B. Halevi, A.K. Datye, Y. Wang, Influence of ZnO Facets on Pd/ZnO Catalysts for Methanol Steam Reforming, ACS Catal. 4 (2014) 2379-2386.

[33] M. Kurtz, N. Bauer, C. Buscher, H. Wilmer, O. Hinrinchen, R. Becker, S. Rabe, K. Merz, M. Driess, R.A. Fischer, M. Muhler, New Synthetic Routes to More Active Cu/ZnO Catalysts Used for Methanol Synthesis, Catal. Lett. 92 (2004) 49-52.

[34] C. Baltes, S. Vukojevic, D. Schuth, Correlations between synthesis, precursor, and catalyst structure and activity of a large set of CuO/ZnO/Al2O3 catalysts for methanol synthesis, J. Catal. 258 (2008) 334-344.

[35] S. Natesakhawat, J.W. Lekse, J.P. Baltrus, P.R. Ochodnicki, B.H. Howard, X. Deng, C. Matranga, Active Sites and Structure–Activity Relationships of Copper-Based Catalysts for Carbon Dioxide Hydrogenation to Methanol, ACS Catal., 2 (2012) 1667–1676.

[36] C. Pacholski, A. Kornowski, H. Weller, Self-Assembly of ZnO: From Nanodots to Nanorods, Angew. Chem. Int. Ed., 41 (2002) 1188-1191.

[37] O. Dulub, M. Batzill, U. Diebold, Growth of Copper on Single Crystalline ZnO: Surface Study of a Model Catalyst, Top. Catal., 36 (2005) 65-76.

[38] C. Wöll, The chemistry and physics of zinc oxide surfaces, Progress in Surf. Sci., 82 (2007) 55-120.

[39] C.T. Campbell, C.H.F. Peden, Oxygen Vacancies and Catalysis on Ceria Surfaces, Science, 309 (2005) 713-714.

[40] M.P. Hyman, V.M. Lebarbie, Y.W. Abhaya, K. Datye, J.M. Vohs, A Comparison of the Reactivity of Pd Supported on ZnO(1010) and ZnO(0001), J. Phys. Chem. C, 113 (2009) 7251-7259.

[41] B. Halevi, E.J. Peterson, A. DeLaRiva, E. Jeroro, V.M. Lebarbier, Y. Wang, J.M. Vohs, B. Kiefer, E. Kunkes, M. Havecker, M. Behrens, R. Schlögl, A.K. Datye, Aerosol-Derived Bimetallic Alloy Powders: Bridging the Gap, J. Phys. Chem. C, 114 (2010) 17181–17190.

[42] B. Halevi, E.J. Peterson, A. Roi, A. DeLaRiva, E. Jeroro, F. Gao, Y. Wang, J.M. Vohs, B. Kiefer, E. Kunkes, M. Havecker, M. Behrens, R. Schlögl, A.K. Datye, Catalytic reactivity of face centered cubic PdZnα for the steam reforming of methanol, J. Catal., 291 (2012) 44–54.

Chapter 4

The contributions of the author of this thesis in the following chapter are: performance of experimental work (e.g. synthesis of materials and catalytic tests), planning of characterization techniques performed under external collaboration. Dr. Katarzyna Eblagon is acknowledged for her significant contribution as first author of the presented chapter.

The in-situ XRD and CO chemisorption characterizations were conducted by Instituto de Tecnología Química (ITQ), in the Polytechnic University of Valencia (UPV) as part of the collaboration related to the European Project BeingEnergy (303476). TPR measurements were conducted by the Technical Research Centre of Finland (VTT) as part of the collaboration related to the European Project BeingEnergy (303476).

The author of this thesis had a percentual contribution as part of the research team of 10 %.

.

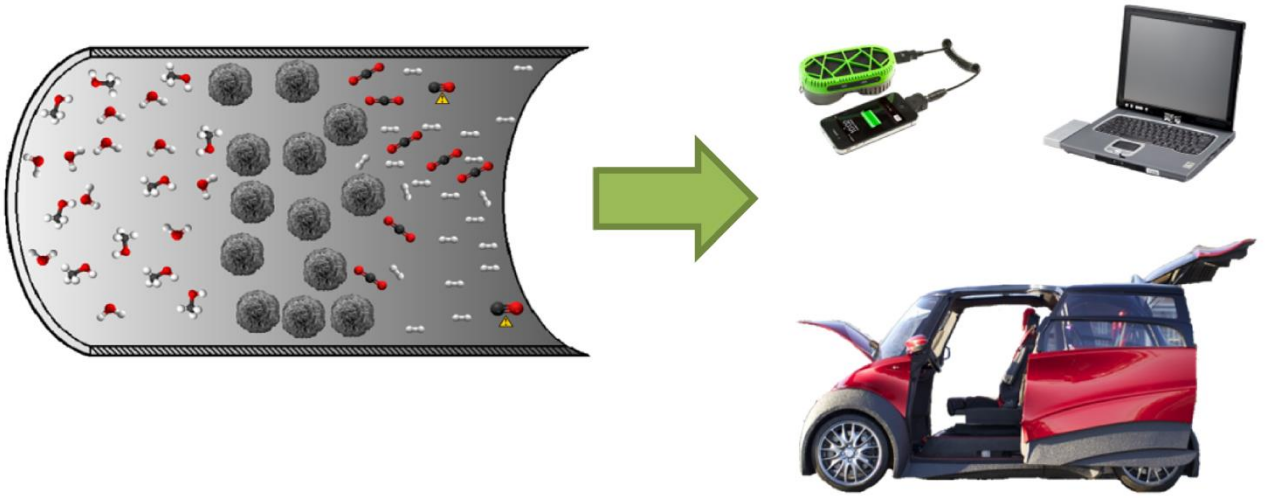

Chapter 4. Ultraselective low temperature steam reforming of methanol over PdZn/ZnO catalyst – Influence of induced support defects on catalytic performance[3]

Abstract

The influence of the calcination atmosphere of ZnO precursor ($Zn_4(CO)_3(OH)_6 \cdot H_2O$) on the catalytic performance of a series of PdZn/ZnO catalysts was studied for production of H_2 via low temperature (180 °C) direct methanol steam reforming (low temperature-MSR). The catalytic activity and selectivity of PdZn/ZnO were found to be strongly influenced by the calcination atmosphere of ZnO precursor and increased from oxidizing to reducing atmosphere, following the order (O_2< air< N_2< H_2). As a result, a very active catalyst was obtained by simply supporting Pd on ZnO calcined in H_2. Further evidence from XPS and TPR analysis indicated that calcination in reducing atmosphere gave rise to a significant increase in the concentration of oxygen vacancies on the surface of ZnO support. Thus, the superb performance of the best catalyst was attributed to the defect chemistry of ZnO support; mainly to the amount of oxygen vacancies present in the interface region, which act as additional active sites for water adsorption and subsequent activation. In addition, the formation of CO was drastically suppressed by replenishment of oxygen vacancies on ZnO support. Thus, it is clear that the abundance of specific active sites on PdZn/ZnO catalyst is strongly influenced by the preparation route of the ZnO support. Additionally, the PdZn alloy was discovered to be unstable under prolonged exposure to CO atmosphere and the stability test under methanol steam reforming conditions showed a 24% drop in conversion over 48 h testing period. This phenomena can have detrimental effect on the performance of this type of catalytic systems in continuous prolonged duty cycle time on-stream.

[3] K. M. Eblagon, P. H. Concepción, H. Silva, and A. Mendes, Ultraselective low temperature steam reforming of methanol over PdZn/ZnO catalysts—Influence of induced support defects on catalytic performance. Appl. Catal. B Environ. 154–155 (2014) 316–328

4.1. Introduction

Hydrogen will surely contribute to the world energy market in the mid-term to long-term future [1, 2]. However, one of the major obstacles of "Hydrogen Economy" is finding a feasible method to store and distribute sufficient amount of hydrogen mainly for transportation sector [3]. Recently, reformers that can extract hydrogen from fuels gained increased research interest due to the fact that they can be integrated directly with polymer electrolyte fuel cell (PEMFC). As a result, high purity H_2 can be produced *in situ* on board of the vehicle via well-established steam reforming of alcohols from biomass, or hydrocarbons [4]. In this regard, methanol is a promising hydrogen carrier candidate for the future [5] mainly because it has high H to C ratio, low chemical energy bond [6] and can be produced either by reduction CO_2 or from diverse bio-based resources [7].

Methanol steam reforming (MSR) is accompanied with side-reactions such as: methanol decomposition (MD), water gas shift (WGS) and reversed water gas shift (RWGS) [8, 9]. The extent of these processes depends on the feed composition, reaction conditions and the catalyst used. Due to MD and RWGS reactions being always present, the reformate gas inevitably contains CO contaminant which even in trace levels can poison the PEMFC anode [2, 10]. For example, high temperature PEMFC (HT-PEMFC) using polybenzimidazole membranes working at 180 °C can only tolerate a maximum of 1–2% CO in the anode feed [11]. One approach to decrease the amount of produced CO is to lower the temperature of MSR to the point at which MD is suppressed and WGS reaction is favoured due to the thermodynamics of these processes [9]. A catalyst able to work efficiently at lower temperatures is also cost-effective and desirable taking into consideration the integration between the endothermic MSR and exothermic PEMFC operation. Furthermore, low operating temperatures are beneficial for applications as power supplies for small portable devices, where heat and space management are of primary concern [12]. However, the development of a suitable catalytic system promoting both endothermic MSR and exothermic WGS at reasonably low temperatures (below 200 °C) remains a challenge.

Cu based catalysts are typically used for MSR due to their relatively low cost, very high activity and low CO production at temperatures below 300 °C [13]. Thus, several catalyst formulations were studied, such as binary compositions; Cu/ZnO, Cu/SiO_2, Cu/CeO_2 [4], commercially based $Cu/ZnO/\gamma\text{-}Al_2O_3$ and its variations with added promoters; $Cu/ZrO_2/\gamma\text{-}Al_2O_3$, $Cu/Cr/\gamma\text{-}Al_2O_3$ [2] or $CuTiP/\gamma\text{-}Al_2O_3$ [6]. More recently CuZnGaOx [12] and CuZn catalyst promoted by rare earth metals such as Tb and Pr [14] were reported to have high activity at low temperature MSR. Nevertheless, Cu based catalysts have some considerable drawbacks which include pyrophoricity and easy deactivation due to thermal instability [7, 15] or coke formation [13]. Additionally, these catalysts are sensitive towards condensing steam [6], which results in declining activity and mechanical integrity of the catalytic system under duty cycle conditions [11].The search for a more suitable catalyst for MSR has led to a discovery that the inherent high selectivity of Pd catalyst towards MD can be drastically switched to high selectivity in MSR by simply changing the material of the support [16]. Apparently, Pd supported on hard-to-reduce oxides M_xO_y (M= Si, Al, Mg, Zr, Pr, Ce, La) is highly selective to MD [17, 18]. On the other hand, Pd supported on easily reducible oxides such as ZnO, Ga_2O_3 or In_2O_3 becomes active and selective in MSR. Unusual behaviour of these Pd based catalysts was attributed to a formation of alloys PdMe (Me = Zn, Ga, In) upon proper reductive pre-treatment, leading to a bifunctional synergism between intermetallic and oxide species which is necessary for a good catalytic performance in MSR [19, 20]. In addition, the *in situ* partial oxidation of PdZn nanoparticles was observed recently to result in the formation of a large interface between the intermetallic PdZn and small ZnO patches, which improved the selectivity to CO_2 in MSR [20]. It is thus evident that the performance of Pd/ZnO catalyst is not only dependent on the chemical composition or size of the active species, but it is also governed by the type of active sites present on its surface [21]. Moreover, there was an indication that addition of Zn to Pt or Pd altered the barriers for C–H cleavage and thus changed the stability of various intermediates in MSR [22]. The PdZn/ZnO interface was found to increase water activation at lower temperatures, therefore promoting CO_2 selectivity [23]. However, the role of ZnO in the performance of PdZn/ZnO is not yet fully understood.

ZnO is an anisotropic oxide which contains intrinsically unstable polar facets with point defects that compensate for a surface dipole moment and non-polar facets which exhibit densely packed Zn and O atoms that are electrically neutral [24]. In addition, stronger electronic interaction and facile PdZn alloy formation was reported on Pd supported on ZnO with majority of polar facets exposed on the surface. Furthermore, it was shown previously that the exposure of ZnO to atmospheric pressure of H_2, can change the concentration of the Schottky defects mainly that of oxygen vacancies [25]. In addition, the creation of defects through reduction modifies the d-band states of a reducible metal oxide (such as ZnO) which changes the interaction with the adsorbates [26]. As a result, it can be expected that the increased concentration of oxygen vacancies in ZnO support might improve the performance of the PdZn/ZnO catalyst at low temperature MSR. With this regard, the present work will be focused on the performance of PdZn alloys supported on the ZnO calcined in N_2, O_2, air and H_2 in low temperature MSR. The catalytic results will be compared to the performance of PdZn supported on commercial ZnO (Sigma–Aldrich). The aim is to provide an insight into the influence of the active sites present on the surface of ZnO support on the activity and selectivity of the PdZn/ZnO catalytic system. Moreover, thorough catalyst characterization was carried out to gain a better understanding of the key parameters controlling the performance of PdZn/ZnO catalysts for low temperature MSR. Thus, the extent of synergetic interaction between PdZn and various ZnO was studied using analytical techniques such as X-ray Diffraction (XRD), Temperature Programmed Reduction (TPR) and X-ray Photoelectron Spectroscopy (XPS). Selected catalysts and ZnO supports were additionally characterised by high resolution transmission electron microscopy (HRTEM) and scanning electron microscopy–energy dispersive X-ray spectroscopy (SEM-EDX). The active sites and the stability of PdZn/ZnO catalysts was characterised by CO absorption IR DRIFT spectroscopy. Finally, the stability test of the most active catalyst was carried out to access its long term performance under prolonged exposure to methanol steam reforming conditions.

4.2. Experimental

4.2.1. Hydrothermal method of ZnO preparation

All the reagents were purchased from Sigma–Aldrich and were used without any pretreatment. The ZnO supports were obtained following a conventional hydrothermal synthesis [27]. $Zn(CH_3COO)_2$ was used as a Zn^{2+} precursor, $CO(NH_2)_2$ as precipitant and P123 Pluronic block copolymer as a surfactant. In a typical hydrothermal synthesis; 1.1 g of $Zn(CH_3COO)_2$, 6 g of urea and 3 g of P123 were dissolved in 100 mL of distilled water. Subsequently, the pH of the solution was fixed at 5.0 using CH_3COOH and the mixture was left to homogenize at ambient conditions for 2 h. After a homogenous mixture was obtained, the solution was sealed in a hydrothermal teflon lined reactor and heated in a laboratory oven at 90 °C for 24 h to ensure the complete precipitation of zinc carbonate. Subsequently, the obtained solid product was filtered and washed several times with distilled water and dried overnight at 90 °C in air in an oven. The final step of the preparation of ZnO supports was the calcination of the prepared precursor at 370°C, with a heating rate of 4.2 °C/min in a flow (200 mL/min) of a selected gas (H_2, O_2, air, N_2) and with a dwell time of 0.5 h. The prepared ZnO supports are hereafter referred as: ZnO_H_2 – ZnO calcined in H_2; ZnO_N_2 – ZnO calcined in N_2. ZnO_COM is a ZnO commercial support (Sigma–Aldrich), etc.

4.2.2. Synthesis of PdZn/ZnO catalysts

The 4.7 wt.% PdZn/ZnO catalysts were prepared following a standard wet impregnation technique, using hydrothermally prepared ZnO supports (Section 4.2.1) and ZnO commercial support (Sigma–Aldrich, ZnO nanopowder) for comparison. In a typical procedure, the appropriate amount of ZnO support was wetted by 10 mL of chloroform to prepare a slurry. Subsequently, a solution of a calculated amount of palladium acetate (Sigma–Aldrich, reagent grade 98%) in 5 mL of chloroform was added dropwise to the slurry of the ZnO support under vigorous ultrasonic treatment.

The solvent was then dried out at ambient conditions under continuous magnetic stirring while placed in a fume hood. PdZn alloy formation is necessary to obtain good catalytic activities in MSR, thus the catalyst reduction temperature was optimized by monitoring various reduction temperatures using an on-line XRD technique. The optimum temperature of PdZn alloy formation was chosen at 400 °C in H_2 flow (200 mL/min), with a heating rate of 4.2 °C/min and a dwell time of 2 h.

4.2.3. Physicochemical characterization of supports and catalyst

The physicochemical properties of ZnO supports were characterised using a variety of methods. The morphology and qualitative composition was obtained from SEM images and EDX, respectively. The SEM micrographs were recorded using a high resolution (Schottky) environmental scanning electron microscope with X-ray microanalysis and backscattered electron diffraction pattern analysis working at 20 kV. Shape and sizes of the particles were obtained using image analysis software (ImageJ). The average diameter of the ZnO assemblies was obtained measuring at least 100 particles from three different regions of each of the samples. The composition of the supports was studied at a magnification of about 600k. Four different areas of each of the samples were examined by EDX analysis with working distance set at 25 mm, dead time 50% and a process time of 6 min.

The crystallographic characterisation of ZnO supports was obtained using the XRD technique. The XRD pattern of the selected samples was collected using a Philips PW1729 diffractometer operating in Bragg-Brentano focusing geometry and using Cu Kα radiation at wavelengths Cu $K\alpha_1$ = 154.06 pm and Cu $K\alpha_2$ = 154.439 pm. The data was collected at 2θ angles (20–70°), with a step size of 0.02°, step speed of 0.5°/min and at 1.25 s per step. The obtained X-ray scans were compared to those of standard database and the phases were assigned comparing the data available in literature.

BET surface area of ZnO supports was measured following a standard procedure, obtaining N_2 11 point adsorption isotherms at 77 K. Prior to the measurements, the samples were outgassed in vacuum at 300 °C for 2 h.

The neat ZnO supports and as-prepared PdZn/ZnO catalysts were characterised using a TEM CM 20 (accelerating voltage 310 and 208 kV at nominal magnification) and a HRTEM JEOL 2010 (accelerating voltage 600 kV, at nominal magnification 590 kV). For determination of a particle size distribution, not less than 100 particles from different areas of the sample were measured, using the Scandium software from Olympus Soft Imaging Solutions. The determination of the lattice d-spacing was carried out using high resolution micrographs of the lattice, taking at least five measurements from different areas of the sample. The estimated error of the measurements was ±0.01 nm.

The interaction between metal and support in PdZn/ZnO calcined at various atmospheres was probed using X-ray photoelectron spectroscopy (XPS). The XPS analysis was performed using a Kratos AXIS Ultra HSA, with VISION software for data acquisition and CASAXPS and XPS Peak 41 software for data analysis. The analysis was carried out with a monochromatic Al Kα X-ray source (1486.7 eV), operating at 15 kV (90 W), in FAT mode (Fixed Analyser Transmission), with a pass energy of 40 eV for regions ROI and 80 eV for survey. Data acquisition was performed with a pressure lower than 1.0×10^{-6} Pa using a charge neutralisation system. The modelling of the spectra was performed using peak fitting with Gaussian–Lorentzian (80%) peak shape and Shirley type background subtraction.

The TPR-curves were measured using a quartz flow-through apparatus. Consumption of H_2 was obtained using a Balzers GAM-415 quadrupole mass spectrometer. Hydrogen response was calibrated by pulsing 1 mL of 3% H_2 in argon and measuring the corresponding response. TPR-conditions: H_2/Ar (3 vol%),flow 20 mL/min, heating rate 3 °C/min in the temperature range 30–600 °C.

The nature of the Pd species and the type of active sites present in the prepared PdZn/ZnO catalysts was further characterised by CO-chemisorption IR-DRIFT analysis. The IR-DRIFT analysis was carried out using powder catalyst. The spectra

of adsorbed CO were recorded at room temperature (25 °C) with a Nexus 8700 FTIR spectrometer using a DTGS detector with 4 cm^{-1} resolution. An IR cell allowing *in situ* treatments under controlled gas atmosphere and temperature was connected to a vacuum system with gas dosing facility. For IR studies the samples were pressed into self-supported wafers and diluted in ZnO (Sigma–Aldrich) using previously optimised weight ratios. The samples were treated at 300 °C in a 5% H_2 in N_2 flow (15 mL/min) for 2 h followed by evacuation at 10^{-4} mbar at 350 °C for 1 h. After the activation procedure, the samples were cooled down to 25 °C under dynamic vacuum conditions followed by CO dosing at increasing pressure (0.4–15 mbar). Several IR-DRIFT spectra were recorded with increasing exposure time, until no further changes were observed in the spectra indicating full CO saturation of the surface.

The amount of Pd in the samples was determined with an ICP-OES (Vista RL, Varian) after matrix-matched calibration. Not more than 5 mg of the sample was dissolved in 2 mL of aqua regia. Finally, the solutions were diluted in 50 mL volumetric flasks and the analysis was carried out.

The number of surface Pd sites was quantified by CO pulse chemisorption experiments which were conducted using a Micromeritics AutoChem II 2920 analyzer. Catalysts (typically 0.3–0.5 g) were loaded in a quartz tube that was placed in the built-in furnace. The temperature in the catalyst layer was controlled using a type-K thermocouple and the flow of gasses was regulated by a built-in mass flow controllers. The catalysts were typically purged with dry helium at 100 °C for 1 h, followed by reduction in 5% H_2/Ar (flow rate 50 mL/min) at 400 °C for 2 h and then it was cooled down to 50 °C. Subsequently, the cleaned sample was exposed to pulses of 0.5 mL CO until five consecutive pulses yielded identical signal areas. The dispersion of Pd was estimated from the ratio of the number of moles of surface Pd atoms to the total number of moles of Pd atoms present in the catalyst.

4.2.4. Catalytic tests

The catalytic activity tests of MSR were performed in a fixed bed reactor at pressures between 1 and 1.6 bar, with the following experimental conditions: steam/methanol molar ratio of 1.5 and a contact time of W/F_0 = 83 kg mol^{-1}s (where W is the mass of the catalyst, 200 mg and F_0 is the flow rate of methanol). The stainless steel microreactor was placed in an electrically heated furnace and the temperature was controlled inside the furnace as well as in the catalytic bed using a K-type thermocouple inserted into the catalytic bed. Argon was used as carrier gas and the flow of reactants was controlled by mass flow meters and the gas products were analysed by an online mass spectrometer. The concentration of CO (ppm) in the products was measured directly using an on-line CO analyser (reading error ± 2 ppm). An average of at least 10 measurements was taken to reduce the reading error. Prior to the catalytic test, the catalyst was pre-treated *in situ* for 2 h by heating up to 200 °C in a stream of Ar (30 mL/min). Subsequently, the hydrogen gas was switched on and the final stream consisted of 70% H_2/Ar. Finally, the catalyst was cooled down to 180 °C and the reaction mixture was introduced. An average of four measurements spaced by 15 min was taken to assure that a stable state of the catalyst performance was reached.

4.3. Results and discussion

4.3.1. Structural and Surface Characterisation of ZnO supports

The hydrothermally prepared ZnO supports showed significantly higher values of BET surface area in comparison to ZnO_COM. The BET surface area results are gathered in Table 4.1. Within in-house made samples, higher surface areas were obtained for ZnO supports calcined in oxidative atmospheres. Larger BET surface area after calcination in air/O_2 than in N_2 were previously observed in case of other oxides [28].

Table 4.1 - The physicochemical characterization of the ZnO supports studied**.**

Sample	BET surface area (m^2/g)	Ratio (100)/(002)
ZnO_O_2	88	1.59
ZnO_air	76	1.56
ZnO_N_2	27	1.13
ZnO_H_2	24	1.3
PdZn_ZnO_COM	16	1.2

The difference in the surface area obtained with different calcination atmospheres can be linked to the changes in mechanism of thermal decomposition of the precursor with the surrounding atmosphere, where the presence of oxygen increases the formation of highly porous structures due to additional burn out of the material.

The representative XRD patterns of the precursor and ZnO supports studied are shown in Figure 4.1. The XRD peaks of the solid samples before calcination were characteristic of $Zn_4(CO)_3(OH)_6 \cdot H_2O$ (JCPDS Card No.11-0287). After calcination, the diffraction peaks in the pattern (see Figure 4.1) were indexed to the hexagonal (wurtzite) ZnO phase (Joint Committee on Power Diffraction Standards card 36-1451). The diffraction peaks at 2θ of 31.5°, 34.2°, 36.0°, 47.3°, 56.4°, 62.6°, 65.6°, 67.7°, 68.8° were ascribed to the diffractions from the following ZnO planes: (100), (002), (101), (102), (110), (103), (200), (112) and (201) [29], respectively.

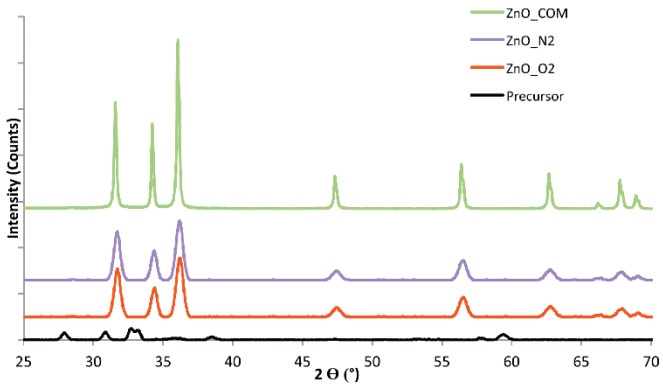

Figure 4.1 - XRD pattern of $Zn_4CO_3(OH)_6 \cdot H_2O$ (precursor), ZnO calcined in N_2 (ZnO_N_2), ZnO calcined in O_2 (ZnO_O_2) and ZnO commercial (ZnO_COM).

It is noted that the XRD patterns for all of the synthesized ZnO supports closely resembled that of bulk ZnO (Zn_COM), regardless the type of gas used during calcination step. However, a typical diffraction peak broadening related to the actual size of the crystallites in a direction normal to the diffracting plane was observed in case of the hydrothermally prepared ZnO supports. This broadening together with a small shift towards higher 2θ values can be a result of the difference in shape of these crystallites as compared to the ZnO_COM [25].

The reactions of Brønsted acids such as methanol are structurally dependent reactions [30] and more active PdZn catalysts were previously obtained when PdZn was supported on ZnO with (002) polar facets exposed [31]. With regards to these findings, the anisotropy of the ZnO supports studied in the present work was compared using the relative ratio of intensity of XRD diffraction peaks of non-polar to polar facet (100)/(002), according to the method proposed by Tsang *et al*. [32]. Thus, a lower relative ratio of (100)/(002) suggests higher exposure of polar planes, whereas a higher ratio of (100)/(002) suggests growing of the crystal along the c-axis [0001] direction and a high proportion of non-polar facets. The obtained (100)/(002) XRD ratios for ZnO supports are compared in Table 4.1. As it can be seen from these results, the ratio of relative peak intensities of the studied supports was in the range of 1.13–1.59. It is noted that this is rather small variation, which indicates only small differences in the amount of exposed polar facets among these ZnO supports. As a matter of fact, the aspect ratio of these ZnO supports is very similar. The ratio (100)/(002) obtained for commercial ZnO was 1.2 which agrees well with the reported values [32]. Thus, the lowest exposure of polar facets was obtained in the samples calcined in oxidative atmospheres, as it can be seen in Table 4.1. The representative HRTEM images of ZnO_H_2 and ZnO_COM are shown in Figure 4.2.

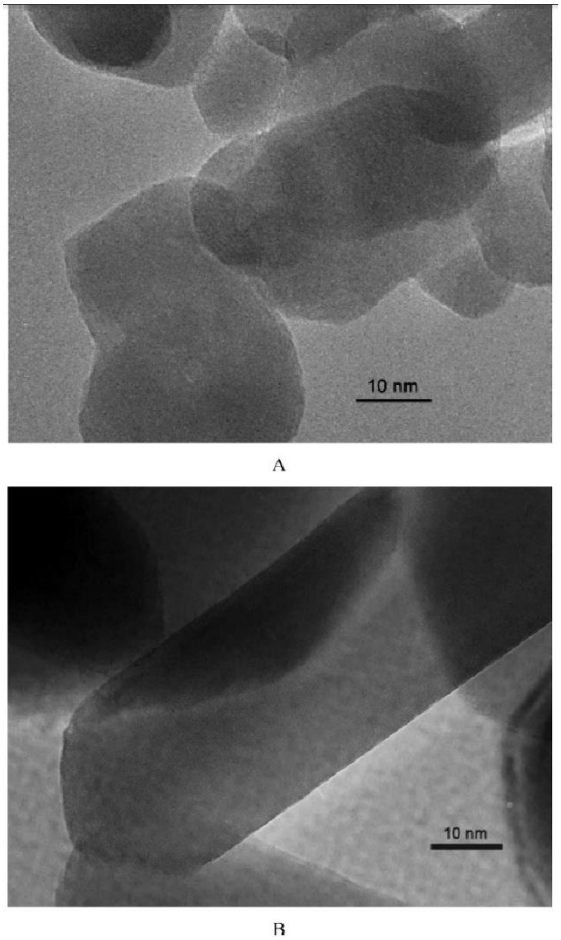

Figure 4.2 - HRTEM micrographs of A) ZnO_H_2 and B) ZnO_COM.

The morphology of the obtained ZnO supports calcined at various atmospheres was additionally examined by SEM and the resulting micrographs are shown in Figure 4.3 together with the related particle size distributions. In general, low magnification images of the ZnO supports, regardless of the calcination atmosphere, showed mostly uniform spherical particles with diameters in the micron range. However, careful examination disclosed that the morphology of ZnO was strongly affected by the type of gas used during calcination step.

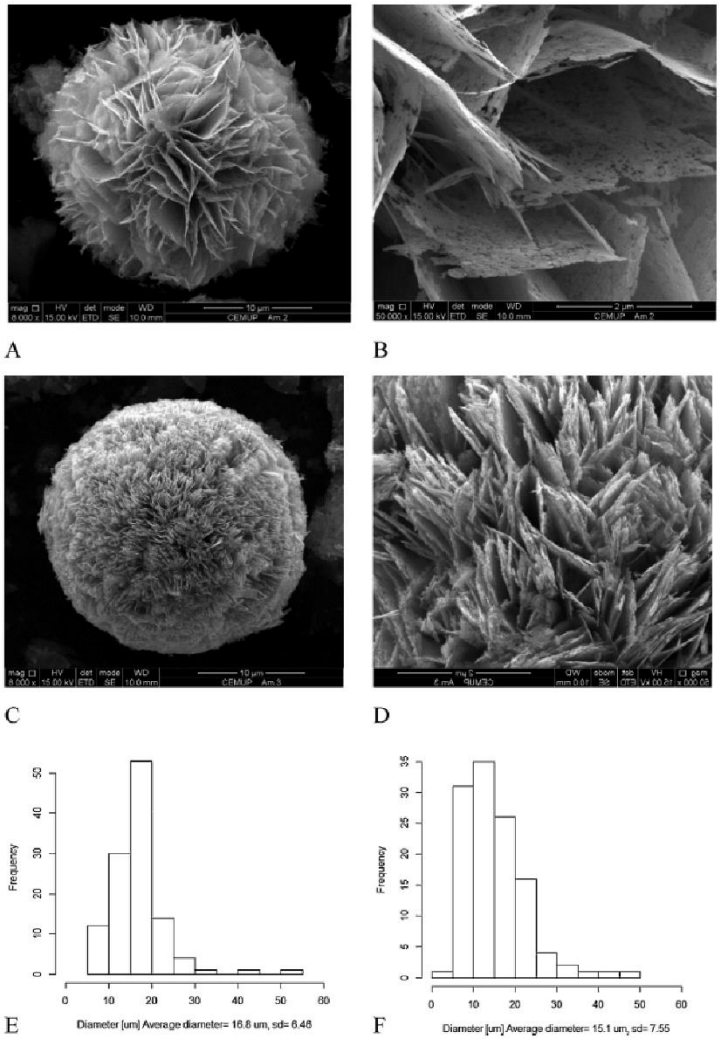

Figure 4.3 - SEM images of the ZnO particles prepared by calcination in different atmospheres. A) ZnO_O_2; B) close-up of ZnO_O_2; C) ZnO_H_2; D) close-up of ZnO_H_2; E) particle size distribution of ZnO_O_2 and F) particle size distribution of ZnO_H_2.

A closer look at a single particle showed that the ZnO_O2 support (see Figure 4.3A and B) contained mostly round flower-like self-assemblies of thin highly porous nanosheets with a mean diameter of 16.8 μm. The magnified SEM image of the same sample revealed that the nanosheets were self-assembled leaving large voids between each other. In addition, the structure of the nanosheets contained very disordered multiple pores. Thus, high potential for adsorption of gaseous reactants

could be anticipated on these ZnO supports due to the structure of the composing nanosheets. The coarse structure of these nanosheets can be attributed to a fast water removal from the precursor. Similar nanoflower assemblies of ZnO were obtained in hydrothermal synthesis and calcination in air [33]. On the contrary, highly magnified SEM images of ZnO_H_2 sample (Figure 4.3C and D) revealed that the microspheres in this case were constructed by highly ordered and very short multilayer nanosheets that were closely packed together to form a nanoball-like porous structure. In addition, in ZnO_H_2 support, the nanosheets were thicker (60 nm in width) as compared to nanosheets of ZnO_O_2. The mean particle size of ZnO_H_2 (see Figure 4.3F) was 15.1 μm, which taking into consideration the standard deviation is very similar to the size of the particles of ZnO_O_2. The morphology of sample ZnO_N_2 closely resembled that of ZnO_H_2 with a mean particle size of 13.1 μm. On the other hand, the morphology of ZnO_air strongly resembled that of ZnO_O_2, with a mean particle diameter of 15.7 μm. Therefore, in general, it can be concluded that calcination of zinc carbonate dihydrate precursor in oxidizing atmospheres (O_2, air) results in the nanospheres/nanoflowers assemblies consisting of a flower-like structure. This structure was constructed from highly porous long nanosheets that were joined together incorporating big voids between them. Such morphology resulted in a higher specific surface area. On the other hand, if the calcination was done in a reductive or inert atmosphere (H_2 or N_2) the spherical nanoballs were produced with short and densely packed nanosheets. These ZnO nanoballs had lower BET surface area than the ZnO supports calcined in oxidizing atmospheres. On the other hand, the size of ZnO particles obtained by hydrothermal method was very similar, regardless of the calcination atmosphere used. In comparison, ZnO_COM had faceted crystallites that had prevalent morphology of nanorods with approximate dimensions of 80–100 nm in length and 20 nm in width (results not shown) and a very low BET surface area (listed in Table 4.1). Thus, in spite of the similar aspect ratio and polarity, the morphologies of the studied ZnO supports significantly differed from each other. Noteworthy, EDX analysis of the synthesized ZnO supports and ZnO_COM agreed well with the XRD results and showed neat ZnO phases without any impurities.

4.3.2. Physicochemical Characterisation of PdZn/ZnO catalyst

It was considered of interest to study the possible influence of the morphology of ZnO support on the onset temperature of PdZn alloy formation. Thus, the reduction of selected samples was followed by on-line XRD measurements in the temperature range (30–400 °C) and the formation of PdZn alloy was confirmed in all cases, regardless of the type of ZnO support present. The representative XRD pattern of PdZn/ZnO_COM is shown in Figure 4.4. In all studied supports, only a very broad peak in the region of $2\theta = 40.2°$ belonging to Pd^0 was observed up to 250 °C, which indicates a small particle size. However, this diffraction peak clearly disappears at higher reduction temperatures. It is thus possible that the amount of remaining Pd^0 is below detection limit of the XRD technique, or that the formation of PdZn alloy was completed. As evidenced in Figure 4.4, the beginning of alloy formation took place at around 300 °C, which was accompanied by the appearance of the diffraction peaks at $2\theta = 41°$ and 43.9° that are close to the values ascribed to PdZn alloy [34]. Upon further heating, the crystallinity and particle size of PdZn alloy increased, which was represented by narrowing of these peaks. Similar patterns were obtained for the samples supported on ZnO calcined in H_2, O_2, air and N_2. Based on these results, 400 °C was selected in the present work as an optimum reduction temperature. Overall it was concluded that the onset of PdZn alloy formation was not affected by the morphology of the ZnO support.

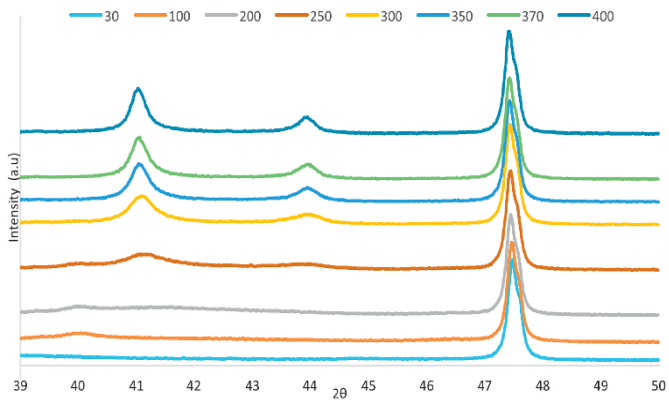

Figure 4.4 - XRD pattern obtained during reduction of PdZn_ZnO_COM at various temperatures (°C). Large peak at 2θ = 47.7°is ascribed to ZnO (102) plane [29].

Lattice fringes of 0.28 nm were measured from HRTEM micrographs for ZnO_O_2, ZnO_H_2 and ZnO_COM which can be attributed to the exposure of a ZnO non-polar (100) plane [29] which is in agreement with the XRD findings. The formation of PdZn alloy under reduction atmosphere in all of the samples was also further supported by the lattice spacing measurements from HRTEM micrographs. A representative HRTEM image of PdZn_ZnO_H_2 is shown in Figure 4.5.

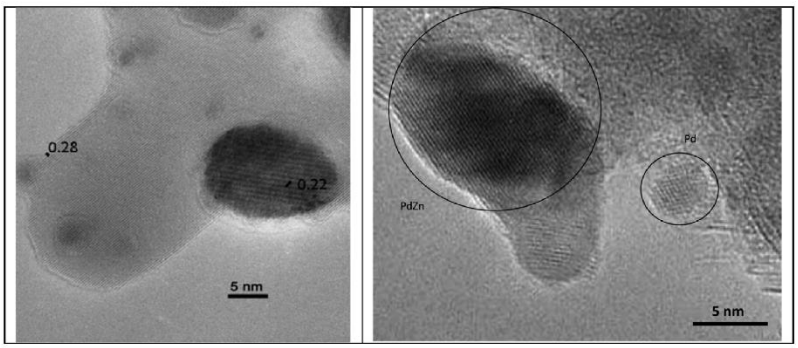

Figure 4.5 - Left: HRTEM image of a single polycrystalline PdZn particle supported on ZnO_H_2. The lattice fringes of PdZn (101) and ZnO (100) are marked. Right: HRTEM image of single PdZn and Pd particles supported on ZnO_COM.

As it can be seen in Figure 4.5 left, a lattice spacing of 0.22 nm was obtained for the nanoparticle, which matches the value reported for PdZn alloy (111) [35]. It should be noted, that the lattice fringes of the particles in the range of 3-4 nm were easily obtained, however measuring d-spacings of smaller particles also present in the samples was difficult due to the contrast from the support. Therefore, we have examined more closely selected area of sample PdZn_ZnO_COM (see Figure 4.5, left) that contained the highest average particle size. The image revealed the lattice spacing of the smaller particle (on the left side of Figure 4.5) to be 0.23 nm. This result can suggest the presence of Pd (111), which possesses lattice spacing slightly higher as compared to that of PdZn alloy in accordance with literature findings [35]. It should be underlined that due to the difference in lattice spacing between PdZn and Pd being not more than 3% [35], the phase of these small particles in our case could only be conclusively identified as Pd by joined results from HRTEM, TPR, XPS and CO adsorption-DRIFT analysis described later in this work. A representative lower magnification HRTEM image of the same sample together with the corresponding particle size distribution is shown in Figure 4.6. Similarly to these results, the HRTEM analysis of the remaining PdZn/ZnO catalysts, showed finely dispersed particles with no visible agglomeration, regardless of the calcination atmosphere of ZnO precursor. The mean diameters obtained from HRTEM images of PdZn supported on hydrothermally synthesized ZnO were in the range of 2.1 nm to 3.4 nm, which is significantly lower than the mean diameter of the PdZn supported on ZnO_COM (8.8 nm). The sizes of the particles are gathered in Table 4.2. A clear influence of the morphology of ZnO support was observed on the crystallization of PdZn alloy, leading to changes in size of the nanoparticles. In general, smaller particles would be expected on the higher surface area supports, mainly due to higher Pd dispersion and thus longer diffusion distances between neighboring PdZn and decreased sintering of these particles. Nevertheless, no clear trend was observed between the particle size and the surface area of ZnO support in the studied catalysts.

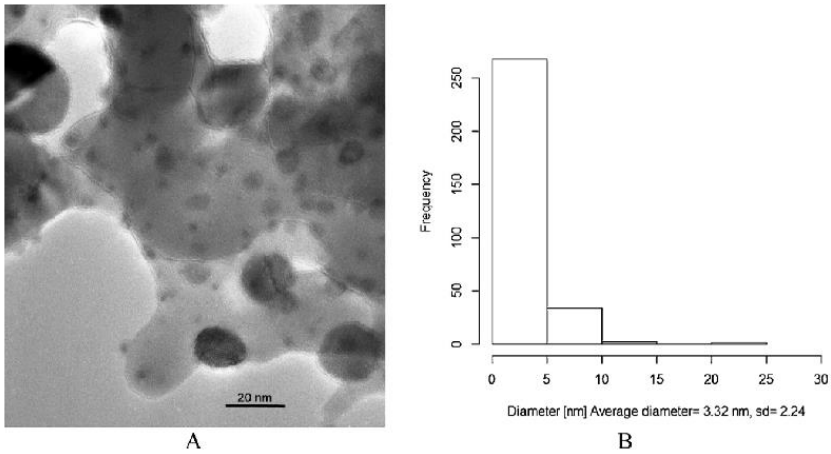

Figure 4.6 - (A) HRTEM image of PdZn/ZnO_H_2. (B) Particle size distribution of the same sample.

Table 4.2 - Catalytic performance of a series of PdZn/ZnO catalyst in low temperature MSR together with corresponding particle size measured from HRTEM images.

Sample	Activity ($\mu mol/g_{met} \cdot s$)	CO concentration (ppm)	HRTEM particle size (nm)
PdZn_FEUP_O_2	42.6	1450	3.3
PdZn_FEUP_air	46.8	1400	2.4
PdZn_FEUP_N_2	63.8	700	2.1
PdZn_FEUP_H_2	**87.9**	**146**	**3.3**
PdZn_ZnO_COM	38.3	309	8.1

4.3.3. Methanol Steam Reforming

A good catalyst for low temperature MSR should provide high water and methanol conversions to hydrogen and carbon dioxide while minimising occurrence of any side-reactions. The prepared PdZn alloyed catalysts immobilized on ZnO calcined under various atmospheres were tested for activity and selectivity in MSR at 180 °C using an in-house built MSR set-up as described in the Experimental section. The results of the catalytic activity and selectivity expressed by CO concentration in ppm, are gathered in Table 4.2 and compared to PdZn alloy supported on ZnO_COM. The BET surface area of ZnO supports and their polarity can be found in Table 4.1.It was rather surprising to find that the catalytic activity was independent from the BET surface area of ZnO support (compare Table 4.1 with Table 4.2),

which is in contrast with the literature reports [27]. On the other hand, selectivity to CO was higher for PdZn catalysts supported on higher surface area ZnO, which were calcined in oxidizing atmosphere. This result can be associated with the apparently lower reducibility of high surface area ZnO supports. Moreover, the selectivity to CO was found to be inversely proportional to the activity for the PdZn supported on hydrothermally obtained ZnO supports (excluding PdZn/ZnO_COM). Lower selectivity to CO was achieved by PdZn supported on ZnO with higher exposure of polar facets which is in agreement with the literature [25]. However, no direct trend was established between increased polarity of ZnO and activity of the PdZn/ZnO catalysts, which can be explained by the fact that the range of the polarities studied was very narrow. Additionally, smaller PdZn alloy particles obtained on hydrothermally produced ZnO displayed better activity per gram of metal than their bigger counterparts supported on ZnO_COM. However, in order to account for the particle size differences between PdZn_ZnO_H_2 and PdZn_ZnO_COM, the TOF of these samples was compared and the results are gathered in the supplementary material. The amount of active sites was obtained by CO pulse chemisorption taking into consideration the similar amount of PdZn alloy present on the surface of these catalysts, as showed later in the paragraph describing XPS results of the present work. Similar extent of alloy present is essential in case of this comparison, because the presence of Zn in Pd decreases the amount of chemisorbed CO and therefore alters the Pd:CO stoichiometry, leading to false number of measured active sites on the catalyst [46]. The TOF of PdZn_ZnO_H_2 was 1.01 s^{-1} and that of PdZn_ZnO_COM was 0.71 s^{-1}, which is in the range of the values reported in the literature for similar systems [16]. These results show that independently of the particle size, the most active catalyst was obtained by supporting PdZn on ZnO calcined in reductive atmosphere.

Nevertheless, the greatest differences in performance could be assigned to differences in calcination atmosphere of ZnO precursor (H_2, O_2, N_2, air). As it can be clearly seen in Table 4.2, the activity of PdZn/ZnO catalysts increased with calcination atmosphere from oxidative (O_2) to reducing (H_2). It should be underlined that over twofold increase in activity was achieved by supporting PdZn on ZnO_H_2 as compared to ZnO_O_2. Moreover, the selectivity to CO dropped significantly on

the PdZn supported on ZnO calcined in N_2 and H_2 as compared to PdZn supported on ZnO calcined in oxidative atmospheres. The decrease in CO production can be a result of more efficient water activation in these supports, prerequisite for CO_2 selective catalyst in MSR [24]. Overall, the anticipated exceptional increase in activity and selectivity of PdZn supported on ZnO calcined in H_2 atmosphere can be associated with the presence of different active sites, mainly oxygen defects on the surface of the support of this catalyst, which alter the adsorption process of substrates and intermediates during low temperature MSR. It is clear that the difference in catalytic performance as a result of the calcination atmosphere of ZnO showed cannot be attributed to a difference in particle size of the PdZn alloy, as virtually the same particle sizes were obtained in this family of catalysts, regardless of the calcination atmosphere of ZnO. As it was mentioned before, significantly higher size of PdZn particles was noted on the ZnO_COM, which can be attributed to the difference in morphology of the ZnO support.

Oxygen vacancies present on the surface of an oxide catalyst are important for several catalytic reactions [31]. However, generally the amount of oxygen vacancies is expected to be higher in ZnO with higher exposure of polar facets, because they are formed to counterbalance the large surface dipole moment [24]. The vacancies can also be created on the non-polar facets of the crystal by treatment in reductive atmosphere, given the right reaction conditions. Much higher conductivity has been previously reported for ZnO materials calcined in oxygen poor atmospheres, which was attributed to a reversible removal of the oxygen atoms from the ZnO lattice and releasing free carriers [37]. Thus, it is likely that the outstanding performance of the PdZn/ZnO_H_2 catalyst in the present work is a result of a higher concentration of oxygen vacancies that are produced according to Eq. (4.1) [37], even though the exposure of polar facets on this support is not the highest in this work (see Table 4.1)

$$2O_i^{2-} \rightleftarrows O_2 + 4e^- \qquad \text{Eq. (4.1)}$$

These oxygen defects in ZnO create additional active sites to the ones existing on PdZn and on PdZn/ZnO interface, which are responsible for water adsorption. Such a synergy drastically increases the activity of the catalysts at low temperature MSR. Additionally, the improved water activation increases the selectivity towards CO_2 by

decreasing the activity of PdZn/ZnO in MD. On the other hand, when the ZnO precursor is calcined in oxidative atmospheres, the surplus oxygen is able to enter the interstitial sites of ZnO and push the interstitial oxygen atoms back into the lattice, or fill in the existent oxygen vacancies. Thus the amount of $VO–O_i$ pairs formed decreases. As a result, less available active sites are present on the surface of ZnO leading to poorer catalytic performance. Noteworthy, further evidence had to be obtained to support this speculation.

4.3.4. XPS study of Oxigen vacancies in ZnO supports

XPS is a very useful technique to investigate the chemical and electronic properties of the heterogeneous catalysts. Particularly, the presence of defects in the structure of ZnO can cause changes in chemical bonding resulting in the shifts of Binding Energy (BE) of the elements in XPS [36]. Thus, the XPS spectra of Pd 3d, Zn 2p, O 1s and C 1s were recorded for selected catalysts and a representative ZnO_H_2 support. A general XPS survey spectra of all of the catalyst samples showed Pd, Zn, C and O throughout the experiments. With the goal to investigate the abundance of the oxygen vacancies on the PdZn supported on various ZnO supports, the electronic state of the O 1s XPS peak was firstly analysed in higher resolution. A resulting comparison of XPS spectra of oxygen 1sregion of the $PdZn/ZnO\_H_2$ and $PdZn/ZnO\_O_2$ is shown in Figure 4.7. In all cases studied, the obtained O1s asymmetric peak was coherently fitted with three components in agreement with previously reported studies [38]. Accordingly, the oxygen species on the lowest side of the O 1s spectrum labelled as Oa can be attributed to Zn-O bonds of highly crystalline ZnO. The component with the medium BE (labelled Ob) can be assigned to O^{2-} ions in oxygen deficient areas of the ZnO lattice. The changes in intensity of this component mirror the variation in the concentration of oxygen vacancies in ZnO support. In addition, the highest BE peak labelled Oc is associated with adsorbed OH groups on the surface of ZnO. These groups most likely originate from dissociation of adsorbed water on ZnO, which was produced during reduction of PdO [39].

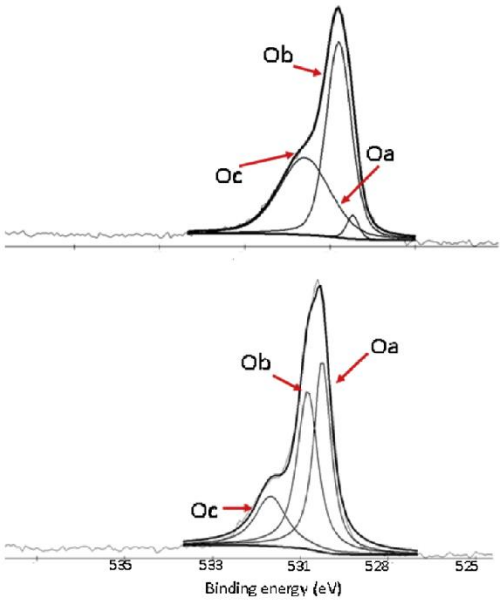

Figure 4.7 - Comparison of the O 1s spectra of PdZn_ZnO_H_2 (top) and PdZn_ZnO_O_2 (bottom) with the assigned peaks from various oxygen species.

The BE and composition of O 1s spectra of the representative catalysts and ZnO_H_2 support are gathered in Table 4.3. As indicated by the results, the highest amount of vacancies (Ob) was found in PdZn_ZnO_H_2. Over 52% of the total oxygen species present on the surface of this catalyst was associated with oxygen defects. On the other hand, the lowest amount of oxygen vacancies was found in PdZn_ZnO_COM. Moreover, the PdZn supported on ZnO_COM had the highest relative concentration of stoichiometric oxygen (Oa) which agrees well with the XRD result (see Figure 4.1), showing that ZnO_COM had a more crystalline nature than the hydrothermally produced counterparts. In addition, a small shift towards lower values of the BE of oxygen can be noted in case of the most active catalyst as compared to other samples (see Table 4.3). This can suggest that the electrons are easier to be excited in ZnO_H_2 due to the significantly higher mobility of interstitial charge associated with oxygen vacancies. A similar shift of BE of O 1s was previously reported for Cu supported on polar ZnO and was linked to the presence of defects in the ZnO support [21]. Further, as shown in Table 4.3, the composition of O

1s peak in ZnO_H_2 did not change significantly upon addition of Pd and subsequent PdZn alloy formation via reduction in H_2. However, a shift of BE towards higher values was observed in PdZn_ZnO_H_2 as compared to pure support ZnO_H_2 (Table 4.3), which can be attributed to the electronic inter-action between PdZn and support. The electronic synergy leads to a lower charge concentration and thus a higher oxidation state of oxygen.

Table 4.3 - BE and relative intensities of components of O 1s XPS spectra.

Sample	Oa BE (eV)	%	Ob BE (eV)	%	Oc BE (eV)	%
PdZn_ZnO_H_2	530.2	4.6	530.7	52	531.9	43.4
ZnO_H_2	529.8	5.9	530.2	53	531.7	40.7
PdZn_ZnO_O_2	530.2	40.5	530.8	40.2	532.0	19.2
PdZn_ZnO_COM	530.4	66	531.6	11	532.3	23
PdZn_ZnO_air	530.5	58	531.1	19	532.1	22

With regards to the chemical state of Zn in PdZn/ZnO catalysts, the XPS spectra of Zn 2p and Auger Zn LMM peaks were also analysed. The representative XPS spectra of Zn $2p_{3/2}$ of PdZn_ZnO_COM is shown in Figure 4.8. The obtained asymmetric Zn peak could be fit-ted with two components. Thus, two Zn species coexisted in all of the analyzed catalysts. The lower binding energy was assigned to metallic Zn and the higher BE was assigned to oxidized Zn [40, 41]. Similar XPS spectra were obtained for the other studied catalysts.

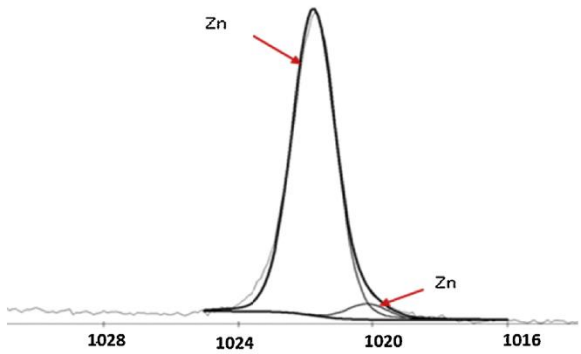

Figure 4.8 - Representative highly resolved core level Zn $2p_{3/2}$ spectrum of PdZn_ZnO_COM.

Different amount of oxygen vacancies in ZnO supports was also confirmed by studying the Auger line of Zn LMM. The BE of Auger Zn LMM is generally more sensitive to the chemical environment [38]. As shown in Figure 4.9, there is a positive shift of BE in the presence of an alloy, which is slightly higher in case of the most active PdZn/ZnO_H_2 sample. The shift of Zn LMM peaks from low BE to higher values in the presence of the PdZn alloy was caused by the decreased negative charge on Zn. This can be attributed to a synergy between support and PdZn particles in which the electrons from Zn interact with the positively charged oxygen vacancies unquestionably present on the interface in the PdZn/ZnO_H_2 sample.

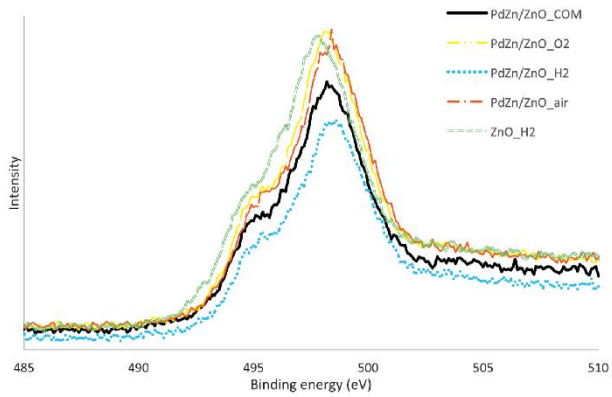

Figure 4.9 - The Zn LMM line of PdZn/ZnO catalysts as compared to pure ZnO_H_2_support.

The influence of the calcination atmosphere of ZnO on the chemical and electronic state of Pd species in PdZn/ZnO catalyst was analysed in detail. It was expected that the small local variation of the electronic charge concentration in the ZnO supports would influence the BE of Pd in the resulting PdZn/ZnO catalysts. In our study, careful fitting of the obtained XPS signal of Pd 3d in case of all of the catalysts studied here showed similarly the coexistence of three different Pd species. For example, a representative Pd 3d XPS spectrum of PdZn/ZnO_H_2 catalyst is shown in Figure 4.10. The Pd 3d region presented a doublet of Pd $3d_{5/2}$ and Pd $3d_{3/2}$ at 335.04 and 340.35 eV, which was assigned to Pd (0) species. Another doublet positioned at 335.93 and 341.29 eV can be assigned to Pd in PdZn alloy. With accordance to the literature, the bimetallic bonding with Zn produces positive BE shift in the core levels and valence d band of the group 10 metals [42]. The positive shift is connected with the reduction of electron population and subsequent shift of the valence d orbital. The remaining third doublet at 336.6 and 342.4 eV would be attributed to oxidized Pd. The presence of oxidized Pd could be expected due to the fact that Pd easily reacts with oxygen from air at ambient conditions and the samples were not pre-reduced *in situ* before the XPS-experiment. The XPS assignment agrees well with the values reported in the literature [17, 43]. The existence of Pd in the metallic state can be the result of not complete alloy formation, or the decomposition of PdZn alloy upon air exposure to Pd and Zn [43]. Additionally, the presence of separately existing metallic Pd particles on XPS spectra agrees well with our results from HRTEM image analysis of lattice spacing of single particles.

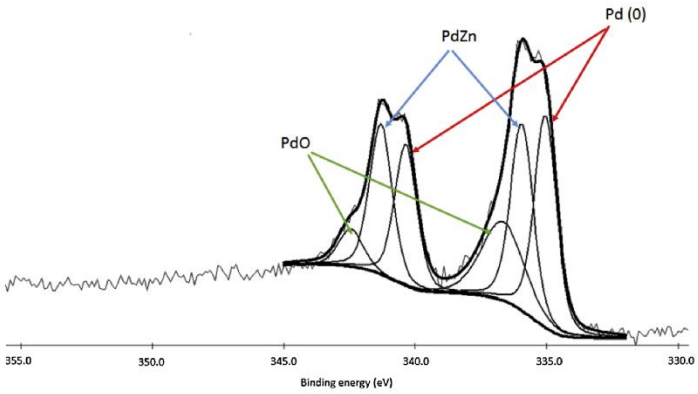

Figure 4.10 - Representative XPS spectra of the elemental peaks of Pd 3d in PdZn/ZnO_H_2

For comparison, the binding energies obtained for PdZn/ZnO_COM, PdZn/ZnO_air, PdZn/ZnO_H_2, PdZn-ZnO_O_2 are listed in Table 4.4. As it can be seen in this table, the XPS surface analysis showed that the surface of the investigated catalysts was composed of PdZn alloyed particles as well as separately existing Pd metallic particles dispersed on the surface of ZnO support.

Table 4.4 - BE and composition of Pd 3d XPS spectra of studied PdZn/ZnO catalysts.

Sample	BE (eV) Pd $3d_{5/2}$	BE (eV) PdZn	BE (eV) PdO	Pd 3d/Zn 2p	Composition (%)
PdZn/ZnO_COM	334.75	335.64	337.11	0.1	34/56/9
PdZn/ZnO_air	334.88	335.58	336.61	0.06	39/38/22
PdZn/ZnO_H_2	335.04	335.93	336.66	0.12	29/51/19
PdZn/ZnO_O_2	334.89	335.70	336.73	0.07	31/36/32

The observed positive shift of binding energy (BE) of Pd 3d in PdZn/ZnO_H_2 is the result of the strong synergy between the metal alloy nanoparticles and ZnO support. The increase of BE can be explained by the interaction of separately existing Pd (0) particles with local positively charged oxygen vacancies on ZnO support, resulting in the charge withdrawal from Pd metal, causing the increase in BE in the core level of the metal. In addition, the binding energy of Pd in PdZn alloy is shifted to the highest value in PdZn/ZnO_H_2 as compared BE of PdZn in other studied

catalysts. This shift of BE suggests that the surface of PdZn alloy in the most active catalyst is the richest in Zn of all the PdZn surfaces of the studied catalysts. Noteworthy, better catalytic performance of Zn rich PdZn alloys was previously reported in MSR [17, 24]. Moreover, the ratio of intensity of the photoelectron peak of Zn $2p_{3/2}$ to Pd $3d_{5/2}$ was calculated, normalised by the appropriate atomic sensitivity factors of Pd = 4.8 and Zn = 4.6 [44]. As it is listed in Table 4.4, the most active catalyst PdZn/ZnO_H_2 as well as the least active PdZn/ZnO_COM had the highest total amount of Pd exposed on the surface of the catalyst, whereas PdZn supported on ZnO calcined in oxidizing atmospheres had relatively less exposure of Pd on the surface. Taking into consideration that ZnO calcined in O_2 or air had significantly higher BET surface areas (see Table 4.1), it is most likely that Pd in these catalysts is encapsulated in the pores of ZnO supports. The composition of Pd 3d based on the relative intensity of Pd 3d signals was calculated and it is shown in Table 4.4. When comparing the catalysts activity results (see Table 4.2) with the catalyst compositions taken from XPS results, a clear correlation can be established between the selectivity to CO_2 of PdZn/ZnO catalysts and the extent of alloy formation. The selectivity to MSR increased proportionally to the amount of PdZn alloy formed. Interestingly, PdZn/ZnO_COM with a high alloy extent (over 50%), showed the poorest activity in low temperature-MSR. On the other hand, PdZn/ZnO_H_2 with very similar composition of Pd 3d peak showed the best performance regarding selectivity and activity in this reaction. Therefore, it can be concluded that no direct correlation could be found between the extent of alloy formation and activity of the catalyst in low temperature-MSR. On the other hand, lower activity of PdZn_ZnO_COM generally could be associated with a much higher size of PdZn alloy. However it was previously reported that the increase in PdZn particle had no adverse effect on the activity of the catalyst in MSR [34]. Thus, the lower activity can be associated with the negative influence of the type of active sites present on the surface of ZnO_COM support.

4.3.5. *Study of the metal-support interaction by TPR experiments*

In order to explore in more detail the interaction between metal species and ZnO supports calcined in various atmospheres, TPR experiments were conducted. The XPS study showed clearly that the electronic state of ZnO support is strongly affected by the type of gas used during its calcination. Thus, it could be anticipated that the reduction characteristics of these catalysts would also vary with the type of ZnO support or more specifically with the calcination atmosphere of the support.

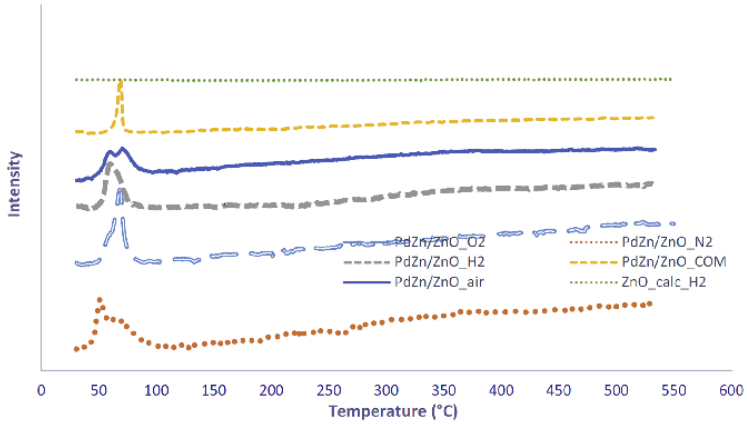

Figure 4.11 - H_2-TPR profile of ZnO_H_2 and PdZn/ZnO catalysts.

The H_2-TPR profiles of the studied catalysts are displayed in Figure 4.11. It should be noted that no hydrogen consumption or desorption was recorded on the pure ZnO_H_2 support. This clearly indicates that in the absence of Pd, ZnO_H_2 cannot be reduced below 600 °C. Surprisingly, the negative peak at low temperature commonly assigned to decomposition of PdH_x was not observed in our experiments. This low temperature peak indicates the presence of metallic Pd in the samples [34]. The presence of Pd metal was evident in the XPS results and HRTEM, so the absence of this TPR peak was rather surprising. Nevertheless, this can be explained by the fact that the hydride could be decomposed once it was formed; therefore observation of the TPR decomposition peak could be masked by a major and positive

peak due to the reduction of PdO as it was reported in other studies [39]. It was noted that the reduction of all of the PdZn/ZnO catalysts started at a similar low temperature range of 51–70 °C. These TPR peaks were undoubtedly attributed to the reduction of PdO [45, 46]. It should be mentioned that these reduction temperatures are generally lower than the values reported in the literature for similar catalytic systems [46, 47]. This indicates that the palladium oxide in this work was present in the form of a passive thin surface layer on the well dispersed Pd particles. Interestingly, there are two overlapping peaks observed in the case of catalysts calcined in N_2, and air (the first around 60 °C and the other around 70 °C), but importantly, in the case of the former the low temperature peak is more prominent. On the other hand, in PdZn/ZnO_air, a slightly higher intensity was recorded for the higher temperature peak. The difference in intensity of these peaks can be the result of the influence of the presence of O_2 during calcination of ZnO_air, which is able to create special active sites on the support. This assumption was confirmed by the TPR profile of PdZn/ZnO_O_2, where one peak is observed at around the same temperature of 72 °C with a small shoulder at lower temperatures. The presence of two peaks in the TPR profile suggests the coexistence of two different Pd^{2+} species with different environment and type of interaction with ZnO support. Thus, the lower temperature peak was attributed to the interface-boundary oxygen atoms on Pd which are in close vicinity to the oxygen vacancies. The reduction of PdO in these areas is promoted by strong metal–support interaction and it is influenced by the increased mobility of lattice oxygen. Thus, this peak is more intense in PdZn supported on ZnO_N_2 than in PdZn_ZnO_air. Similar observations were made in the TPR studies of Cu catalysts [47] and Ce doped with CuO [48, 49].With a strong agreement to the above conclusion, the most active catalyst (PdZn/ZnO_H_2) shows a broad peak at a lower temperature (58 °C), suggesting the presence of the active sites in the close proximity to the defected ZnO sites. In addition, as it could be anticipated from other results, PdZn_COM showed a single very sharp peak at a higher temperature (68 °C), indicating one type of PdO present on this catalyst, possibly supported on stoichiometric ZnO. In addition, there is a very broad peak visible in temperatures above 250 °C in all of catalysts studied, which represents a continuous PdZn alloy formation [4]. The dissociation of molecular hydrogen on the surface of Pd metal provides very active atomic hydrogen which reduces ZnO by abstracting $O^{2-}$from its

surface. Overall, the presence of oxygen vacancies is apparent in TPR results, leading to a significant decrease in the reduction temperature of the neighboring PdO. Noteworthy, a decrease in the reduction temperature of the metal oxide supported on redox-active oxide such as ZnO is a reliable sign of the established strong metal support interaction (SMSI) [26]. It is clear that the calcination atmosphere of ZnO influences the reduction profile of the PdZn/ZnO catalysts. In summary, the TPR results agreed well with the XPS findings and also points at existence of metallic Pd particles along with PdZn alloyed particles on the surface of ZnO.

4.3.6. DRIFT study of CO adsorption on PdZn/ZnO catalysts

CO-adsorption-DRIFT analysis presents a unique tool to probe the chemical nature of the adsorption sites on the catalyst surface. This is because the bonding of CO to the metal is sensitive to the oxidation and coordination of the catalytically active sites. Thus, the position of the CO adsorption band on a given metal depends on the oxidation state of a metal site, nature of exposed faces and the particle size [50]. It is clear that the existence of different active sites/ensembles on PdZn/ZnO catalyst may lead to pronounced differences in its performance in low temperature-MSR. Thus, DRIFT spectra using CO as a probe molecule were recorded at room temperature in the region of 2200-1900 cm^{-1} for representative PdZn/ZnO catalysts. The resulting DRIFT spectra are presented in Figure 4.12. The spectra were recorded in the increasing CO exposure time from spectra 1 freshly reduced catalyst to spectra to spectra three, four-fully saturated sample.

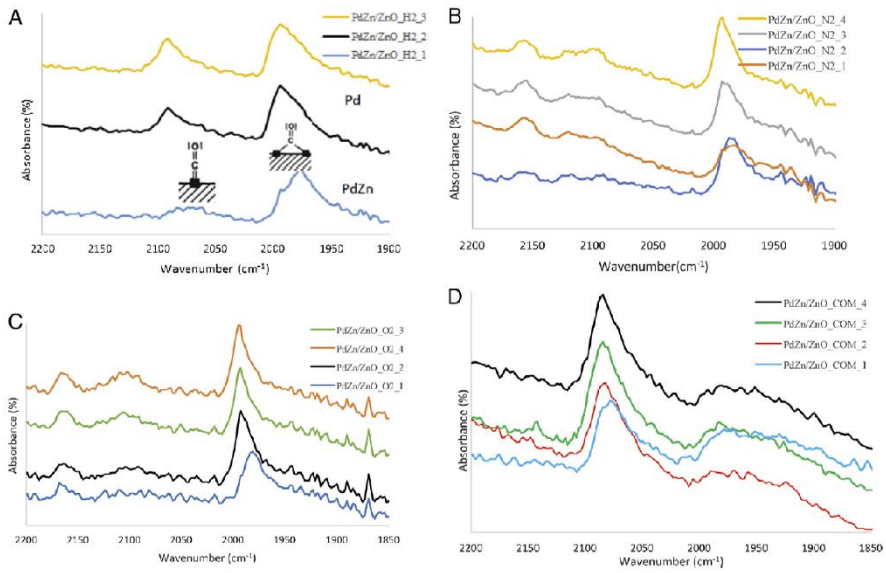

Figure 4.12 - CO adsorption at room temperature on A) PdZn/ZnO_H_2; B) PdZn/ZnO_N_2; C) PdZn/ZnO_O_2 and D) PdZn/ZnO_COM. Spectra 1–4 were recorded with increasing time of CO exposure.

All the DRIFT results showed the coordination bands of CO in two regions. CO adsorbed in bridging mode (1981–1960 cm^{-1}) on the Pd (0) and CO adsorption on the steps and edges of rows of Pd in PdZn in linear (a-top) mode (2093-2010 cm^{-1}) [51, 52]. The modes of adsorption are schematically shown in Figure 4.12 A. The bands with a wavenumber higher than 2150 cm^{-1} can be assigned to CO in gas phase [52]. As it can be seen from this study, the type of ZnO substrate affects the vibrational frequency of adsorbed CO. The presence of the bridging mode is the result of ensemble of neighboring Pd atoms on the surface of all the catalysts. This confirms the previous results from the catalysts composition obtained in TPR, XPS and HRTEM studies. The CO adsorbs mostly in bridging mode on PdZn/ZnO_N_2 and PdZn/ZnO_O_2. This finding agrees well with the XPS results that showed lower alloy formation in PdZn/ZnO_O_2 sample as compared with PdZn/ZnO_COM. Thus, due to higher alloy extent present in PdZn/ZnO_COM, CO adsorbed mainly in linear mode on this sample (see Figure 4.12 D). Moreover, higher concentration of CO linearly bonded to Pd was found on the samples with higher concentration of Zn on the surface [52]. Taking into consideration the size of the PdZn nanoparticles, it can be

concluded that CO adsorbs mostly in bridging mode on the smaller PdZn particles. On the most active catalyst, PdZn/ZnO_H_2 there is also two adsorption modes present. Careful analysis of the wavenumbers revealed that there is a blueshift of bridging mode on the PdZn/ZnO_H_2 (1975.58 cm^{-1}) and linear mode (2075.1 cm^{-1}) as compared to the bridging mode (1979.1 cm^{-1}) and linear mode (2087 cm^{-1}) on PdZn/ZnO_O_2 or bridging (1981.1 cm^{-1}) and linear (2100 cm^{-1}) on PdZn/ZnO_N_2. This shift of wavenumber to lower values can be ascribed to the electronic interaction between Pd and ZnO support. The presence of free electrons from oxygen vacancies in ZnO increases the charge of Pd. In general, higher electron density of metal increases the back-donation to 2Π* orbitals of adsorbed CO which in turn makes the adsorption weaker and shifted to lower frequencies [36]. The presence of free electrons associated with the vacancies on ZnO support in PdZn/ZnO_H_2 sample was previously confirmed by TPR and XPS results in the present work.

Moreover, limited stability of the PdZn surface alloy in all of the samples was observed with a prolonged exposure to CO atmosphere. As it can be seen in Figure 4.12, there was a redshift observed with increasing time in CO atmosphere. The saturated spectra numbers three and four on each of the samples in this figure closely resembled that of CO adsorbed on Pd metal. This result strongly indicates that there are some homogenous structural changes taking place on the surface of the studied catalysts. With increasing time, new surface sites are created on these catalysts which are probably Pd rich. Since interaction of CO with Pd sites is much stronger than its interaction with Zn containing sites [36] it can be assumed that as a result of the strong interaction with CO, the Pd atoms in PdZn bulk alloy segregate to the surface. Similar observations were described by other authors [53], however in our case changes of observed intensity of the bands were only noted in case of PdZn/ZnO_H_2 sample. The most active catalyst showed redshift of the frequencies accompanied by increased intensity of bridging mode with exposure time. In this case, the surface reconstruction step might be affected by the presence of free electrons on the surface of ZnO support, which can give rise to the production of new active sites on the surface. Therefore, it is very likely that the PdZn alloys on these supports could be prone to segregation of Pd to the surface of the catalyst.

The results of CO–DRIFT analysis suggested that the stability of these catalysts under methanol steam reforming conditions could be limited. Actually, the stability of the catalyst PdZn_ZnO_H_2 was tested under methanol steam reforming conditions for a period of 48 h. A total drop of conversion of 24% was recorded, which is slightly higher than the values reported in the literature for the similar system [54]. This very interesting result can be undoubtedly attributed to the restructuring changes of the surface of PdZn/ZnO catalyst under MSR conditions.

4.4. Conclusions

The obtained results clearly identify that strong synergism between active sites present on intermetallic PdZn alloy and active sites present ZnO support is necessary to obtain excellent catalytic performance of PdZn/ZnO systems in methanol steam reforming. The XPS study showed that the composition of the surface of the studied catalysts contained a mixture of Pd metallic and PdZn alloyed particles supported on ZnO. It should be noted that the amount of Pd metallic present on the surface of the studied catalysts as calculated from XPS experiments was very similar in case of all the materials studied. Therefore, it can be concluded that the presence of these particles had no adverse effects on the catalysts performance, which agrees well with the literature findings [35]. Indeed, the activity of these monometallic Pd particles is altered by the presence of the ZnO support, favoring higher production of CO_2 over CO.

The influence of the calcination atmosphere of the ZnO precursor on the performance of PdZn/ZnO catalyst in low temperature MSR was studied in detail and a very active and ultraselective catalyst was obtained by supporting Pd on ZnO calcined in H_2. The activity of the PdZn catalyst was found to be independent of the extent of the PdZn alloy formed. However, higher selectivities to CO_2 were achieved by the samples showing higher amount of PdZn alloy on the surface as evidenced by XPS results. The extent of alloy formation was found to be influenced by the BET surface area and ZnO supports with higher BET values displayed lower extent of alloy formation. A direct correlation was found for the first time between the

catalytic performance of PdZn/ZnO catalysts in low temperature MSR and the calcination atmosphere of the ZnO support. Thus, the performance of the catalysts increased from PdZn supported on ZnO calcined in oxidative atmospheres to PdZn/ZnO calcined in nitrogen and was the best in case of PdZn supported on ZnO calcined in H_2.The exceptional performance in low temperature MSR of PdZn/ZnO_H_2 catalyst was attributed to the presence of higher concentration of oxygen vacancies in ZnO_H_2, as evidenced by TPR, XPS and CO-DRIFT studies. The gathered results showed that the activity of PdZn catalyst is strongly affected by the morphology and crystallinity of the ZnO support which governs the type of specific active sites responsible mainly for water activation. The stronger synergy between Pd and ZnO was achieved in the presence of oxygen vacancies in ZnO support, which resulted in the high selectivity towards MSR of the best catalyst. Thus, a clear correlation was discovered for the first time between the amount of oxygen defects present on the ZnO support as indicated by XPS, TPR, CO-DRIFT studies and the activity of PdZn/ZnO catalysts. Unfortunately, the PdZn alloy in these systems was found to be unstable under prolonged CO exposure during DRIFT experiments. The stability test carried out under methanol steam reforming conditions showed a 24% drop in conversion of the most active catalyst during 48 h on stream. Thus, it was confirmed that surface reconstruction is likely to take place during the MSR reaction, possibly involving either segregation of Pd to the surface from the bulk of the PdZn alloy, or other changes in the composition of the PdZn alloy due to reordering under reaction conditions. Further research is currently carried out to understand the mechanism of deactivation of these catalytic systems.

To sum up, it is expected that the presented results would aid in the rational design of more active and selective catalyst for application at even lower temperature (170 °C) for hydrogen production by MSR.

4.5. Acknowledgement

The research leading to these results has received funding from European Union' Seventh Framework Programme (FP7/2007-2013) for the Fuel Cells and Hydrogen

Joint Technology Initiative under grant agreement number {303476} 10 (BeingEnergy). K.Eblagon is grateful for the financial support from FCT postdoctoral grant (PTDC/CTM/108454/2008) co-financed by FEDER and POFC and PTDC/EQU-EQU/104217/2008. The work of H. Silva was supported by FCT, grant SFRH/BD/45890/2008. Mr. F. Eblagon and Dr L. Brandão are acknowledged for fruitful discussions of the data. Dr J. L. Jorda Moret from ITQ-Universidad Politecnica de Valencia is thanked for performing the XRD study of PdZn alloy formation. Authors are also grateful to Dr M. Reinikainen and Dr S. Pekka from VTT Technical Research Centre of Finland for performing TPR measurements. Mr. P. Ribeirinha from FEUP is thanked for performing the stability tests and Dr. P.J.F.Harris is acknowledged for performing additional HRTEM characterization.

4.6. References

[1] M.U. Niemann, S.S. Srinivasan, A.R. Phani, A. Kumar, D.Y. Goswami, E.K. Stefanakos, J. Nanomater. 2008 (2008) 1–9.

[2] B. Lindström, L.J. Pettersson, P.G. Menon, Appl. Catal. A 234 (2002)11–125.

[3] Y.-H.P. Zhang, J.-H. Xu, J.-J. Zhong, Int. J. Energy. Res. 37 (2013) 769–779.

[4] N. Iwasa, M. Yokoshikawa, W. Nomura, M. Arai, Appl. Catal. A 292 (2005)215–222.

[5] G.A. Olah, Angew. Chem. Int. Ed. 44 (2005) 2636–2639.

[6] S. Kim, M. Kang, J. Ind. Eng. Chem. 18 (2012) 969–978.

[7] D.R. Palo, Chem. Rev. 107 (2007) 3992–42021.

[8] P. Bichon, M. Asheim, A. Jordal, T. Sperle, M. Fathi, A. Holmen, E.A. Blekkan, Int.J. Hydrogen Energy 32 (2007) 1799–1805.

[9] J.-P. Shen, C. Song, Catal. Today 77 (2002) 89–98.

[10] C.E. Taylor, B.H. Howard, C.R. Myers, Ind. Eng. Chem. Res. 46 (2007) 8906–8909.

[11] O. Llinich, Y. Liu, C. Castellano, G. Koermer, A. Moini, R. Farrauto, Platinum Met.Rev. 52 (2008) 134–143.

[12] K.M.K. Yu, W. Tong, A. West, K. Cheung, T. Li, G. Smith, Y. Guo, S.C. Tsang, Nat.Commun. 3 (2012) 1–7.

[13] S. Sá, H. Silva, L. Brandão, J.M. Sousa, A. Mendes, Appl. Catal. B 99 (2010)43–57.

[14] M.-C. Tsai, J.-H. Wang, C.-C. Shen, C.-T. Yeh, J. Catal. 279 (2011)

[15] Y. Matsumura, H. Ishibe, J. Mol. Catal. A 345 (2011) 44–53.

[16] N. Iwasa, S. Kudo, H. Takahashi, S. Masuda, N. Takezawa, Catal. Lett. 19 (1993)211–216.

[17] M. Friedrich, D. Teshner, A. Knop-Gericke, M. Armbruster, J. Catal. 285 (2012)41–47.

[18] Y. Usami, K. Kagawa, M. Kawazoe, Y. Matsumura, Appl. Catal. A 171 (1998)123–130.

[19] N. Iwasa, N. Takezawa, Top. Catal. 22 (2003) 215–224.

[20] M. Friedrich, S. Penner, M. Heggen, M. Armbruster, Angew. Chem. Int. Ed. 52(2013) 4389–4392.

[21] F. Liao, Y. Huang, J. Ge, W. Zheng, K. Tedsree, P. Collier, X. Hong, S.C. Tsang,Angew. Chem. Int. Ed. 50 (2011) 2162–2165.

[22] E. Jeroro, J.M. Vohs, J. Am. Chem. Soc. 130 (2008) 10199–10207.

[23] H. Lorenz, C. Rameshan, T. Bielz, N. Memmel, W. Stadlmayr, L. Mayr, Q. Zhao, S.Soisuwan, B. Klötze, Chem. Catal. Chem. 5 (2013) 1273–1285.

[24] J. Strunk, K. Kahler, X. Xia, M. Muhler, Surf. Sci. 603 (2009) 1776–1783.

[25] B. Halevi, S. Lin, A. Roy, H. Zhang, E. Jeroro, J. Vohs, Y. Wang, H. Guo, J. Phys.Chem. C 117 (2013) 6493–6503.

[26] N. Acerbi, S.C.E. Tsang, G. Jones, S. Golunski, P. Collier, Angew. Chem. Int. Ed. 52(2013) 1–6.

[27] G. Xiong, L. Luo, C. Li, X. Yang, Energy Fuels 23 (2009) 1342–1346.

[28] M. Arsalanfar, A.A. Mirzaei, H.R. Bozorgzadeh, J. Nat. Gas Sci. Eng. 6 (2012) 1–13.

[29] M.Y. Ge, H.P. Wu, L. Niu, J.F. Liu, S.Y. Chen, P.Y. Shen, Y.W. Zeng, J. Cryst. Growth 305 (2007) 162–166.

[30] J. Kiss, A. Witt, B. Meyer, D. Marx, J. Chem. Phys. 130 (2009) 184706–184720.

[31] G.R. Li, T. Hu, G.L. Pan, T.Y. Yan, X.P. Gao, H.Y. Zhu, J. Phys. Chem. C 112 (2008)11859–11864.

[32] A. Mclaren, T. Valdes-Solis, G. Li, S.C. Tsang, J. Am. Chem. Soc. 131 (2009)12540–12541.

[33] C. Shao, L. Tu, A. Yu, B. Li, X. Zhou, Thin Solid Films 525 (2012) 148–153.

[34] W. Yanhua, Z. Jingchang, X. Hengyong, B. Xuefeng, Chin. J. Catal. 28 (2007)234–238.

[35] A. Karim, T. Conant, A. Datye, J. Catal. 243 (2006) 420–427.

[36] I. Eswaramoorthi, A.K. Dalai, Int. J. Hydrogen Energy 34 (2009) 2580–2590.

[37] S. Du, Y. Tian, H. Liu, J. Liu, Y. Chen, J. Am. Ceram. Soc. 89 (2006) 2440–2443.

[38] P.T. Hsieh, Y.C. Chen, K.S. Kao, C.M. Wang, Appl. Phys. A 90 (2008) 317–321.

[39] M.L. Cubeiro, J.L.G. Fierro, Appl. Catal. A: Gen. 168 (1998) 307–322.

[40] M. Chen, X. Wang, Y.H. Yu, Z.L. Pei, X.D. Bai, C. Sun, R.F. Huang, L.S. Wen, Appl.Surf. Sci. (2000) 134–140.

[41] M. Leonarda, E. Moretti, L. Storaro, P. Patrono, F. Pinari, E. Rodriguez-Castellon,A. Jimenez-Lopez, G. Busca, E. Finocchio, T. Montanari, R. Frattini, Appl. Catal.312 (2006) 220–228.

[42] J.A. Rodriguez, M. Kuhn, J. Phys. Chem. 100 (1996) 381–389.

[43] V. Engels, D.A. Jefferson, F. Benaskar, P.C. Thune, A. Berenguer-Murcia, B.F.G.Johnson, A.E.H. Wheatley, Nanot 22 (2011) 205701–205721.

[44] http://www.cem.msu.edu [Online].

[45] P. Pfeifer, K. Schubert, M.A. Liauw, G. Emig, Appl. Catal., A 270 (2004) 165–175.

[46] Y.-H. Chin, R. Dagle, J. Hu, A.C. Dohnalkova, Y. Wang, Catal. Today 77 (2002)79–88.

[47] L. Yang, G.-D. Lin, H.-B. Zhang, Appl. Catal., A 455 (2013) 137–144.

[48] S. Patel, K.K. Pant, Fuel Process. Technol. 88 (2007) 825–832.

[49] A. Aranda, S. Agouram, J.M. López, A.M. Mastral, D.R. Sellick, B. Solsona, S.H.Taylor, T. García, Appl. Catal., B 127 (2012) 77–88.

[50] S. Royer, D. Duprez, Chem. Catal. Chem. 3 (2011) 24–65.

[51] W. Stadlmayr, C. Rameshan, C. Weilach, H. Lorenz, M. Hävecker, R. Blume, T.Rocha, D. Teschner, A. Knop-Gericke, D. Zemlyanov, S. Penner, R. Schlögl, G.Rupprechter, B. Klötzer, N. Memmel, J. Phys. Chem. C 114 (2010) 10850–10856.

[52] L. Bollmann, J.L. Ratts, A.M. Joshi, W.D. Williams, J. Pazmino, Y.V. Joshi, J.T. Miller,J. Catal. 257 (2008) 43–54.

[53] K. Föttinger, Catal. Today 208 (2013) 106–112.

[54] T. Conant, A.M. Karim, V. Lebarbier, Y. Wang, F. Girgsdies, R. Schlögl, A. Datye,J. Catal. 257 (2008) 64–70.

Chapter 5

The contributions of the author of this thesis in the following chapter are: performance of experimental work (e.g. kinetic experiments, characterization of textural and reducibility properties of the studied materials); fitting of the experimental data to kinetic models described in the literature; interpretation and discussion of the results.

Writing of a first version of the manuscript results that had the important contribution of Dr. Cecilia Mateos Pedrero and Professor Adélio Mendes for obtaining the final version, which was revised by all the co-authors.

The author of this thesis had a percentual contribution as part of the research team of 60 %.

.

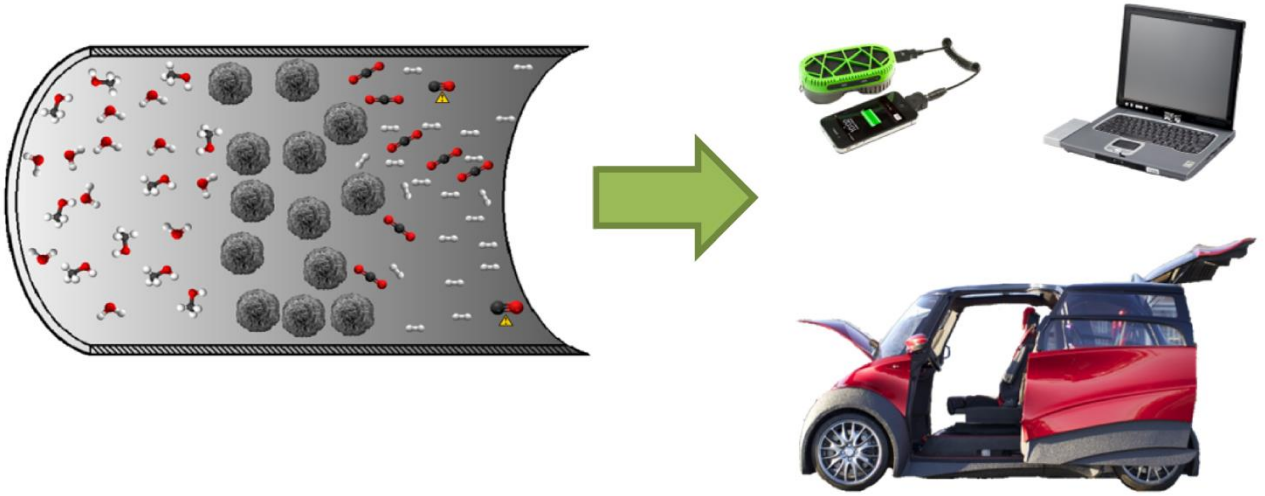

Chapter 5. Low-Temperature Methanol Steam Reforming Kinetics over a novel CuZrDyAl Catalyst[4]

Abstract

A kinetic study within the low-temperature methanol steam reforming (MSR) reaction was performed over a novel CuZrDyAl catalyst. The physicochemical and catalytic properties of the CuZrDyAl catalyst were compared with those of a conventional $CuO/ZnO/Al_2O_3$ (G66 MR, Süd-Chemie) sample. The in-house catalyst displays better performances,than the reference G66 MR sample in terms of methanol conversion and selectivity. The parameters of a simple power-law equation and two mechanistic kinetic models were determined minimizing the residual sum of squares; the best fitting with the experimental data was obtained when using Model 3, based on the reported work from Peppley *et al.* [13] for the commercial $CuO/ZnO/Al_2O_3$. Noteworthy, is the small number of MSR kinetic studies at 170 °C - 200 °C temperature range

[4] Silva H, Mateos-Pedrero C, Ribeirinha P, M. Boaventura, C. Mateos Pedrero, A. Mendes (2015) Low-temperature methanol steam reforming kinetics over a novel CuZrDyAl catalyst. React Kinet Mech Catal 115:321–339.

5.1. Introduction

Hydrogen is considered the energy vector of the future where fuel cells are expected to have a key role as energy converting devices with high efficiency [1]. Despite being a clean energy carrier, handling and storage an explosive gas such as hydrogen requires special conditions and special materials to minimize diffusion and leakages [2]. Different techniques are currently considered: the use of hydrogen tanks at very high pressures (up to 700 bar), hydrogen liquefaction and the use of chemical substances that have the capacity of reacting reversely with hydrogen, such as metallic and organic hydrides [3]. Nevertheless, none of the mentioned approaches can reach competitive volumetric energy densities levels of common fuels. For example, liquid hydrogen has a volumetric energy density of 9.8 $MJ \cdot L^{-1}$, ca.3-4 times lower than gasoline or diesel fuels [4]. This has engaged the search of parallel strategies to provide hydrogen grade for fuel cells, namely the *in situ* reforming of fuels such as methanol, DME, ethanol or methane. Methanol has unique advantages: it is liquid fuel at ambient conditions with a volumetric energy density of 15.9 $MJ \cdot L^{-1}$ (LHV) –[4]); it has a high hydrogen to carbon ratio with no carbon-carbon covalent bonds, which opens the possibility of low-temperature reforming (150 °C - 300 °C) [5, 6]. Though, undesirable carbon monoxide (CO) is formed in sideways reactions of methanol steam reforming (MSR), methanol decomposition (MD) and reverse water-gas shift (RWGS):

$$CH_3OH \rightleftarrows CO + 2H_2 \qquad \Delta H = 92.0 \ kJmol^{-1} \qquad (5.1)$$

$$CO + H_2O \rightleftarrows CO_2 + H_2 \qquad \Delta H = -41.2 \ kJmol^{-1} \qquad (5.2)$$

Carbon monoxide has a detrimental influence on the performance of fuel cells as a consequence of the well-known poisoning effect on the Pt-based electrochemical anode catalyst of the polymer electrolyte membrane fuel cells (PEMFC). Hydrogen grade standards for fuel cell vehicles refer that the CO concentration should be below 0.2 ppm for automotive applications [7]. Recently high temperature polymer electrolyte membrane fuel cells (HT-PEMFC) technology, which operate in temperature range of 160 °C and 200 °C, shifted the limit of CO concentration to ca. 0.1 % (1000 ppm) at 170 ºC. As additional advantages HT-PEMFCs have higher

electrochemical catalytic activity, simpler water management and simpler integration with methanol steam reformers compared to low-temperature PEMFCs; preferential oxidation reactors, humidifiers, air compressors and radiators are among the dispensable process units [8].

The integration of a methanol reformer with HT-PEMFCs can assume different configurations. However, coupling the exothermic electrochemical reactor (HT-PEMFC) with the endothermic MSR reactor should result in a significant energy integration if both reactors run at a common temperature; energy savings are ca. 11 % of the methanol fuel energy [9]. Since HT-PEMFCs are limited to operate up to 200 °C, the common temperature should be no more than 200 °C. Thus, the efficiency of a combined system of MSR and HT-PEMFC is highly dependent on the MSR catalyst reaction kinetic at low-temperatures (< 200 ºC), which defines the purity and flow rate of hydrogen produced.

Since the 1960s the developed copper-based catalysts have revolutionized the methanol reformation process [6]. The coprecipitation method is an attractive route to produce these commercial catalysts, especially at a large scale [10]. At present, a completely tuned and commonly used formulation in the industry is the $CuO/ZnO/Al_2O_3$ catalyst, which is also used for methanol production and water-gas shift reaction [5, 11-13]. Nevertheless, there are several reports describing the preparation of copper-based catalysts for MSR using coprecipitation where copper is combined and precipitated with various metals [14-20]. For instance, zirconia has been reported to have a beneficial effect for MSR, attributed to copper improved reducibility and dispersion [16, 18]; rare earth metal oxides have been studied, such as Y, Pr and Tb, and reported as a viable strategy for improving the MSR activity at low- temperatures [15, 21]. Recently, CuZnGaOx formulation has been found to be highly active and suitable for low-temperature methanol steam reforming (LT-MSR). This high activity was assigned to the incorporation of a small amount of Ga that promotes a high copper dispersion on a defective $ZnGa_2O_4$ surface [22-24]. Improving the $CuO/ZnO/Al_2O_3$ commercial catalyst in terms of selectivity and activity would have direct repercussion on the integration of LT-MSR and HT-PEMFC. Most of the kinetic studies in literature concerns with the $CuO/ZnO/Al_2O_3$ catalyst at temperatures above 200 ºC.

A novel CuZrDyAl MSR catalyst was prepared and characterized concerning the morphology and composition and the reaction rate at 170 °C - 200 °C; commercial catalyst G66 MR from Süd-Chemie ($CuO/ZnO/Al_2O_3$) was used as reference for the reaction rate study. Three kinetic models were fitted to the experimental reaction rates, one empirical [25] and two mechanistic [13, 26].

5.2. Experimental

5.2.1. Catalyst Synthesis

A CuZrDyAl sample was prepared by coprecipitation from a 0.8 M aqueous mixture of copper nitrate trihydrate ($Cu(NO_3)_2 \cdot 3H_2O$, VWR), zirconyl nitrate dihydrate ($ZrO(NO_3)_2 \cdot 2H_2O$, Wako), aluminum nitrate nonahydrate ($Al(NO_3)_3 \cdot 9H_2O$, VWR chemicals) and dysprosium nitrate hydrate ($Dy(NO_3)_3 \cdot H_2O$, Sigma-Aldrich), with dropwise (0.64 ml/min) addition of an aqueous solution of Na_2CO_3 (0.9 M) under vigorous stirring at 50 °C. The resulting precipitate was filtered and thoroughly washed with distilled water. The procedure was repeated for several times until the pH value of the filtrate reached the level of the distilled water. The precipitate was then dried at 110 °C overnight and calcined under static air as follows: from 25 °C to 200 °C (heating rate: 2 °C/min; dwell time: 1 h), from 200 °C to 360 °C (heating rate: 2 °C/min; dwell time: 1 h), and finally kept at 360 °C for 8.5 h.

The $CuO/ZnO/Al_2O_3$ (G66 MR from Süd-Chemie) sample was used as supplied.

5.2.2. Characterization

The identification of the crystalline phases was performed by X-ray powder diffraction (XRD), using a Bruker AXS D8 Discover equipment, in θ-2θ mode, with

a step of 0.04° and an integration time of 2s. The mean size of CuO crystallites was determined based on XRD peak broadening using the Scherrer equation:

$$D = K\lambda/(\beta\cos\theta) \quad (5.3)$$

where D is the average size of the CuO crystallites (nm), K is the crystallite-shape factor, λ is the wavelength of the $K\alpha$ radiation of Cu (λ = 1.5418 Å), θ is the Bragg angle, and β is the broadening of the diffraction line measured at half maximum intensity (FWHM). The average particle size was estimated by assuming all the particles to have same spherical shape and size, so that K was 0.9.

The characterization by Scanning Electron Microscopy (SEM) was performed using a FEI Quanta 400 scanning electron microscope equipped with an energy dispersive X-ray high vacuum detector (EDX). The SEM images were captured at low vacuum using the large field detector (LFD).

Induced coupled plasma (ICP-MS) analyses were carried out in a Thermo X Series equipment and samples digested in a high concentrated nitric acid solution.

The reducibility of the CuZrDyAl catalyst was studied by hydrogen temperature programmed reduction (H_2-TPR) measurements under a 5 % hydrogen stream diluted in argon at a total flow rate of 50 $cm^3 \cdot min^{-1}$. The TPR profiles were obtained with an automatic chemisorption analyzer (ChemBET Pulsar TPR/TPD). 50 mg of sample was placed in a long U-shaped quartz cell and heated from 50 °C to 400 °C at a rate of 5 $°C \cdot min^{-1}$. Hydrogen consumption was measured by a thermal conductivity detector (TCD). A copper oxide sample (CuO, *Riedel*-de Haën) was used as reference material.

5.2.3. MSR: Fixed-bed Tests

The MSR reaction rates were obtained at atmospheric pressure in an in-house built set-up [5]. The experimental set-up uses a tubular reactor (7.25 mm i.d., 6 cm length) placed inside an oven. Plug flow conditions were assumed since catalyst diameter to reactor length ratio was higher than 50 ($L_{reactor}/d_{particle} \geq 50$) and the reactor to catalyst diameter ratio was higher than 30 ($d_{reactor}/d_{particle} \geq 30$) [27].

The reaction was performed with a mass of 400 mg of catalyst (W) and the methanol flow rate (F^0) was changed to obtain different space-time ratios (W/F^0). The water: methanol molar ratio was 1.5. Kinetic experiments were performed in the temperature range of 170 °C to 200 °C. Catalyst was reduced *in situ* using a 40 % hydrogen in argon stream at 240 °C for 2 h. The gas feed flow rate was controlled by mass flow controllers from Bronkhorst (model F-201C, ± 0.1 FS). Required flow rate of methanol aqueous solution was controlled using a Controlled Evaporation and Mixing (CEM) system from Bronkhorst. The condensable reactants were separated from the gas mixture in a condenser at ca. 0 °C. Hydrogen and carbon dioxide were analyzed in a quadruple mass spectrometer (Pfeiffer, Vacuum OmniStar GSD 320). Carbon monoxide concentration was measured using CO infrared analyzer from Signal Instruments (7100 FM) with accuracy of ±0.2 ppm. The methanol steam reforming MSR conversion (X_{CH_3OH}) was determined using equation (5.4):

$$X_{\mathrm{CH_3OH}}(\%) = \frac{F^{out}_{\mathrm{CO_2}} + F^{out}_{\mathrm{CO}}}{F^{in}_{\mathrm{CH_3OH}}} \times 100 \tag{5.4}$$

where $F^{out}_{CO_2}$ and F^{out}_{CO} are carbon dioxide and carbon monoxide outlet molar flow rates and $F^{out}_{CH_3OH}$ is the inlet methanol molar flow rate.

5.3. Results and Discussion

5.3.1. Physicochemical characterization

The physicochemical properties of the in-house CuZrDyAl and the as-received $CuO/ZnO/Al_2O_3$ catalysts (hereafter denoted as G66 MR) were evaluated by means of the following techniques: ICP-MS (catalyst composition), N_2-physisorption (BET surface area), SEM-EDX (structure), XRD (crystallinity) and H_2-TPR (reducibility).

The composition of both samples determined by ICP is given in Table 5.1. A weight percentage of $CuO/ZrO_2/Dy_2O_3/Al_2O_3$: 65.1/19.7/4.8/10.4 was found for the CuZrDyAl catalyst, in good agreement with the experimental composition

(65/20/5/10). The G66 MR sample has a composition of $CuO/ZnO/Al_2O_3$: 65.8/25.7/8.5. It is important to note that both samples exhibit nearly the same copper content (ca. 65 wt.% CuO) and, considering that Cu-species are the active sites for MSR reaction, the catalytic differences observed here can be related to different physicochemical properties.

Figure 5.1 shows the nitrogen adsorption-desorption isotherm for CuZrDyAl (Figure 5.1-A) and G66 MR (Figure 5.1-B) catalysts. According to the IUPAC classification, the isotherms obtained for both samples appear to be type-IV with a type-H3 hysteresis loop, indicating a mesoporous structure. Although both samples showed the same type of isotherm, clearly the amount of adsorbed nitrogen was different (Figures 5.1A-B). Accordingly, the specific surface area and pore volume values of CuZrDyAl (98 $m^2 \cdot g^{-1}$; Vp: 0.61 $cm^3 \cdot g^{-1}$) are significantly higher than those of G66 MR (60 $m^2 \cdot g^{-1}$; Vp: 0.36 $cm^3 \cdot g^{-1}$).

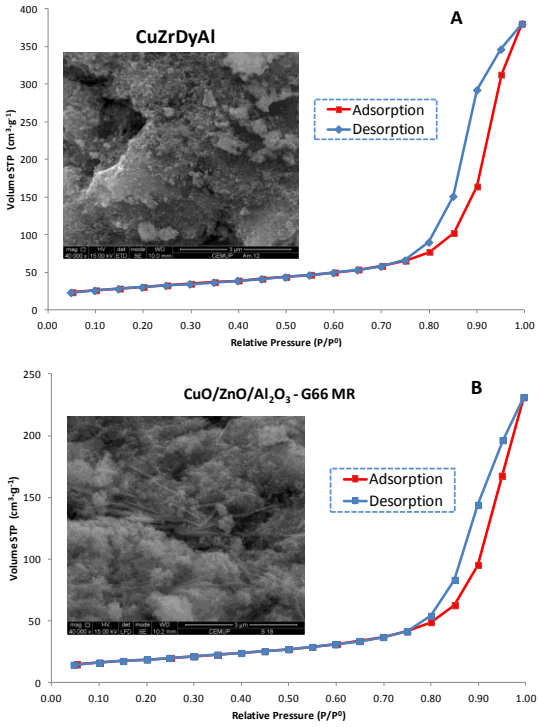

Figure 5.1 - Nitrogen adsorption–desorption isotherm of synthesized CuZrDyAl after calcination at 360 °C (A) and as received G66 MR (B) samples. SEM images of both samples with a magnification of x40,000 (inset).

The XRD patterns of both samples are displayed in Figure 5.2. All the diffraction lines of the CuZrDyAl sample can be indexed using the tenorite phase of CuO (ICDD file number 00-048-1548). As apparent in Figure 5.2, no diffraction lines of any Al, Zr or Dy compounds were observed for CuZrDyAl, suggesting that these species were highly dispersed in this sample. In the case of the G66 MR sample, besides tenorite phase, additional features ascribed to zinc oxide (ZnO – ICDD file number 01-089-1397) and aluminum oxide (Al_2O_3 – ICDD file number 01-070-3321) are found (Figure 5.2).

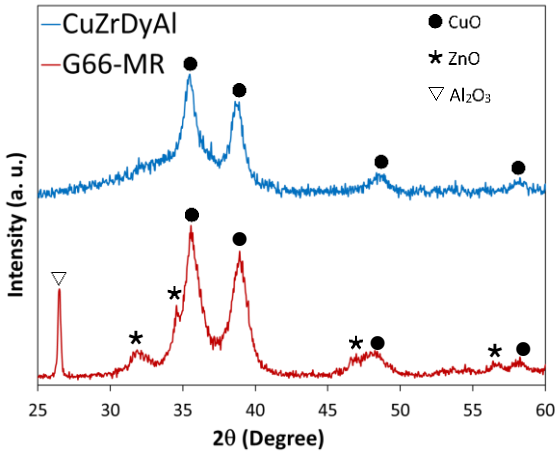

Figure 5.2 - XRD patterns of synthesized CuZrDyAl after calcination at 360 °C and as received G66 MR samples.

Both catalysts show broad CuO peaks, indicating that they are made up of relatively small CuO particles (note that both catalysts contain 65 wt. % of CuO). The estimated mean crystallite size of CuO for both samples is in the order of 9 nm (Table 5.1).

Table 5.1 - Average crystallite size of CuO determined from the XRD data using the Scherrer equation and chemical composition (ICP) of CuZrDyAl and G66 MR samples.

Sample	CuO mean crystallite size (nm)	Chemical composition (ICP) (wt.% of metal oxides)
CuZrDyAl	8.7	CuO = 65.1 ZrO_2 = 19.7 Dy_2O_3 = 4.8 Al_2O_3 = 10.4
CuO/ZnO/Al_2O_3 G66-MR	7.9	CuO = 65.8 ZnO = 25.7 Al2O3 = 8.5

The H_2-TPR profiles of CuZrDyAl and G66 MR catalysts are presented in Figure 5.3. The TPR curve of a bare CuO sample is also included in this figure for comparative purposes. Clearly, and not surprisingly, CuZrDyAl and G66 MR catalysts are reduced at much lower temperatures than the reference CuO sample (Figure 5.3, Table 5.2). This is in line with reported data, since addition of promoters, such as ZrO_2 and ZnO, results in catalysts that are easier to reduce than their unpromoted counterparts[28-30].

The TPR profile of pure CuO (Figure 5.3 and Table 5.2) is characterized by two reduction peaks at ca. 280 °C (LT-peak) and 320 °C (HT-peak). According to other published works [17, 30, 31] and reference 18 of the present study, the presence of two reduction signals in bulk CuO is attributed to the stepwise reduction of copper oxide according to the following equation:

$$Cu^{2+} \rightarrow Cu^{+} \rightarrow Cu^{0} \quad (5.5)$$

Thus, one can assume that LT-peak and HT-peak in Figure 5.3 correspond to the two-step reduction from Cu^{2+} to Cu^{0} described by Equation 5.5.

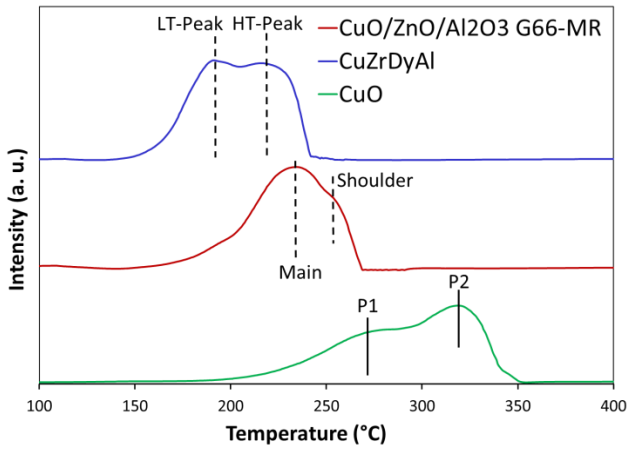

Figure 5.3 - H_2–TPR profiles of the CuZrDyAl and G66-MR catalysts. The H_2-TPR profile of a bulk CuO is also shown for comparison.

It is interesting to note that the reduction temperature of copper in the CuZrDyAl sample is significantly lower (by about 45 °C; Table 5.2) than that of the G66-MR sample (Figure 5.3 and Table 5.2), although both samples have similar copper content (Table 5.1). On the other hand, the shape of the TPR curve of both catalysts are clearly different (Figure 5.3). The TPR profile of the in-house catalyst displays two distinct reduction peaks, a major peak at a lower temperature (LT-peak in Figure 5.3), which represents about 75 % of the overall peak area, and the other peak at higher temperature (HT-peak in Figure 5.3).

The occurrence of two peaks in the CuZrDyAl sample could be due to the presence of: (i) copper oxide species with different particle sizes; and/or (ii) copper species differently interacting with the zirconia-rich matrix. The present findings also confirmed previous results reporting on the existence of two reduction peaks for binary Cu/ZrO_2 samples [32, 33]. The authors attributed this behavior to the presence of different copper-ZrO_2 interactions.

Table 5.2 - H_2-TPR data of bare CuO, CuZrDyAl and G66 MR catalysts**.**

Sample	*LT-peak*(°C)	*HT-peak* (°C)
Pure CuO	280	320
G66 MR	235	255
CuZrDyAl	191	221

As seen in Figure 5.3, the G66-MR sample was fully reduced between 165 and 270 °C. Unlike the in-house sample, G66-MR shows a single broad peak centered at 235 °C with a small shoulder around 255 °C.

The present findings unequivocally evidence that the reducibility of CuO was significantly improved in the CuZrDyAl catalyst. The addition of Zr and Dy as promoters allows lowering the CuO reduction temperature, which is likely due to the strong interaction of copper species with the ZrDy-containing matrix. Two kinds of copper species are present on the surface of the in-house catalyst that are responsible for the two reduction peaks observed during the reduction of this sample.

To sum up, the in-house CuZrDyAl and G66 MR catalysts were characterized according to their, elemental composition, textural properties, crystallinity and reducibility. According to XRD both samples have similar CuO particle size although the in-house sample has a higher specific surface area. The main difference between both samples is undoubtedly the reducibility of CuO that is noticeably enhanced in the CuZrDyAl catalyst.

According to XRD, both samples have similar CuO particle size although the in-house sample has a higher specific surface area. The amount of CuO was also approximetly the same for both catalysts (see Table 5.1). Therefore, the main difference between the two samples is undoubtedly the reducibility of CuO that is noticeably enhanced in the CuZrDyAl catalyst. There is evidence in the literature that underlines the importance of the ease of copper reduction for having improved activity for MSR [17, 22, 38, 39]. In fact, ZrO_2 and ZnO are pointed out to have benefitial role for decreasing the reduction temperature of copper-based catalysts, which is suggested to be a consequence of a hydrogen spill-over effect [17, 38].

Threfore, depending on the metal oxide matrix that surrounds the copper particles, changes can occur in the Cu^0/Cu^{ox} redox mechanism, which is suggested to be an important factor for the catalyst activity [17, 40].

5.3.2. Kinetic Models

In the literature it can be found several semi-empirical and mechanistic models for the MSR reaction. The mechanism of the MSR reaction is still a matter of debate; some authors consider the CO formation from RWGS excluding MD [12, 26] and others include a network of three reactions where MD has also a contribution. For instance, Peppley *et al.*, has reported a kinetic model that includes MD, RWGS and MSR [13].

Since the kinetic experiments in this work were performed at low-temperature (170 °C-200 °C), the contribution of MD as a sideway reaction should be negligible. There are many studies that support this assumption, and attribute the formation of CO to the RWGS due to the high concentrations of CO_2 and H_2 in the reaction medium [5, 12, 22, 26].

5.3.3. Empirical model

The use of empirical equations to compute the MSR rate is a common strategy reported in the literature [5, 11, 25, 34]. Despite their simplicity, in some cases the experimental results are better fitted using power-laws [35]. Moreover, some authors denote preference for the power-law kinetics when the purpose of the study is to predict the hydrogen and CO production for fuel cells applications [25]. In this work, the following power-law expression was used to describe the experimental results and was designated as Model 1:

$$-r_{MSR} = k_{MSR} P_{CH_3OH}^{a} P_{H_2O}^{b} P_{H_2}^{c} P_{CO_2}^{d} \tag{5.6}$$

where k_{MSR} is the kinetic constant of the MSR reaction ($k_{MSR} = k_0 e^{-E_a/RT}$), where E_a is the activation energy, k_0 is the pre-exponential factor, *R* is the gas constant and T is the absolute temperature – Arrhenius equation); a, b, c and d are the apparent reaction orders of methanol, water, hydrogen and carbon dioxide. This model has been used in the literature for the MSR reaction on $CuO/ZnO/Al_2O_3$ commercial catalysts [5, 25]. It has a total of 6 parameters, including the activation energy and pre-exponential factor.

5.3.4. *Mechanistic Models*

There are several mechanistic expressions that describe the kinetics of MSR and there is still controversy regarding this matter in the literature. The first reaction mechanism proposes the formation of H_2 and CO primarily from MD and then the water-gas shift (WGS) would occur to produce CO_2 and H_2 [36]. Other authors claimed that the correct pathway involves the formation of CO_2 and H_2 through direct MSR, followed by the RWGS reaction [37]. According to the first mechanism, the amount of CO should be equal or higher to the equilibrium of the RWGS reaction and this condition must be verified for the whole temperature range [12, 26]. However, experimental results have indicated the opposite, meaning that the CO amount in the temperature range of 160 °C to 260 °C was always below the equilibrium of the RWGS [5, 12].

The Langmuir-Hinshelwood kinetic equation proposed by Tesser *et al.* [26] assumes the formation of CO from MD followed by WGS that leads to production of H_2 and CO_2 as reaction pathways. The detrimental effect of the partial pressure of both H_2 and H_2O are included factors on the model equation. This inhibitory effect takes into account the competitive adsorption of the reactants, water and methanol, and of the produced hydrogen on the active sites. The former model was applied to the obtained experimental data and it was designated as Model 2:

$$-r_{MSR} = \frac{k_{MSR} K_{CH_3OH} p_{CH_3OH}}{1 + K_{CH_3OH} p_{CH_3OH} + K_{H_2O} p_{H_2O} + K_{H_2} p_{H_2}} \quad (5.7)$$

where k_{MSR} is the methanol steam reforming kinetic constant; K_{CH_3OH}, K_{H_2O} and K_{H_2} are the adsorption equilibrium constants of methanol, water and hydrogen, respectively; p_{CH_3OH}, p_{H_2O} and p_{H_2} are the partial pressures of methanol, water and hydrogen. This model has eight parameters, including the activation energy and pre-exponential factor.

Peppley *et al.* [13] proposed a reaction network considering MSR, MD and RWGS reactions and assumed two different active sites on the catalyst, one for hydrogen and the other for oxygen containing species. The resulting rate expression can be written as follows and was designated as Model 3:

$$-r_{\mathrm{MSR}} = \frac{\dfrac{k_{\mathrm{MSR}} K_{\mathrm{CH_3O^{(1)}}}\, p_{\mathrm{CH_3OH}}}{p_{\mathrm{H_2}}^{1/2}}\left(1-\dfrac{p_{\mathrm{H_2}}^{3}\, p_{\mathrm{CO_2}}}{K_{SR}\, p_{\mathrm{H_2O}}\, p_{\mathrm{CH_3OH}}}\right)}{\left(1+\dfrac{K_{\mathrm{CH_3O^{(1)}}}\, p_{\mathrm{CH_3OH}}}{p_{\mathrm{H_2}}^{1/2}}+\dfrac{K_{\mathrm{OH^{(1)}}}\, p_{\mathrm{H_2O}}}{p_{\mathrm{H_2}}^{1/2}}+K_{\mathrm{HCOO^{(1)}}}\, p_{\mathrm{H_2}}^{1/2}\, p_{\mathrm{CO_2}}\right)\left(1+\sqrt{K_{\mathrm{H^{(1a)}}}\, p_{\mathrm{H_2}}}\right)} \tag{5.8}$$

Here constants denoted by K_i are the adsorption equilibrium constants for the intermediate species involved and K_{MSR} is the equilibrium constant for MSR. The model has a total of ten parameters, including the activation energy and pre-exponential factor. The parameters estimation was, however, simplified using data gathered by Skrzypek *et al.* regarding the adsorption of various reactants, products and possible intermediates in methanol synthesis for the $CuO/ZnO/Al_2O_3$ commercial catalyst [13]; as a result, the number of parameters estimated was reduced to a total of six. In this work, the model suggested by Peppley *et al.* with six and ten parameters was considered and parameters were obtained by non-linear regression.

5.3.5. Parameters estimation

Assuming plug flow pattern and no mass transfer resistances, the mass balance to the reactor fixed bed is:

$$-dF = F^0 dX_{CH_3OH} = \left(-r_{CH_3OH}\right) dW \tag{5.9}$$

where F^0 is the flow rate of methanol and $\left(-r_{CH_3OH}\right)$ is reaction rate of methanol. Rearranging Equation (5.9) one obtains:

$$\left(-r_{CH_3OH}\right) = \frac{dX_{CH_3OH}}{d\left(W/F^0\right)} \tag{5.10}$$

where X_{CH_3OH} is the methanol conversion. The experimental reaction rates were determined from the first derivative of a second order polynomial fitting curve to the experimental results (Equation 5.10) [12, 13]. The kinetic parameters were obtained minimizing the mean residual sum of the squares (*MSRR*) (Equation 5.11):

$$MSRR = \frac{\sum_{i=1}^{N}\left(r_{exp,i} - r_{cal,i}\right)^2}{N - N_p} \tag{5.11}$$

Here, $r_{exp,i}$ and $r_{cal,i}$ are respectively the experimental and predicted reaction rates; N and N_p are respectively the number of experimental values ($N = 24$) and of estimated parameters.

Figure 5.4 presents the parity plots for each model; a good fitting between calculated and experimental values is observed. The mechanistic models provide a closer description of the experimental reaction rates, moreover Model 3 present the lowest *MSRR*, 1.4×10^{-7}. Accordingly, when comparing Model 3 with Model 3* (Table 5.3), a slightly worst fitting of Model 3* was obtained; the parameters obtained in this work for the CuZrDyAk do not present significant differences to the data tabled for the commercial $CuO/ZnO/Al_2O_3$. Lee *et al.* observed the same behavior for CuO/ZnO/MnO/Al2O3 catalyst [12]. Actually, the former catalyst has only 2 wt.% of MgO and therefore it has a very close chemical composition when compared to the commercial catalyst. This suggests that a small change in the metal oxide composition of the catalyst does not affect significantly the adosption equilibrium enthalpies (see Table 5.1).

Finally, Model 2 considers a very different reaction mechanism and had a *MSRR* of $1.7x10^{-7}$. There is a clear difference between both models regarding the reaction schemes; Peppley *et al.* (Model 3) assumes a reaction network with MD, MSR and RWGS occurring sideway, while Tesser *et al.* (Model 2) assumes a mechanism where CO is first produced as a result from MD, and afterwards WGS occurs to form to CO_2 and H_2. Other studies report that the amount of CO produced during MSR is above the WGS equilibrium, which suggests a different reaction path than the one addressed by Tesser *et al.* [5, 12]. Comparing both mechanism in more detail, the mechanism model presented by Peppley *et al.* for MSR (Model 3) was based on the extensive data reported in the literature for the methanol synthesis reaction (MS). Despite this fact, the reverse methanol synthesis models failed to describe MSR, mainly due to the differences in the reducing potential of the reactant mixture that changes the chemical state of the catalyst. The compiled MS results indicate that H_2 has a unique mode of adsorption, as described by Peppley *et al.*. This has led to a model that assumes two different active sites, one for hydrogen, and a common site for the competitive adsorption of CH_3OH, CO, CO_2 and H_2O. The other mechanistic model reported by Tesser *et al.* is a Langmuir-Hinshelwood-Hougen-Watson type of model that was not derived form and explicit mechanism and also does not have any background of experimental data regarding the adsorption of compounds at the surface of the same catalyst. In fact, one of the assumptions of this model is competitively adsorption of hydrogen, water and methanol in the same active site. Finally, Model 1 is an empirical model, and is a mathematical expression without any mechanistic insight. Despite this, as already mentioned, there is a preference of some authors [25] for using a power-law equation that are simple to use and provide an acceptable fitting with the experimental data.

Figure 5.5 compares the MSR experimental and model conversions as a function of the space-time for various temperatures. It can be concluded that the model based on Peppley *et al.* work (Model 3) fits quite well the experimental values. However, in the same figure it is possible to observe that the power law model also fits well with the experimental data, despite being a quite simple model.

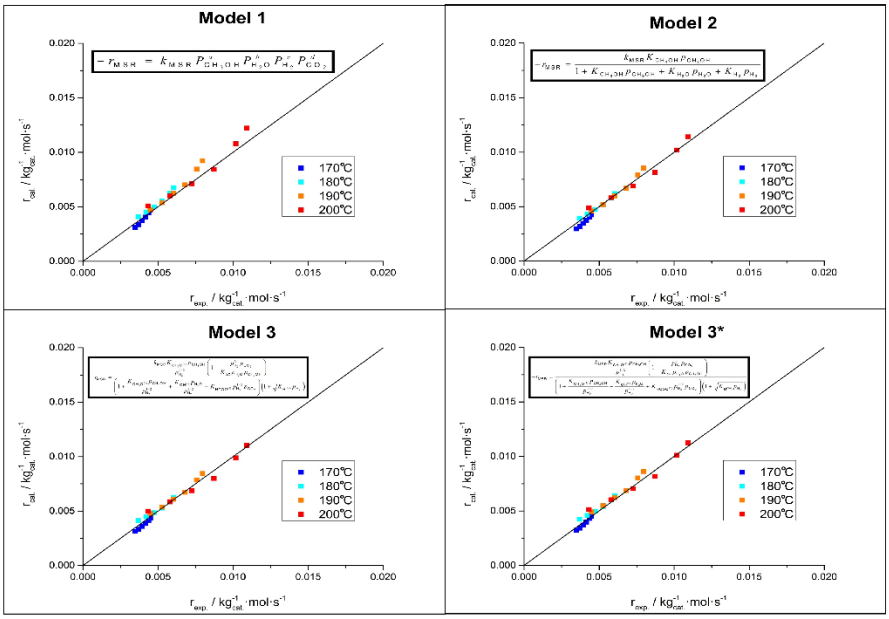

Figure 5.4 - Parity plots of the experimental and predicted reaction rates using different models. Reaction conditions: steam/methanol = 1.5, P = 1 bar, catalyst weight (W) = 0.4 g, methanol flow rate = 0.02-0.06 mL/min.

Table 5.3 - Parameters determined for the different models. The adsorption equilibrium enthalpies (ΔHi) are in kJ·mol^{-1} and the entropies of adsorption (ΔSi) are in J·mol·k^{-1} and values labeled with "p" refers to the data from Peppley *et al.* [13].

	Temperature		Adsorption Equilibrium								MSRR
	E_a **(kJ·mol^{-1})**	k_0 **(mol·kg$^{-1}_{cat.}$·s^{-1})**									
Model 1	77.8	2.0x10^7	a	b	c	0	-	-	-		3.7x10^{-7}
			0.42	0.99	0	0					
Model 2	76.0	5.0x10^6	ΔH_{CH_3OH}	ΔS_{CH_3OH}	ΔH_{H_2O}	ΔS_{H_2O}	ΔH_{H_2}	ΔS_{H_2}	-	-	1.7x10^{-7}
			-50.1	151.0	-57.5	127.1	-51.9	147.4			
Model 3	79.9	4.1x10^7	$\Delta H_{CH_3O^{(l)}}$	$\Delta S_{CH_3O^{(l)}}$	$\Delta H_{OH^{(l)}}$	$\Delta S_{OH^{(l)}}$	$\Delta H_{HCOO^{(l)}}$	$\Delta S_{HCOO^{(l)}}$	$\Delta H_{H^{(l)}}$	$\Delta S_{H^{(l)}}$	1.4x10^{-7}
			-20^p	-44.5	-20^p	-39.7	100^p	97.9	-50^p	-195.0	
Model 3*	77.5	8.6x10^7	$\Delta H_{CH_3O^{(l)}}$	$\Delta S_{CH_3O^{(l)}}$	$\Delta H_{OH^{(l)}}$	$\Delta S_{OH^{(l)}}$	$\Delta H_{HCOO^{(l)}}$	$\Delta S_{HCOO^{(l)}}$	$\Delta H_{H^{(l)}}$	$\Delta S_{H^{(l)}}$	2.1x10^{-7}
			-18.7	-51.9	-17.9	-34.0	114.4	84.8	-55.3	-155.0	

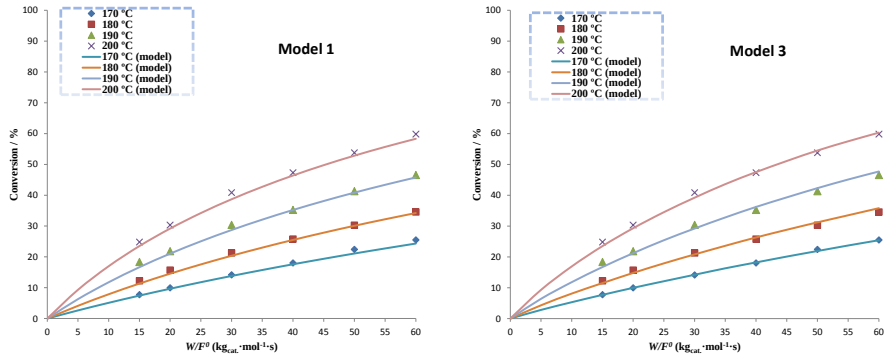

Figure 5.5 - Experimental (*symbols*) and simulated (*solid lines;* Model 1 and Model 3) results for methanol conversion versus the space-time ratio atdifferent temperatures. Reaction conditions: steam/methanol = 1.5, P = 1 bar, catalyst weight (W) = 0.4 g, methanol flow rate = 0.02 – 0.06 mL/min.

5.3.6. Comparison between the CuZrDyAl and the $CuO/ZnO/Al_2O_3$

According to the previous section, Model 3 is the mechanistic model that exhibits the best fitting. Therefore, a comparison is established between the estimated parameters obtained for CuZrDyAl and $CuO/ZnO/Al_2O_3$ (Süd-Chemie, G66 MR) catalysts when using this model – see Table 5.4.

For the MSR reaction the CuZrDyAl catalyst exhibits lower activation energy than $CuO/ZnO/Al_2O_3$ catalyst (Süd-Chemie, G66 MR), suggesting higher catalytic activity of the in-house prepared catalyst. Therefore, catalytic Süd-Chemie G66 MR was further characterized at 180 °C. Figure 5.6, compares the reaction conversion as a function of the space-time on both catalysts.

Figure 5.6 shows that the CuZrDyAl catalyst has a higher catalytic activity than the catalyst $CuO/ZnO/Al_2O_3$ at 180 °C. Moreover, CuZrDyAl catalyst produces less CO than commercial catalyst. At space time ratio of 100 $kg_{cat.}\cdot mol^{-1}\cdot s^{-1}$ and 180 °C the reformate stream contains 60 ppm of CO in the case of catalyst CuZrDyAl and 90 ppm of CO in the case of the commercial catalyst. The developed CuZrDyAl catalyst show to be a promising formulation for MSR, not only regarding its activity but also the CO amounts produced.

Table 5.4 - Comparison between the parameters obtained for the $CuO/ZnO/Al_2O_3$ (Süd-Chemie, G66 MR) and the CuZrDyAl catalysts in this work when considering Model 3

	$CuO/ZnO/Al_2O_3$	**CuZrDyAl**
E_a (kJ·mol^{-1})	86.9	79.9
k_0 (m^2·mol^{-1}·s^{-1})	4.0x10^{13}	3.7x10^{12}
$\Delta S_{CH_3O^{(l)}}$ (J·mol·k^{-1})	-47.9	-44.5
$\Delta H_{CH_3O^{(l)}}$ (kJ·mol^{-1})	-20	-20
$\Delta S_{OH^{(l)}}$ (J·mol·k^{-1})	-44.1	-39.7
$\Delta H_{OH^{(l)}}$ (kJ·mol^{-1})	-20	-20
$\Delta S_{HCOO^{(l)}}$ (J·mol·k^{-1})	100.1	97.9
$\Delta H_{HCOO^{(l)}}$ (kJ·mol^{-1})	100	100
$\Delta S_{H^{(la)}}$ (J·mol·k^{-1})	-223.2	-195.0
$\Delta H_{H^{(la)}}$ (kJ·mol^{-1})	-50	-50

***** The kinetic constant reported in the literature by Peppley *et al.* is presented in m^2·mol^{-1}·s^{-1} and for comparison purposes the values in this table where converted to the same units using the surface area of the CuZrDyAl catalyst (98 m^2·g^{-1}) and the total surface concentration of the active sites considered in the model.

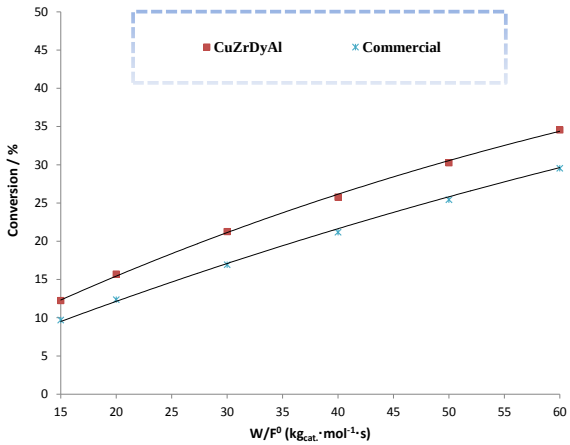

Figure 5.6 – Methanol conversion as a function of $W_{cat} = F^0_{CH_3OH}$ ration of synthesized CuZrDyAl and commercial G66-MR (Süd-Chemie) catalysts; reaction conditions: steam/methanol = 1.5, T = 180 °C, P = 1 bar, catalyst weight (W) = 0.4 g, methanol flow rate = 0.02-0.06 mL/min.

5.4. Conclusions

A novel CuZrDyAl catalyst was synthesized, characterized and tested for low temperature MSR (170 ºC - 200 ºC) and a space time ratio between 15 $kg_{cat.} \cdot mol^{-1} \cdot s$ and 60 $kg_{cat.} \cdot mol^{-1} \cdot s$. The physicochemical characterization of the in-house catalyst CuZrDyAl and the reference catalyst G66-MR by Süd-Chemie indicates that in-house catalyst has an improved reducibility of copper oxide, which could be attributed to higher dispersion of copper particles and/or the presence of copper species strongly interacting with the Zr-rich matrix.

Three kinetic models were applied to describe the CuZrDyAl experimental reaction rates, where Model 3, showed the best fitting. The performance of the new catalyst was compared with catalyst G66-MR at 180 ºC and both selectivity and activity were higher for the CuZrDyAl sample. The better performances shown by the in-house sample could be attributed to its enhanced copper reducibility.

Acknowledgments

The research leading to these results has received funding from the European Union's Seventh Framework Program (FP/2007-2013) for the Fuel Cells and Hydrogen Joint Technology Initiative under grant agreement n° [303476]. Hugo Silva wishes to thank FCT-Foundation for Science and technology for the PhD fellowship, SFRH/BD/45890/2008. Dr. C. Mateos Pedrero is grateful to the Portuguese Foundation for Science and Technology (FCT) for her Post-Doctoral Grant (Reference: SFRH/BPD/97114/2013).

References

[1] Conte, M., Energy | Hydrogen Economy, in Encyclopedia of Electrochemical Power Sources, J. Garche, Editor. 2009, Elsevier: Amsterdam. p. 232-254.

[2] Olah, G.A., A. Goeppert, and G.K.S. Prakash, The Hydrogen Economy and its Limitations, in Beyond Oil and Gas: The Methanol Economy. 2009, Wiley-VCH Verlag GmbH & Co. KGaA. p. 143-178.

[3] Yang, J., et al., High capacity hydrogen storage materials: attributes for automotive applications and techniques for materials discovery. Chemical Society Reviews, 2010. 39(2): p. 656-675.

[4] Durbin, D.J. and C. Malardier-Jugroot, Review of hydrogen storage techniques for on board vehicle applications. International Journal of Hydrogen Energy, 2013. 38(34): p. 14595-14617.

[5] Sá, S., J.M. Sousa, and A. Mendes, Steam reforming of methanol over a CuO/ZnO/Al2O3 catalyst, part I: Kinetic modelling. Chemical Engineering Science, 2011. 66(20): p. 4913-4921.

[6] Palo, D.R., R.A. Dagle, and J.D. Holladay, Methanol Steam Reforming for Hydrogen Production. Chemical Reviews, 2007. 107(10): p. 3992-4021.

[7] Papasavva S, Sloane C, Wagner F, et al. (2005) Developing hydrogen (H_2) specification guidelines for proton exchange membrane (PEM) fuel cell vehicles

[8] Andreasen, S.J., S.K. Kær, and S. Sahlin, Control and experimental characterization of a methanol reformer for a 350 W high temperature polymer electrolyte membrane fuel cell system. International Journal of Hydrogen Energy, 2013. 38(3): p. 1676-1684.

[9] Jensen, J.O., et al., High temperature PEMFC and the possible utilization of the excess heat for fuel processing. International Journal of Hydrogen Energy, 2007. 32(10–11): p. 1567-1571.

[10] Lok M (2009) Coprecipitation. In: Synthesis of Solid Catalysts. Wiley-VCH Verlag GmbH & Co.KGaA, Weinheim, pp 135–151.

[11] Jiang, C.J., et al., Kinetic study of steam reforming of methanol over copper-based catalysts. Applied Catalysis A: General, 1993. 93(2): p. 245-255.

[12] Lee, J.K., J.B. Ko, and D.H. Kim, Methanol steam reforming over Cu/ZnO/Al2O3 catalyst: kinetics and effectiveness factor. Applied Catalysis A: General, 2004. 278(1): p. 25-35.

[13] Peppley, B.A., et al., Methanol–steam reforming on Cu/ZnO/Al2O3 catalysts. Part 2. A comprehensive kinetic model. Applied Catalysis A: General, 1999. 179(1–2): p. 31-49.

[14] Agrell, J., et al., Production of hydrogen from methanol over Cu/ZnO catalysts promoted by ZrO2 and Al2O3. Journal of Catalysis, 2003. 219(2): p. 389-403.

[15] Yang, H.-M. and M.-K. Chan, Steam reforming of methanol over copper–yttria catalyst supported on praseodymium–aluminum mixed oxides. Catalysis Communications, 2011. 12(15): p. 1389-1395.

[16] Matsumura, Y., Stabilization of Cu/ZnO/ZrO2 catalyst for methanol steam reforming to hydrogen by coprecipitation on zirconia support. Journal of Power Sources, 2013. 238(0): p. 109-116.

[17] Breen, J.P. and J.R.H. Ross, Methanol reforming for fuel-cell applications: development of zirconia-containing Cu–Zn–Al catalysts. Catalysis Today, 1999. 51(3–4): p. 521-533.

[18] Zhang, L., et al., CeO2–ZrO2-promoted CuO/ZnO catalyst for methanol steam reforming. International Journal of Hydrogen Energy, 2013. 38(11): p. 4397-4406.

[19] Jones, S.D. and H.E. Hagelin-Weaver, Steam reforming of methanol over CeO2- and ZrO2-promoted Cu-ZnO catalysts supported on nanoparticle Al2O3. Applied Catalysis B: Environmental, 2009. 90(1–2): p. 195-204.

[20] Park, J.E., et al., Steam reforming of methanol over Cu/ZnO/ZrO2/Al2O3 catalyst. International Journal of Hydrogen Energy, 2014. 39(22): p. 11517-11527.

[21] Tsai, M.-C., et al., Promotion of a copper-zinc catalyst with rare earth for the steam reforming of methanol at low temperatures. Journal of Catalysis, 2011. 279(2): p. 241-245.

[22] Yu, K.K., et al., Non-syngas direct steam reforming of methanol to hydrogen and carbon dioxide at low temperature. Nature Communications, 2012. 3.

[23] Tong, W., et al., Dramatic Effects of Gallium Promotion on Methanol Steam Reforming Cu-ZnO Catalyst for Hydrogen Production: Formation of 5 angstrom Copper Clusters from Cu-ZnGaOx. ACS Catalysis, 2013. 3(6): p. 1231-1244.

[24] Tong, W., et al., Direct methanol steam reforming to hydrogen over CuZnGaOx catalysts without CO post-treatment: mechanistic considerations. Physical Chemistry Chemical Physics, 2013. 15(19): p. 7240-7248.

[25] Samms, S.R. and R.F. Savinell, Kinetics of methanol-steam reformation in an internal reforming fuel cell. Journal of Power Sources, 2002. 112(1): p. 13-29.

[26] Tesser, R., M. Di Serio, and E. Santacesaria, Methanol steam reforming: A comparison of different kinetics in the simulation of a packed bed reactor. Chemical Engineering Journal, 2009. 154(1–3): p. 69-75.

[27] Froment, G.F. and K.B. Bischoff, Chemical Reactor Analysis and Design. Second ed. 1990, New York: Wiley.

[28] Shishido, T., et al., Active Cu/ZnO and Cu/ZnO/Al2O3 catalysts prepared by homogeneous precipitation method in steam reforming of methanol. Applied Catalysis A: General, 2004. 263(2): p. 249-253.

[29] Jung, K. and A. Bell, Effects of Zirconia Phase on the Synthesis of Methanol over Zirconia-Supported Copper. Catalysis Letters, 2002. 80(1-2): p. 63-68.

[30] Fernández-García, M., et al., Tracking Down the Reduction Behavior of Copper-on-Alumina Catalysts. Journal of Catalysis, 1998. 178(1): p. 253-263.

[31] Turco, M., et al., Cu/ZnO/Al2O3 catalysts for oxidative steam reforming of methanol: The role of Cu and the dispersing oxide matrix. Applied Catalysis B: Environmental, 2007. 77(1–2): p. 46-57.

[32] Zhao, Y., K. Tao, and H.L. Wan, Effect of zirconia phase on the reduction behaviour of highly dispersed zirconia-supported copper oxide. Catalysis Communications, 2004. 5(5): p. 249-252.

[33] Köppel, R.A., C. Stöcker, and A. Baiker, Copper- and Silver–Zirconia Aerogels: Preparation, Structural Properties and Catalytic Behavior in Methanol Synthesis from Carbon Dioxide. Journal of Catalysis, 1998. 179(2): p. 515-527.

[34] Idem, R.O. and N.N. Bakhshi, Kinetic modeling of the production of hydrogen from the methanol-steam reforming process over Mn-promoted coprecipitated Cu-Al catalyst. Chemical Engineering Science, 1996. 51(14): p. 3697-3708.

[35] Purnama, H., et al., CO formation/selectivity for steam reforming of methanol with a commercial CuO/ZnO/Al2O3 catalyst. Applied Catalysis A: General, 2004. 259(1): p. 83-94.

[36] Santacesaria, E. and S. Carrá, Kinetics of catalytic steam reforming of methanol in a cstr reactor. Applied Catalysis, 1983. 5(3): p. 345-358.

[37] Geissler, K., et al., Autothermal methanol reforming for hydrogen production in fuel cell applications. Physical Chemistry Chemical Physics, 2001. 3(3): p. 289-293.

[38]. Matter P (2004) Steam reforming of methanol to H_2 over nonreduced Zr-containing CuO/ZnO catalysts. J Catal 223:340–351

[39] Fierro G, Lo Jacono M, Inversi M et al (1996) Study of the reducibility of copper in CuO/ZnO catalysts by temperature-programmed reduction. Appl Catal A 137:327–348

[40] Fujitani T, Saito M, Kanai Y et al (1994) The role of metal oxides in promoting a copper catalyst for methanol synthesis. Catal Lett 25:271–276

Chapter 6

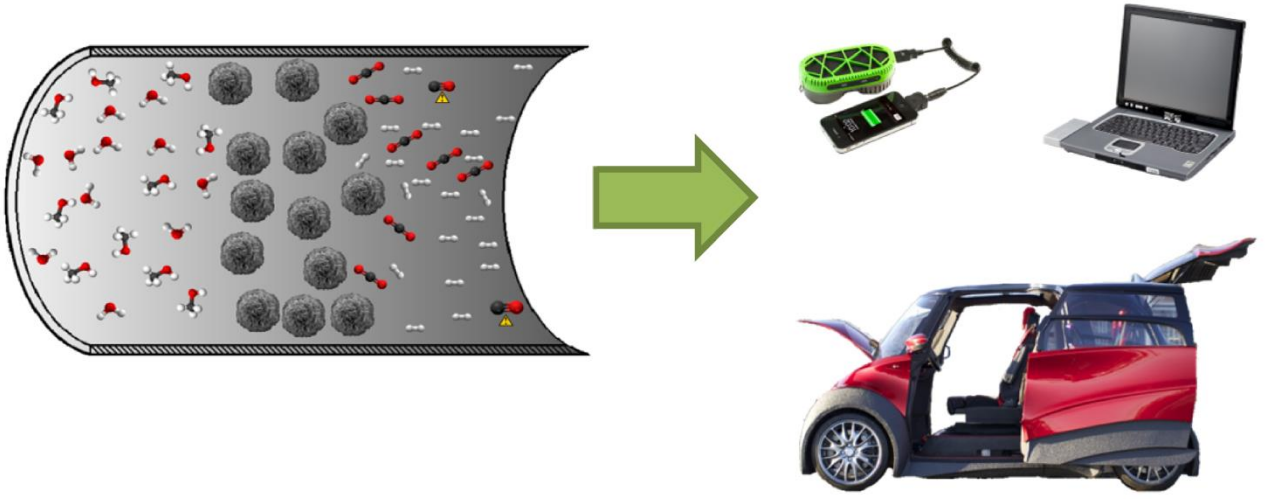

Chapter 6. General Conclusions and Future Work

The present thesis aimed the development and study of highly active-selective catalysts for methanol steam reforming reaction (MSR), with the purpose of supplying hydrogen for PEMFCs. In chapter 2, the physicochemical properties of ZnO (polarity, surface area and morphology) are tailored using a simple hydrothermal method of easy scaling-up. Synthesis temperature, surfactant concentration and calcination temperature/time were the optimized parameters that allowed to obtain a ZnO material with high surface area (80 $m^2 \cdot g^{-1}$), much higher than the typical commercial ZnO supports (10 $m^2 \cdot g^{-1}$) and with a high proportion of polar planes, being the polar planes considered the most reactive surfaces for MSR. The method was only applied to ZnO, however it would be interesting to synthesized mixed metal oxide catalysts using the same hydrothermal route.

In chapter 3, the ZnO supports with different physicochemical properties were used to prepare binary CuO/ZnO catalysts through and incipient wetness impregnation method. The activity of the CuO/ZnO catalysts was directly related with the surface area of the ZnO supports. The $CuO/ZnO_{Ac\text{-}375}$ sample presented a better activity, due to its higher surface area and dispersion of active copper metal particles. The polarity was another studied property of ZnO that revealed to be closely related with the selectivity of the prepared CuO/ZnO catalysts. Again the $CuO/ZnO_{Ac\text{-}375}$ catalyst presented the highest polarity and remarkably, showed a better selectivity than the reference commercial catalyst, $CuO/ZnO/Al_2O_3$. As result, this is a promising catalyst for testing a direct supply of a reformate stream to a HT-PEMFC without compromising the performance of the anode electrochemical catalyst. The choise of preparing the catalysts through the IWI method has the advantage of the catalysts properties being largely determined by the support, however it should be remainded the limited solubility of the active-phase precursor may cause some drawbacks. One of the issues, is the difficulty of preparing catalysts with a loading of copper active-phase comparable to the optimized commercial sample (CuO: 66 wt. %).

In the following chapter, the Pd/ZnO catalysts were studied. The calcination atmosphere of the ZnO supports revealed to influence the selectivity of the catalysts. Accordingly, the lower CO selectivity was attained for the catalyst prepared with a ZnO support calcined under a H_2 atmosphere. This was attributed to the higher number of oxygen vacancies present in this ZnO support. Once more, the ZnO properties had a major impact in the catalyst performance. In this group of catalysts, an interesting approach is the possibility of studying the MSR performance through the formation of selective alloys. For a future work, the study of new alloys is a matter of great importance, such as Ga-based alloys that are easier to form at low-temperatures and had a recent impact in the methanol synthesis field.

In the last chapter of the thesis, it was performed a kinetic study over a novel CuZrDyAl catalyst formulation and tested in a low temperature range of MSR (170-200 °C). The catalyst was prepared through a coprecipitation method that allows the preparation of bulk catalysts with extremely high metal loadings and a relatively high metal dispersion. This catalyst was comparated to the reference $CuO/ZnO/Al_2O_3$ (G66 MR, Süd-Chemie) and had an improved performance in terms of selectivity and activity. Three kinetic models were applied to describe the CuZrDyAl experimental reaction rates: one empirical and two mechanistic. The mechanistic model 3 provided a better fitting of the experimental data. As future work, it should be deeply studied the influence of reverse water-gas shift reaction (RWGS) at such operating temperatures. Methanol decomposition is not a major issue below 200 °C, however if the purpose is to supply a reformate stream near full conversion conditions, this implicates very high space-time ratios, which drawback favors RWGS and this way the production of CO. Additionally, complete conversion means lower amount of methanol supply and consequently a decrease in the hydrogen flow rates. Both factors have a major impact in the integration with HT-PEMFCs.